NUMERICAL MODELLING OF NANOPOROUS ANODIC ALUMINA PHOTONIC STRUCTURES FOR OPTICAL BIOSENSING

Francisco Bertó Roselló

UNIVERSITAT ROVIRA i VIRGILI

NUMERICAL MODELLING OF NANOPOROUS ANODIC ALUMINA PHOTONIC STRUCTURES FOR OPTICAL BIOSENSING

FRANCISCO BERTÓ-ROSELLÓ

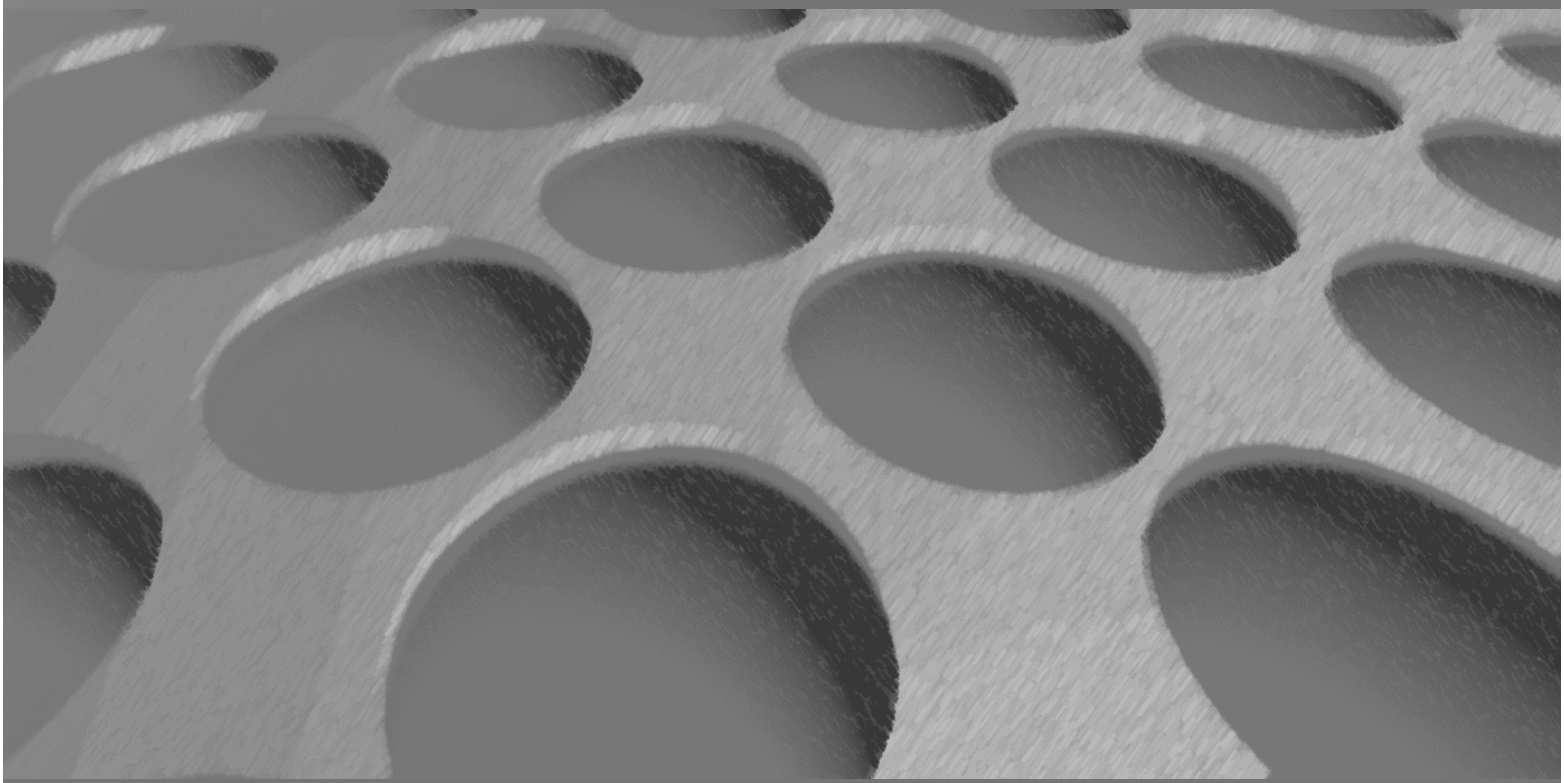

DOCTORAL THESIS
2018

UNIVERSITAT ROVIRA I VIRGILI
NUMERICAL MODELLING OF NANOPOROUS ANODIC ALUMINA PHOTONIC STRUCTURES FOR OPTICAL BIOSENSING
Francisco Bertó Roselló

UNIVERSITAT ROVIRA I VIRGILI
NUMERICAL MODELLING OF NANOPOROUS ANODIC ALUMINA PHOTONIC STRUCTURES FOR OPTICAL BIOSENSING
Francisco Bertó Roselló

UNIVERSITAT ROVIRA I VIRGILI
NUMERICAL MODELLING OF NANOPOROUS ANODIC ALUMINA PHOTONIC STRUCTURES FOR OPTICAL BIOSENSING
Francisco Bertó Roselló

FRANCISCO BERTÓ-ROSELLÓ

NUMERICAL MODELLING OF NANOPOROUS ANODIC ALUMINA PHOTONIC STRUCTURES FOR OPTICAL BIOSENSING

Doctoral Thesis

Supervised by Dr. Josep Ferré-Borrull

Department of Electric, Electronic and Automatic Control Engineering

UNIVERSITAT ROVIRA i VIRGILI

Tarragona
2018

UNIVERSITAT ROVIRA I VIRGILI
NUMERICAL MODELLING OF NANOPOROUS ANODIC ALUMINA PHOTONIC STRUCTURES FOR OPTICAL BIOSENSING
Francisco Bertó Roselló

UNIVERSITAT ROVIRA I VIRGILI

Departament d'Enginyeria Electrònica, Elèctrica i Automàtica
Escola Tècnica Superior D'Enginyeria
Campus Sescelades
Avinguda dels Països Catalans, 26
43007 Tarragona
Tel. 977 55 96 10
Fax 977 55 96 05

I STATE that the present study, entitled "NUMERICAL MODELLING OF NANOPOROUS ANODIC ALUMINA PHOTONIC STRUCTURES FOR OPTICAL BIOSENSING", presented by Francisco Bertó-Roselló for the award of the degree of Doctor, has been carried out under my supervision at the Department of Electronic, Electric and Automatic Control Engineering of this university.

Tarragona, 31^{th} August 2018.

Doctoral Thesis Supervisor

Dr. Josep Ferré-Borrull

UNIVERSITAT ROVIRA I VIRGILI
NUMERICAL MODELLING OF NANOPOROUS ANODIC ALUMINA PHOTONIC STRUCTURES FOR OPTICAL BIOSENSING
Francisco Bertó Roselló

Acknowledgements

First of all, I would like to express my sincere thanks to my supervisor Dr. Josep Ferré-Borrull for giving me incalculable support with my doctorate. His valuable advice, constructive criticism, patience and understanding helped me throughout this research period. I feel fortunate to have worked with him.

I would like to give special thanks to Dr. Lluís Marsal for the opportunity to work in the Nanoelectronic and photonic group systems (NePhoS), as well as his valuable comments and suggestions. I also really appreciate very much having been able to work with him.

I would like to acknowledge all the members of the NePhoS group (former and current) at the University Rovira i Virgili for their welcome, help and support, and, of course for the good times with all of them. Apologies in advance in case I leave someone. Thanks to Pili, José, Karen, Laura, Pilar, Aurelien, François,Caterina, Sara, Jakub, Elisabet, Maria, Chris, Magali, Angel, Carlos, Mari Carmen and Pankaj.

I would like to express immense gratitude to the members of my family. To my parents, Francisco and Amparo who have always been an example of hard work and a lifetime of support, as well as my sister Amparo who has always been a support. Special thanks to my in-laws, Salvador and Ramona because they have always been by my side.

Finally, I want to express my greatest gratitude to my wife, for her patience and confidence. Thank you for sharing your life with Aina, Martina and with me. This thesis is dedicated to you.

UNIVERSITAT ROVIRA I VIRGILI
NUMERICAL MODELLING OF NANOPOROUS ANODIC ALUMINA PHOTONIC STRUCTURES FOR OPTICAL BIOSENSING
Francisco Bertó Roselló

Table of contents

UNIVERSITAT ROVIRA I VIRGILI
NUMERICAL MODELLING OF NANOPOROUS ANODIC ALUMINA PHOTONIC STRUCTURES FOR OPTICAL BIOSENSING
Francisco Bertó Roselló

List of figures

List of tables

UNIVERSITAT ROVIRA I VIRGILI
NUMERICAL MODELLING OF NANOPOROUS ANODIC ALUMINA PHOTONIC STRUCTURES FOR OPTICAL BIOSENSING
Francisco Bertó Roselló

List of contributions

Journal articles

Bertó-Roselló, F., Xifré-Pérez, E., Ferré-Borrull, J., Pallarès, J., and Marsal, L. F. (2016). Nanoporous Anodic Alumina 3D FDTD Modelling for a Broad Range of Inter-pore Distances. *Nanoscale Res. Lett.*, 11(1):359.

Bertó-Roselló, F., Xifré-Pérez, E., Ferré-Borrull, J., and Marsal, L. F. (2018). 3D-FDTD Modelling of Optical Biosensing based on Gold-Coated Nanoporous Anodic Alumina. *Results in Physics*, 2018, Accepted (in press).

Acosta, L. K. **Bertó-Roselló, F.**, Xifré-Pérez, E., Santos, A., Ferré-Borrull, J., and Marsal, L. F. (2018). Stacked nanoporous anodic alumina gradient-index filters with tuneable multi-spectral photonic stopbands as sensing platforms., To be submitted.

Comunications

Bertó-Roselló, F., Xifré-Pérez, E., Ferré-Borrull, J., Pallarès, J., and Marsal, L. F.. 3D-FDTD Modelling Optical behaviour of Long Inter-pore Distance Nanoporous Anodic Alumina. *Porous Semiconductors - Science and Technology PSST*. Tarragona (SPAIN), 2016. Oral communication.

Bertó-Roselló, F., Xifré-Pérez, E., Ferré-Borrull, J., and Marsal, L. F. . Nanoporous Anodic Alumina 3D-FDTD Modelling Optical behaviour for Long Inter-pore Distance. *CEN2016 - Conferencia Española de Nanofotonica*. Valencia (SPAIN), 2016. Poster.

Bertó-Roselló, F., Xifré-Pérez, E., Ferré-Borrull, J., and Marsal, L. F.. Nanoporous Anodic Alumina Optical Biosensing Modelling with 3D-FDTD. *25th edition Optical*

Wave and Waveguide Theory and Numerical Modelling Workshop. Eindhoven (THE NETHERLANDS), 2017. Oral communication.

Bertó-Roselló, F., Acosta, L.K., Xifré-Pérez, E., Ferré-Borrull, J., and Marsal, L. F.. Numerical Modelling and Characterization of Nanoporous Anodic Alumina Rugate Filters. *Porous Semiconductors - Science and Technology PSST*. La Grande Motte (FRANCE), 2018. Poster.

Acosta, L.K., **Bertó-Roselló, F.**, Xifré-Pérez, E., Ferré-Borrull, J., and Marsal, L. F.. Nanoporous Anodic Alumina Rugate Filters for Optical Biosensing. *XII Reunión Nacional de Óptica*. Castellón (SPAIN), 2018. Oral communication.

Bertó-Roselló, F., Acosta, L.K., Xifré-Pérez, E., Ferré-Borrull, J., and Marsal, L. F.. Study of Nanoporous Anodic Alumina Gradient-Index Structures by Numerical Modelling. *CEN2018 - Conferencia Española de Nanofotonica*. San Sebastián (SPAIN), 2018. Poster.

Chapter 1

Introduction

1.1 General Remarks

It is well known from a variety of studies, that some materials shown particular physical, optical and chemical properties at the nanoscale. Nanotechnology permits scientists to enhance their properties modifying the matter structure at this level and taking advantage of them for the development of new devices and applications. The fields in which the nanotechnology is critical are diverse and involve different areas, such as biology, materials science, optics, energy and medical sciences.

In medical sciences the development of new devices for biomedical applications are increasing the interest of research areas as, for example, drug delivery and biosensing. Particularly important is the research in biosensing in order to obtain more sensitive and reliable devices with a view for their deployment to society in the form of cost-effective and reliable diagnostic systems. The manufacturing of such devices in some cases implies the manipulation of the light in these materials at the nanoscale, for which it implies to have a deep knowledge of the optical behaviour of the structure. In this sense, the election of the appropriate material with the ability of controlling the propagation of the light through them is decisive in the development of biosensing devices.

Nanoporous Anodic Alumina (NAA) is a self-ordered porous material produced by electrochemical anodization of aluminium with an hexagonal arrangement of cylindrical pores perpendicular to their surface. In the recent years, NAA structures have generated a considerable research interest because of their physical, chemical and optical properties. Actually, their optical properties in the visible, their great tunability of the structure, their ability to act as a holder of small objects, their stability under biological conditions and their capacity to act as a scaffold to hold other nanostructures are some of the

properties that make NAA especially appropriate as a platform for the development of optical biosensors. Focusing in the optical properties of the NAA, these are strongly dependent to their geometrical parameters. This fact permits to achieve a precise control of their optical properties by tuning the structure (for instance, by nanopore engineering or changing the lattice parameter of the pore arrangement).

Theoretical studies on the optical properties of these NAA structures is a fundamental field of research. The numerical modelling of the optical properties of NAA permits to understand their relationship with the structural features of the NAA, providing a conceptual framework for the analysis of their optical behaviour. Additionally, these simulations are a powerful tool for the improvement of the NAA-based devices with a design fundamented on a wider knowledge basis.

Several models exist in the literature to predict the optical behaviour of NAA-based devices, however the published research on this issue is very limited. Whilst most of these models are developed for a specific type of NAA with a restricted range of geometric and optical characteristics, there exist a paucity of published studies on NAA optical modelling in a broad range of structural features.

In this thesis, we aim at to cover this existing gap with the development of a predictive models for the optical properties of the NAA valid in a wide range of geometrical characteristics, as well as the suitability of the numerical method used.

1.2 Objectives

The objectives of this Thesis are:

- To develop computer implementations of numerical models for the theoretical study of the optical behaviour of NAA with a broad range of geometric and optical characteristics.
- To analyse the structural and the optical properties of the NAA in order to perform the modelling considering it as a one-dimensional and a two-dimensional photonic crystal.
- To study theoretically of the optical behaviour of gold-coated NAA as a proposal of application to sensing devices based on NAA.
- To study theoretically of the optical behaviour of NAA graded-index structures as a proposal of modelling tools applied to more complex structures, and a

theoretical study and assessment of an alternative proposal of sensing with NAA-based graded-index structures.

1.3 Structure of this Ph. D. Thesis

In order to achieve the objectives previously exposed, we organized the structure of this Ph. D. Thesis as follows:

In chapter 2 the state of the art is given. Firstly, a brief overview of fundamentals of NAA is presented. A glimpse on the fabrication process of NAA is given, with an introduction to the anodization and the structural parameters. The optical properties of the produced NAA are introduced as well as their dependence on these parameters. Finally, the state of the art about current simulation models of the optical properties of NAA closes this chapter.

Chapter 3 is devotes to the description of the numerical methods applied in this thesis. From the different techniques existing in the literature on numerical modelling, the chosen for our investigation had been restricted to those more suitable for the type of structures we are considering. Thus, an introduction to Effective Medium Approximation (EMA) techniques is given, as well as an introduction to Transfer Matrix Method (TMM) for the study of the NAA structure as a equivalent homogeneous material, resulting from the mixture of air and the aluminiumoxide matrix. Additionally, the fundamentals of the Finite-Differences in the Time Domain (FDTD) method also are introduced for the analysis of the NAA as a two-dimensional photonic crystal.

Chapter 4 is devoted to the modelling of the optical behaviour of NAA with the methods exposed in chapter 3. The optical behaviour dependence on the different structural parameters of two types of NAA structures are studied. Different geometrical models are proposed to simulate the optical properties of such structures. Simulations of the reflectance spectra are performed using both EMA with TMM and FDTD, and analysed and compared with the experimental data. The limitations and the suitability of the numerical methods applied and of the model adjustments are presented and discussed.

In chapter 5 we apply our simulation model to study the suitability of two types of gold-coated NAA structures as a platform for reflectometric-based plasmonic biosensors.

In this sense, the reflectance spectrum is simulated upon the absorption of biomolecules (modelled as a conformal "biolayer") on the gold coating layer and the inner pore walls. A study on the coupling of the incident light to a localized surface plasmon resonance because of the nanostructuring provided by the pore arrangement with the absorption of the biolayer is presented. Additionally, a sensitivity study on the biolayer thickness and the gold thickness is performed.

Chapter 6 presents a theoretical study of the optical behaviour of more complex NAA structures by means of numerical modelling: the gradient-index NAA (NAA-GI) based structures. The diameter of the cylindrical pores of this type of NAA structures are periodically modulated with the depth. This modification of pore morphology induces a variation in depth of the porosity modulating the effective refractive index of the medium with the pore depth. The optical behaviour of the NAA-GI structures is simulated considering them as a 1-D photonic crystal with their effective refractive index previously modelled with EMA and performed with TMM. An analysis of the relations between the anodization parameters and the structural parameters of NAA-GI (such as average pore diameter and pore modulation amplitude is presented.

Finally, the chapter 7 completes this thesis providing the summary and the conclusions reached in this work.

Chapter 2

State of the Art

The purpose of this chapter is to provide a basic introduction to the fundamentals of nanoporous anodic alumina (NAA) in order to supply the background for the understanding the results obtained in this thesis. However, a complete report on the fabrication of NAA and all of their features is beyond of the scope of this work and may be too broad because of its huge extension.

The chapter starts with a brief look on the NAA fabrication process method and describes the anodization and the structural parameters. The types of NAA produced in the NePhoS group at URV are also detailed, as well as their geometrical and chemical features. Next, the optical properties of the produced NAA are introduced as well as their dependence on the anodizing parameters. Finally, we provide the state of the art with the current simulation models for the optical properties of NAA.

2.1 Nanoporous anodic alumina basics

Aluminium, like other metals as Tantalum or Zirconium, when exposed to oxygen present in air or in a liquid environment, reacts spontaneously forming a coating with a oxide layer of a few nanometres thick. This thin layer prevents the metal of being completely oxidized, protecting it. However, from a scientific and a commercial point of view, it could be interesting to achieve a controlled oxidation process of the aluminium.

An analogous oxidation reaction can be carried out electrochemically in order to produce aluminium oxide. This process has been called “anodization”. A schematic picture of this process is illustrated in figure 2.1. On the electrodes of an electrolytic system, the aluminium is placed as the anode and platinum or graphite are used as cathode. Next, both of them are partially submerged in an aqueous dilution of an electrolyte. When a voltage is applied between both electrodes, redox reactions take

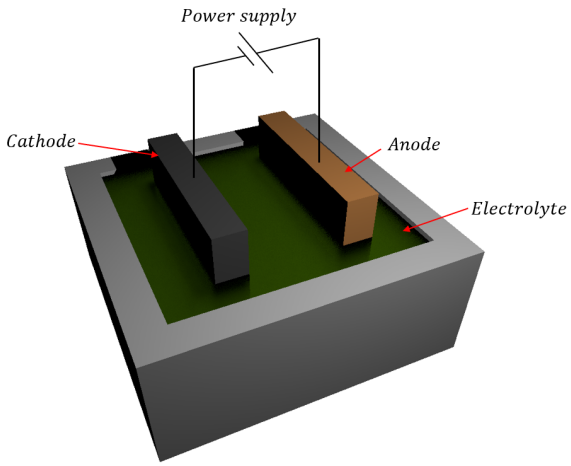

Fig. 2.1 Schematic view of the electrochemical cell for anodizing.

place on them. The aluminium is oxidized in the anode and the aluminium oxide starts to grow perpendicularly to the surface. During this process, negative charged compounds (anions) coming from the electrolyte can migrate and being incorporated into the aluminium oxide. Meanwhile, a reduction reaction occurs in the cathode producing hydrogen ions.

2.1.1 Types of anodic aluminium oxide

In this electrochemical process, the nature of the electrolyte has a crucial role on the characteristics of the oxide layer. The chemical composition of the electrolyte influences the geometrical properties of the anodic aluminium oxide (AAO). In general, the AAO is present in two distinct morphologies: barrier-type AAO and porous-type AAO. Figure 2.2 illustrates the two types of AAO. Figure 2.2.a shows the first type of AAO, the barrier-layer AAO. This AAO is formed by a compact and non-porous oxide foil, generally, using neutral electrolytes, such as citrates and borates, in which AAO is insoluble. By contrast, acid electrolytes in which the AAO is slightly soluble, such as sulphuric, oxalic and phosphoric acids, are used to produce porous-type AAO or NAA (figure 2.2.b) [Lee2014, Thompson1997]. The morphology of this last type of AAO is very different from that of barrier-layer type and, in addition, it is very sensitive to the anodization conditions, such as pH, temperature, type of electrolyte and voltage applied [[Lee2014]].

Thus, depending on the manufacturing process a porous spongiform NAA structure is obtained (the porous and ordered NAA depicted in figure 2.2.b has only illustrative purposes as a type of porous AAO and it will be described in the following sections).

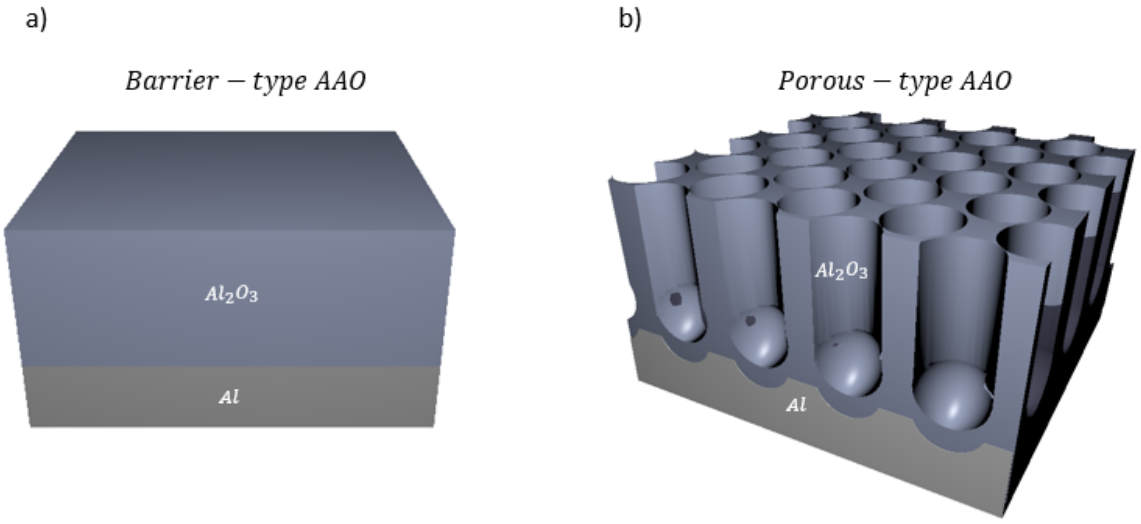

Fig. 2.2 Schematic view of the two types of anodic aluminium oxide: a) barrier-type AAO and b) porous-type AAO.

This type of NAA played an important role in industrial applications because of, among others, their hardness and resistance to the corrosion [Lee2014]. However, the porous morphology of this type of structure may not be the most suitable for nanotechnological applications based on NAA for which a good pore ordering is necessary. Actually, in order to provide some examples, research areas such as biotechnology [Ingham2012, Gultepe2010, Santos2013a] and energy [Santos2010, Balderrama2015] are investigation fields in which the degree of the NAA pore arrangement is crucial.

2.1.2 Self-ordered nanoporous anodic alumina

In 1995, Masuda and Fukuda [Masuda1995] discovered that the NAA produced by the anodization of the aluminium in a oxalic acid solution revealed a texturization of the substrate surface with an array arrangement of hemispherical concavities. From this discovery, a procedure was developed to anodize aluminium which permitted to obtain NAA films with an arrangement of highly ordered pores. This procedure was called the “two-step anodization” process. Usually the self-ordered NAA is produced using two experimental anodization process: the mild anodization (MA) process and the hard anodization (HA) process.

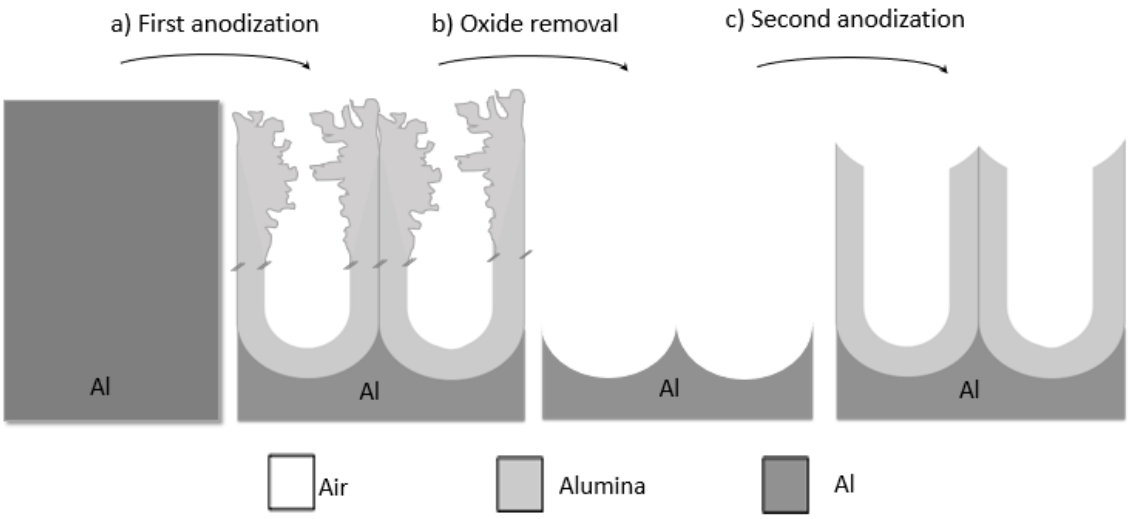

Fig. 2.3 Schematic view of the two-step anodizing process.

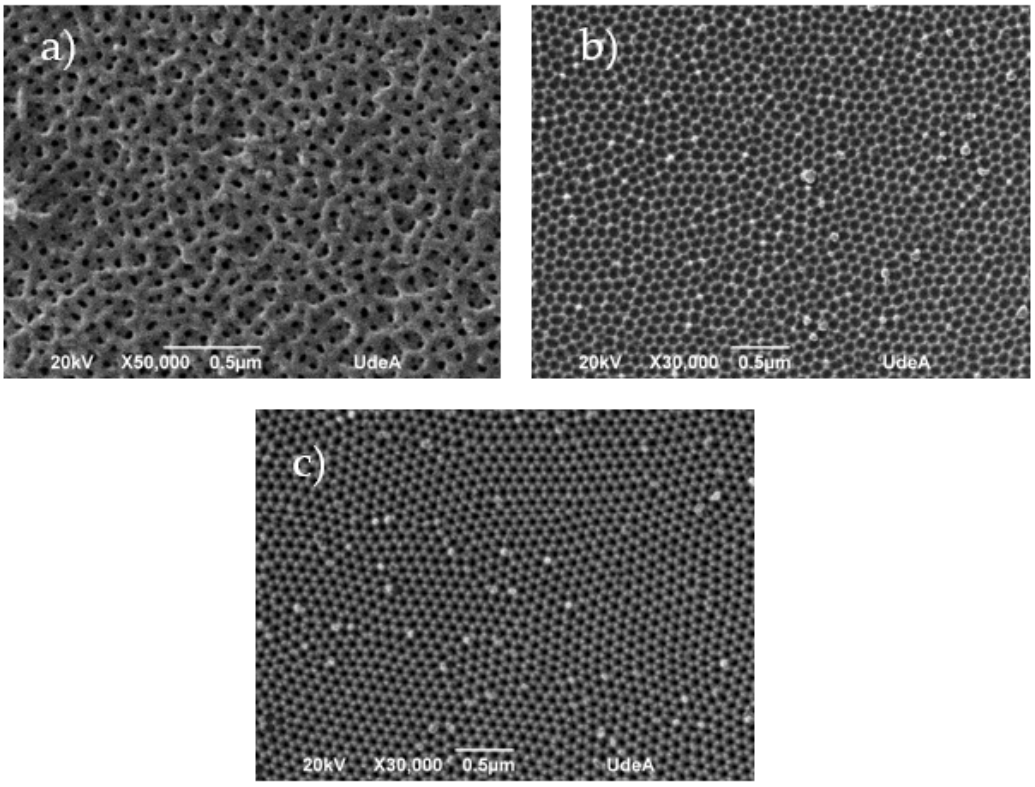

Fig. 2.4 NAA SEM top view images corresponding to the phases of the two-step anodizing process: a) first anodization, b) oxide removal and c) second anodization. Courtesy of Sara Aguilar, Universidad de Antioquia.

Mild anodization

In mild anodization, the two-step process consists of applying a first anodization which is performed in an aqueous dilution of an acidic electrolyte under potentiostatic conditions for a long time. During this first stage, the pores start to nucleate on the aluminium foil at random positions and the aluminium oxide starts to grow perpendicularly to the metal surface. The NAA resulting film shows disordered pores on the top of the oxide layer. As the pores grow into the metal, they shift their position with respect to the surface and become self-arranged in an almost-triangular lattice. This ordering of the pores is observed at their bottom after some hours of anodization. Figure 2.3 illustrates schematically the two-step anodization process, whereas figure 2.4 illustrates the SEM top view images of NAA produced with the two-step anodization process. Figure 2.3.a depicts a sketch of the first step and the figure 2.4.a shows the top view of a SEM image corresponding to a NAA sample after the first step. Subsequently, the oxide layer is removed (figure 2.3.b) unveiling a texturization of the aluminium substrate with an hexagonal array of hemispherical concavities (figure 2.4.b). At this point is when the second anodization is carried out with the same conditions as the first anodization. The pores are formed at the centre of the concavities and grow perpendicular to the aluminium surface (figure 2.3.c). Although with this procedure the obtained NAA pore arrangement can be highly ordered, it is not perfect. Figure 2.4.c shows a NAA top view SEM image after the second anodization exhibiting a polydomain structure (i.e. a structure with regions in which the lattice orientation of the pore arrangement is the same with domain walls where orientation is changed and with defect points in the lattice.). This result is according to those reported in [hillebrand2008].

The arrangement of the pores depends of the anodization conditions, such as the temperature (T), the applied voltage or potential (U), the pH and the type of acid electrolyte used. Several investigations on the self-ordering phenomenon of the porous arrangement have been published. In order to provide some examples, we cite works like this one of Masuda et al. [Masuda1997] in which the pore arrangement of NAA in a sulfuric acid solution was studied. The authors obtained a highly ordered structure with an anodization potential of 25 to 27 V. In another study, Li et al. [Li1998] discussed about the growth of highly ordered pores in NAA in a oxalic acid solution. Nielsch et al. [Nielsch2002] reported a set of conditions that allows to obtain the hexagonal array of cylindrical pores in NAA with the three major acids electrolytes (i.e. sulfuric, oxalic and phosphoric acid). Here, the authors stated the existence of an optimum anodizing potential for a specific acid electrolyte in order to obtain the finest pore ordering. That

is the so-called "self-ordered anodization regimes". In this line, the authors reported that the optimum potential to obtain the best pore ordering for the three mostly used acids electrolytes in mild anodization was: $25V$ for sulfuric acid, $40V$ for oxalic acid and $195V$ for phosphoric acid. When the anodization is performed out of the bounds of the self-ordered regimes, the pore ordering decreases extremely [Lee2014].

Previous works have focused mainly on considering the commonly three mostly used electrolytic acids for the production of the self-ordered NAA. However, some authors demonstrated the fabrication of self-ordered NAA considering other types of acidic electrolytes. For example, Ono et al. [Ono2004] reported the fabrication of a self-ordered NAA using citric acid as electrolyte and applying $240V$ as anodization potential. In a posterior work, Ono et al. [Ono2005], fabricated self-ordered NAA employing other organic acids electrolytes. In this later case, the authors used malonic and tartaric acids as electrolytes, at $120V$ and $195V$ respectively, to produce the porous alumina films. In both studies, the authors obtained NAA films with a worse spatial ordering as compared with those achieved using the conventional acid electrolytes.

Hard anodization

On the other hand, the HA process is used with hard anodization conditions (i.e. with high voltages) in order to obtain a higher growth rate of the NAA. Lee et al. [Lee2006a] investigated the NAA fabrication with this process, in a one-step anodization procedure using oxalic acid as electrolyte at low temperatures and applying high voltages such as 100–150V. The hard conditions on the voltage applied may damage the oxide film, and for this reason the authors reported that a protective oxide layer on the substrate of aluminium using MA conditions should be formed before the hard anodization process be applied. Finally, they reported a fast fabrication process with a new self-ordering regime and a highly pore ordering.

An alternative approach was developed by Santos et al. [Santos2012c]. The authors proposed an new method to obtain NAA films produced in oxalic acid without the protective oxide layer by hard anodization. To this end, the authors used a two-step process in HA: they started anodizing the aluminium substrate by MA conditions during a short period of time (5 minutes) after which the authors increased the voltage until reach the HA anodization voltage, and then a second step at HA voltage is applied with low temperature, low acid concentration and with a high stirring rate in order to provide a faster diffusion of the heat. With this work, the authors reported a cost-effective fabrication process without additional stages for obtain NAA membranes with well-defined pores.

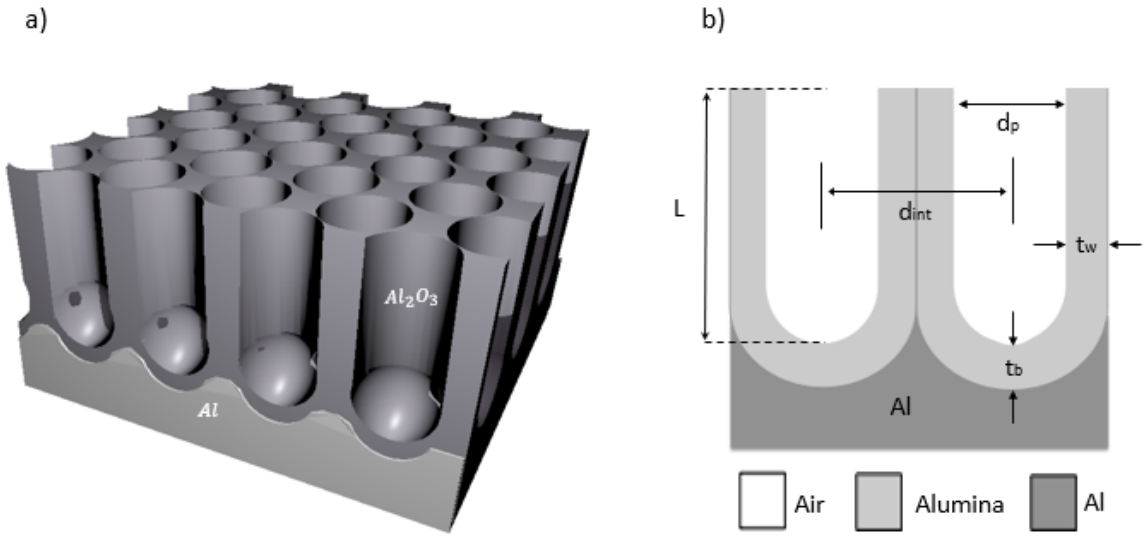

Fig. 2.5 Schematic pore morphology of NAA. a) 3D prespective view of the NAA pore morphology. b) Schematic planar cross section view of the NAA pore morphology with the geometrical parameters explicitly depicted.

This section has reported the fabrication process usually used to obtain self-ordered NAA. From now on, throughout this dissertation, the term NAA will refer to self-ordered NAA. The following section of this chapter moves on to describe in greater detail the general structure of the NAA.

2.1.3 Pore morphology of nanoporous anodic alumina

Figure 2.5 shows schematically an ideal pore morphology of the NAA. The structure shows a hexagonal arrangement of cylindrical pores perpendicular to the aluminium substrate (figure 2.5.a). The interface substrate-alumina is texturized with hemispherical concavities, as well as the interface alumina-air in the nanopores. The space between this two interfaces is a thin barrier of alumina that constitutes the barrier layer. In general, the NAA pore morphology can be characterized by a set of geometric or structural parameters (figure 2.5.b): the interpore distance (d_{int}), the pore diameter (d_p), the pore length or porous layer thickness (L), the barrier layer thickness (t_b) and the pore wall thickness (t_w).

For highly ordered NAA, we can consider an ideal hexagonal arrangement of the pores. With this distribution we can establish a relationship between some structural parameters and also with the porosity (P) of the structure.

$$d_{int} = d_p + 2t_w \tag{2.1}$$

$$P = \frac{\pi}{2\sqrt{3}}\left(\frac{d_p}{d_{int}}\right)^2 \tag{2.2}$$

As we indicated previously, numerous investigations have established that the anodization conditions strongly influences the morphology of the NAA. The applied voltage [Losic2009a, Nagaura2008, Rahman2013], the pH [Chu2006, Ono2005], the temperature [Sulka2009, Xu2004] and the acid electrolyte [Chu2006, Ono2005, Zaraska2016a] determines the resulting NAA structure, making possible engineer the NAA with desired geometrical parameters. Thus, it is convenient that the dependence of the major structural parameters with the anodization factors be briefly described.

Interpore distance

On a key study about the self-ordering regimes of the NAA, Nielsch et al. [Nielsch2002] observed that for self-ordered NAA the ratio $\frac{d_p}{d_{int}}$ was always constant, giving a value for the porosity of $P \approx 10\%$. This result was called the 10% porosity rule. Additionally, the authors reported that in the self-ordered regimes the anodizing potential influences the interpore distance. They found that for the three mostly used acids (sulphuric, oxalic and phosphoric acids) this influence follows a linear equation

$$d_{int} = \alpha U \tag{2.3}$$

where α is the proportionality constant. For this regime (mild anodization), the authors, experimentally determined $\alpha = 2.5\,nm/V$. Table 2.1 summarizes the interpore distance for the NAA achieved with the tree mostly used acids and with three additional organic acids (malonic, tartaric and citric) with the optimum anodizing potential.

On the other hand, in hard anodization Lee et al. in [Lee2006a] reported a reduction in the proportionality constant of eq. (2.3). The authors experimentally determined $\alpha = 2.0\,nm/V$, and also reported a new ranges of interpore distances for this anodization process. In order to provide comparison, table 2.2 shows the ranges of interpore distances achieved in mild and in hard anodization for sulphuric and oxalic acid electrolytes.

Table 2.1 Interpore distance for the self-ordered NAA achieved with the tree major inorganic acids (sulphuric, oxalic and phosphoric) and with three organic acids (malonic, tartaric and citric) with the optimum anodizing potential in mild anodization. Adapted from [Lee2008].

Electrolyte acid	anodizing potential (V)	interpore distance (nm)
Sulphuric	25 V	65 nm
Oxalic	40 V	103 nm
Malonic	120 V	300 nm
Phosphoric	195 V	500 nm
Tartaric	195 V	500 nm
Citric	240 V	600 nm

Table 2.2 Interpore distance for the self-ordered NAA achieved with sulphuric and oxalic acids with the optimum anodizing potential (U) in mild anodization and hard anodization. Adapted from [Lee2006a].

Electrolyte acid	Mild anodization		Hard Anodization	
	$U\ (V)$	$d_{int}\ (nm)$	$U\ (V)$	$d_{int}\ (nm)$
Sulphuric	19-25	50-60	40-70	90-140
Oxalic	40	100	120-150	220-300

Table 2.3 Pore diameter for the self-ordered NAA achieved in mild anodization with the tree major electrolyte acids (sulphuric, oxalic and phosphoric) with the 10% porosity rule. Adapted from [Nielsch2002]

Electrolyte acid	anodizing potential (V)	Pore diameter (nm)
Sulphuric	25 V	24 nm
Oxalic	40 V	31 nm
Phosphoric	195 V	158.4 nm

Pore diameter

In the study provided by Nielsch et al. in [Nielsch2002], the authors reported that in contrast to the interpore distance, the pore diameter is influenced by the pH of the electrolyte solution. They reported that the potential necessary for an optimal self-ordering anodization is lower for lower pH. Table 2.3 summarizes the pore diameter for the NAA achieved with the tree major inorganic acids (sulphuric, oxalic and phosphoric) with the 10% porosity rule.

Additionally, they also reported that under the 10% porosity rule and with the equations (2.3) and (2.2), a relationship between the anodizing potential and the pore diameter is also obtained.

$$d_p = \sqrt{\frac{2\sqrt{3}P}{\pi}}\alpha U \tag{2.4}$$

Pore diameter modulation

The self-ordering anodization process described previously permits to obtain a highly ordered NAA with a specific range of d_p and d_{int} in the self-ordered regimes. This procedure permits to obtain NAA structures with well-aligned cylindrical pores perpendicular to the aluminium substrate. However, as we have seen before, the pore diameter of the NAA strongly depends on the applied voltage. Thus, the production of NAA films with a modulation of the pore diameter in depth is possible and it can be engineered by a precise control of the anodization voltage or the current density in the fabrication process. This structural modulation of the pore morphology in depth can be achieved using different anodization techniques.

In this work, we consider two pore modulation procedures of anodization: the pulse anodization (PA) and the cyclic anodization (CA). The PA is one of the most studied pore modulation procedure [Lee2008, Chen2015, Lee2008a]. This procedure permits to fabricate NAA structures breaking the cylindrical shape of the pores and giving a 3D pore morphology to the NAA combining a low-potential pulse followed by another high-potential pulse with periods and amplitudes intentionally designed. Figure 2.6 illustrates a schematic view of the NAA pore morphology achieved with the pulse anodization process. The picture shows the variation of the pore diameter in depth of the structure. The pore geometry can be defined by two sections of pore lengths: the corresponding to the achieved by a high-potential pulse, Λ_{high}, and the corresponding to the achieved with the low-potential pulse, Λ_{low}. The length in depth of each section it will depend of the time of the applied pulse.

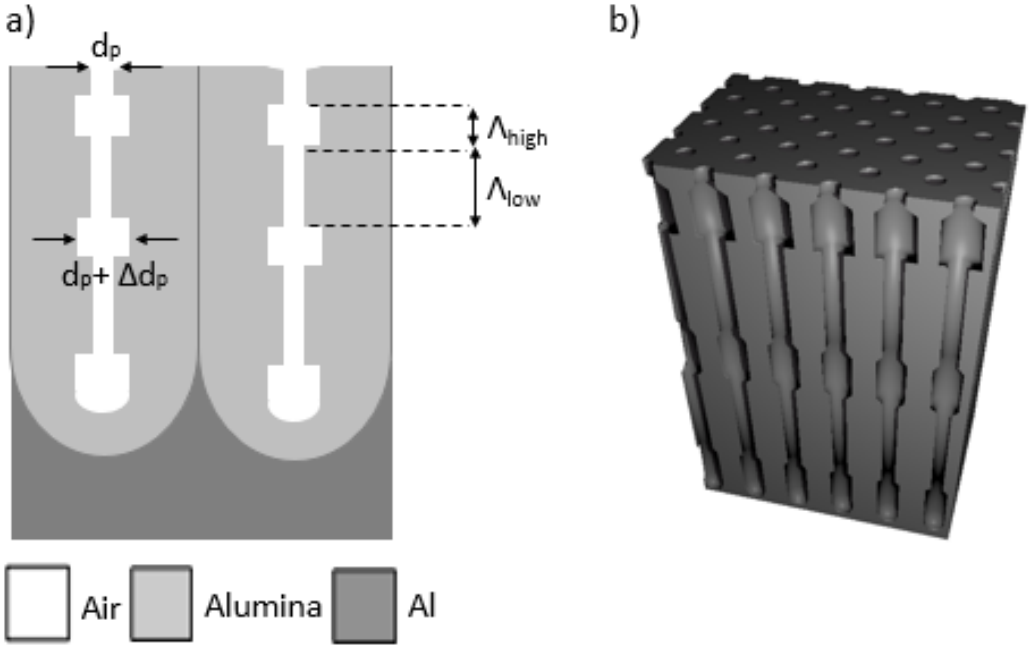

Fig. 2.6 Schematic NAA pore structure with pulse anodization: (a) 2D planar cross section sketch and (b) 3D perspective view sketch.

Another type of procedure to modify the NAA pore morphology is the so-called "cyclic anodization". Losic et al. [Losic2009a] developed this procedure employing periodic oscillating parameters in the anodization current to achieve, for instance, NAA-based rugate filters (NAA-RFs). NAA-RFs are a NAA-based structures where their pores have a periodical oscillation of their diameter with the depth. Figure 2.7 illustrates a schematic view of the NAA structure achieved with this cyclic anodization process. In the picture we can observe the sinusoidal variation of the pore diameter (Δd_p) on the pore length period (Λ). This sinusoidal pore morphology can be achieved by applying a sinusoidal anodization current profile such as:

$$I(t) = I_0 + I_1 sin(\frac{2\pi t}{T}) \tag{2.5}$$

where I_0 is an offset current (equivalent to the anodization current in constant current anodization), and I_1 and T are the amplitude and period of the sinusoidal component. As a example, Ferré-Borrull et al. [Ferre-Borrull2014] fabricated NAA-RFs using the cyclic anodization process by a variation of the current from galvanostatic conditions. They applied a sinusoidal profile of the current similar to that of the eq. 2.5 to create the pore modulation in depth. The authors concluded that different sinusoidal current components can be superimposed. Also, they demonstrated that is possible to

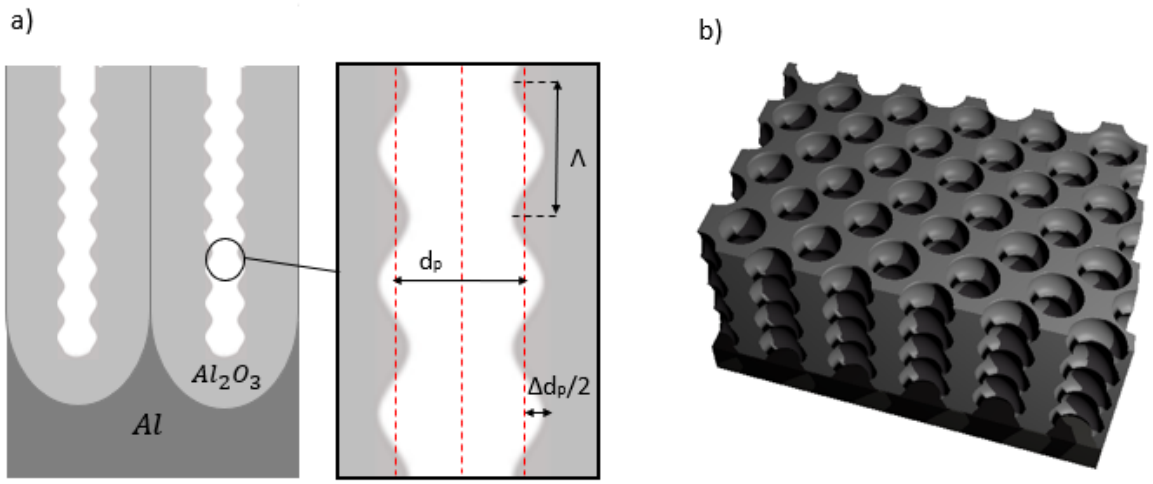

Fig. 2.7 Schematic NAA pore structure with cyclic anodization: (a) 2D cross section planar sketch and (b) 3D perspective view sketch.

modulate both the average diameter and the amplitude in the diameter variation and in the period. Finally, the investigators reported that the pore widening contributes to increase the contrast between minimum diameter and maximum diameter.

Barrier layer thickness

The growth mechanism of NAA is highly influenced by the barrier layer thickness (t_b) which is considered one of the most important structural parameters of NAA [Vrublevsky2005]. This parameter is also dependent on the anodizing potential. Nielsch et al. [Nielsch2002] reported that the thickness of the barrier layers in mild anodization satisfies the relationship

$$t_b \approx d_{int}/2, \tag{2.6}$$

condition that prevents the pore nucleation between the existing pores.

Structure of the pore wall

The anodization process of the aluminium does not only determines the geometrical parameters of the NAA, but also the chemical ones. During this process, a transport of anionic species coming from the acid electrolyte towards the aluminium oxide occurs [Shimizu2000, Shimizu2001]. The amount of incorporated anions and their spatial distribution in the NAA structure depends on the acidic electrolyte and on the anodization conditions [Lee2014]. The pore morphology of the NAA is affected by this

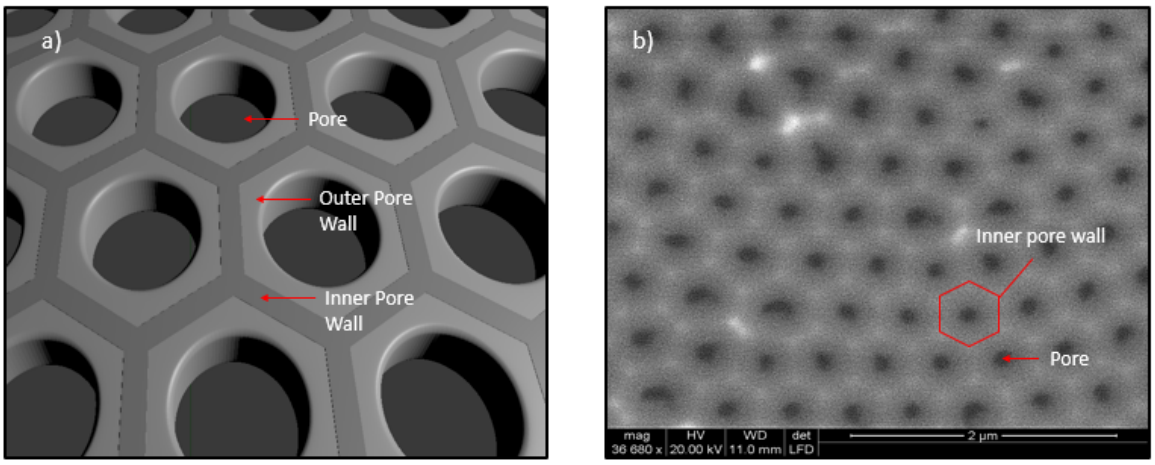

Fig. 2.8 a) Schematic dual layer structure of the pore wall of NAA. b) Top view SEM image of NAA produced with phosphoric acid electrolyte showing the structure of the pore wall. Courtesy of Laura Pol, Universitat Rovira i Virgili.

incorporation revealing a chemical layered structure in the pore wall oxide. Thompson in [Thompson1997] reported that the chemical composition of the pore wall shows a dual layer structure: the so-called “outer pore” wall layer and the “inner pore ” wall layer. The authors also reported that the outer pore layer consists in a pore wall layer with a higher concentration of anions than the inner pore layer which remains relatively pure. Figure 2.8.a shows a schematic picture of the dual layer structure of the pore walls of NAA whereas the figure 2.8.b shows a top view SEM image of NAA produced with phosphoric acid electrolyte showing the structure of the pore wall. The SEM image reveals the cell boundary (highlighted in red) that corresponds to the inner pore wall whereas the material surrounding the pores corresponds to the outer pore wall.

Other researchers, however, have found that the anions were distributed in an onion-like manner. Specifically, Santos et al. [Santos2014a] reported four chemical layers for the pore wall with decreasing concentrations of anionic species from the outer pore wall to the inner pore wall (figure 2.9.b).

In any case, the incorporation of the anionic species to the NAA affects the refractive index of the aluminium oxide in comparison with the relatively pure alumina. This will depend on the type of the anionic species migrated (sulphate, oxalate, and phosphate), which in turn depends basically on the acidic electrolyte used in the anodization process [Santos2013a].

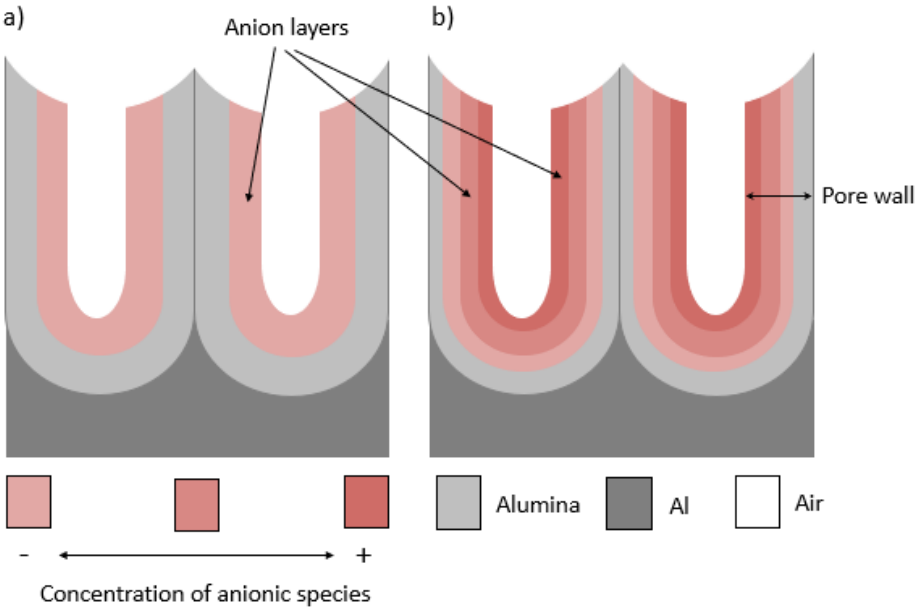

Fig. 2.9 a) Schematic cross section of the dual layer structure of the pore wall of NAA. b) Schematic cross section of the four layer structure of the pore wall of NAA showing the decreasing concentration of anionic species by layer.

2.2 Optical properties of nanoporous anodic alumina

The main optical properties of NAA are reflectance, transmittance, absorbance and photoluminescence (PL). These are very related with the nanoporous structure of the NAA and their chemical composition [Santos2014]. Therefore, the fabrication conditions and the structural design of the NAA are determinant aspects to control the optical properties of the NAA. This pronouncement has been widely reported in the literature. For example, Marsal et al. [Marsal2009] reported the influence of the alumina thickness and the temperature on the transmittance. The authors measured the optical transmission spectra of NAA films with different thickness and temperatures, and determined the dependence of the complex refractive index with the temperature and crystalline phase. The influence of the main structural parameters on the optical NAA properties was investigated in works such as that of Kumeria et al. [Kumeria2012]. Here, the authors studied the optical properties of the NAA reporting the influence of d_p, d_{int}, L and the modification of the surface by for example metal deposition (Au, Ag) in these. In a posterior study, Kumeria et al. [Kumeria2014b] demonstrated that the nanoengineering of the NAA structural parameters, such as the

pore diameter and the pore length, were critical in the development of more sensitive and efficient optical sensors. The authors also reported that the 3D modulation in depth of the NAA pore diameter improved the optical performance of the devices based on them. In this line, Ferré-Borrull et al. [Ferre-Borrull2014a] studied the applied voltage cycles and the temperature on NAA-based distributed Bragg reflectors (i.e. a NAA structure which its pore diameter varies in depth inducing a periodic variation in depth of the refractive index of the structure). The authors reported the possibility of tuning and enhancing the photonic stop bands (i.e. range of wavelengths where the propagation of the light through the photonic crystal in one or several directions is forbidden) when combining with the temperature and a pore widening procedure.

Concerning other optical properties such as photoluminescence , Santos et al. [Santos2012], in a exhaustive study, reported that the PL properties of the NAA were related to the structural parameters and also to the acid electrolyte. Li et al. [Li2007a] investigated the influence of the acid electrolyte on the PL spectrum of the NAA. Cantelli et al. [Cantelli2016] studied the effect of the anodization temperature on the NAA photoluminescence spectra. The authors reported an increase on the number of the Fabry-Pérot fringes with the increase of the electrolyte temperature; meanwhile, in contrast, a decrease of the oscillation amplitude with the temperature ascent was observed.

The optical methods commonly used in the detection of the optical signals are diverse. According to the optical properties, these can be used as a detection principles in the development of NAA-based sensors or biosensors. We can cite, for example, optical sensing based on surface plasmon resonance (SPR), localized surface plasmon resonance (LSPR) , surface enhanced Raman scattering (SERS) and reflectometric interference spectroscopy (RIfS). In the next paragraphs these optical methods are briefly described and also are summarized in table 2.4.

Surface Plasmon Resonance (SPR)

SPR is based on the excitation of the surface plasmons of a metal film when light impinges on it. Usually, the optical system is implemented using the Kretschmann configuration, which consists of illuminating a triangular prism so that the light beam is incident on the base of the prism from the glass medium (figure 2.10). The base of the prism is coated with a very thin film of the metal. If the angle incident on the base of the prism is corresponds to the wavevector of the SPR, incident photons

Table 2.4 Summary of optical sensors and biosensors based on Nanoporous Anodic Alumina (NAA) platforms: optical method, analyte and reference.

Optical method	Analyte	Reference
SPR	octadecyl-phosphonic acid	[Koutsioubas2008]
	BSA	[Lau2004]
	BSA	[Hotta2012]
LSPR	ethanol	[Konig2014]
	aptamers	[Kim2008]
	Pseudomonas aeruginosa	[Kim2017]
SERS	Rhodamine 6G (R6G)	[Mondal2010]
	IgG	[Fu2014]
	mouse neuroblastoma N2a cells	[Toccafondi2015]
RIfS	IgG	[Alvarez2009]
	H2S gas	[Kumeria2011a]
	BSA	[Macias2013]
PL	trypsin	[Santos2012b]
	oxazyne, glucose	[Santos2012b]
	ethanol	[Laatar2017]

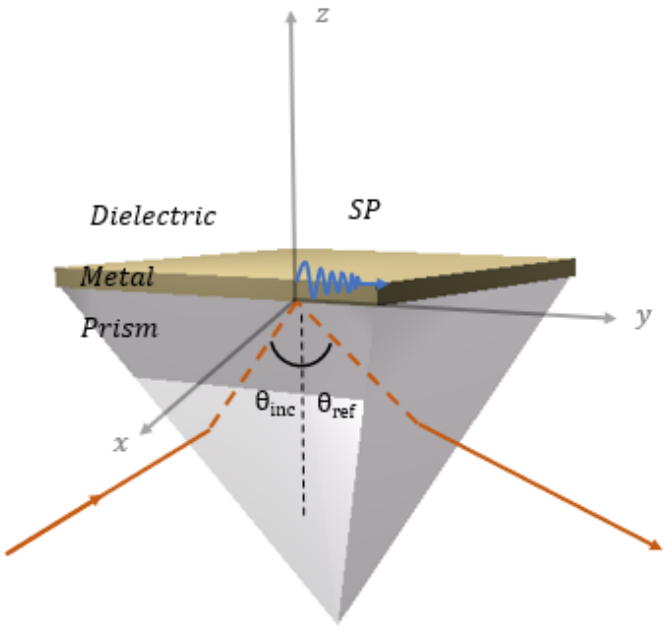

Fig. 2.10 Schematic view of the Kretschmann configuration for surface plasmon excitation.

are coupled to the SPR. The sensing principle of the system lies in the fact that the SPR is hugely sensitive to changes in the refractive index of the medium surrounding the metal coating on the side opposite to the prism up to distances of a few hundred of nanometres from the metal surface. Taking advantage of that, Koutsioubas et al. [Koutsioubas2008] investigated the signal enhancement of a SPR-NAA based sensor. In another study, Lau et al [Lau2004] demonstrated the detection of bovine serum albumin (BSA) adapting NAA as SPR planar optical waveguide. Hotta et al. [Hotta2012] developed a free-label biosensor based on a NAA waveguide on a aluminiumsubstrate. The authors investigated the adsorption of BSA by the NAA and reported a 20-times higher sensitivity than conventional SPR sensors.

Localized Surface Plasmon Resonance (LSPR)

When illuminating metallic particles with sizes much smaller that the wavelength of the incident light, the plasmons at the metallic surface become excited and oscillates around the particle with a characteristic resonant frequency called LSPR [Willets2007, Anker2008]. The LSPR shows an extreme dependence on the geometric nature of the nanoparticle such as the size and the geometry, as well as on their composition [Petryayeva2011]. The LSPR, as well as the SPR, is also very sensitive to changes in the refractive index of the surrounding medium. In addition, the size, the shape, the material and the properties of the medium influences the LSPR. König et al. [Konig2014] infiltrated silver nanocubes into the pores of the NAA to investigate the LSPR coupling between them. The authors reported a high plasmonic sensitivity for the system in contrast to conventional planar substrates. Kim et al. [Kim2008] studied the detection of biomolecules (aptamers and proteins) by means of LSPR on a gold-capped NAA nanostructure. In a more recent work, Kim et al. [Kim2017] developed a gold-capped NAA chip for the detection of a specific type of bacterial cells. The combined action of the interferometry and the LSPR enhanced the optical response of the system. Thus, the authors reported reproducible changes in the wavelength peak and in the relative reflected intensity (RRI) in presence of the bacterial cells.

Surface-Enhanced Raman Scattering (SERS)

Surface-enhanced Raman scattering (SERS) is based on the enhancement of Raman scattering of an analyte on the surface of a roughened metal or nanostructured surface [Zhang2008a]. The surface-enhanced Raman effect mainly lies in the enhancement of the electromagnetic field at the metal surface because of coupling of the incident

light to the LSPR. Since Raman emission of a specific molecule depends with the fourth power of the electric field at the point where the molecule is placed, field enhancement results in a boost of the Raman signal. The nanostructured surface of the NAA is a suitable platform to build up SERS substrates. In this line, Mondal et al. [Mondal2010] fabricated a SERS substrate using a NAA membrane decorated by silver nanoparticles. When the silver was deposited the lattice arrangement of the nanoparticles by the NAA nanostructuration provided the adequate roughness to create the huge SERS effect. Additionally, as the NAA nanostructure can be exquisitely tuned, the authors reported the possibility to design and produce NAA-based SERS substrates to achieve a control of the field enhancement in a precise way. Other studies have used a NAA as a waveguide to sensing biomolecules by SERS. Fu et al. [Fu2014] proposed a highly sensitive SERS detection device by means of a NAA waveguide and assembled silver nanoparticles. Another investigation on SERS-NAA platform was performed by Toccafondi et al. [Toccafondi2015] in which the authors investigated the suitability of gold-coated NAA as a biosensor. They used gold-coated NAA as a SERS surface and performed Raman measurements on living cells cultured on the gold-coated NAA structure. The analysed Raman peaks corresponding to the distinct components of the cells with this nanostructured substrate showed a remarkable enhancement of the Raman effect in comparison with the corresponding ones obtained with different substrates.

Reflectometric Interference Spectroscopy (RIfS)

Reflectometric Interference Spectroscopy (RIfS) is a label-free optical method based on the interference pattern obtained when white light impinges and go through a thin film. The interference pattern is due to the overlap of the multiple reflections of the incident beam at the thin film interfaces. The optical path difference ($2nL$) between two consecutive reflected wave fronts gives the condition for constructive or destructive interference of the overlapped reflected components at each wavelength. Such constructive and destructive interferences give rise to maxima and minima (interference fringes) in the reflectance spectrum. Changes the optical path will be translated into a modification of the number, the position and the intensity of the interference fringes [Kumeria2012]. Thus, as the interference pattern depends on the pore morphology, to achieve a precise control of the fabrication conditions is crucial to design NAA structures with determined optical properties. RIfS-NAA based platforms have been developed for sensing and biosensing applications. Alvarez et

al. [Alvarez2009] developed a NAA biosensor to detect binding of immunoglobulin. Changes in the refractive index of the layer because of the binding of the proteins were detected by thin film interference spectroscopy. Kumeria et al. [Kumeria2011a] used NAA for reflective interferometric sensing of volatile sulphur compounds. Macias et al. [Macias2013] demonstrated the use of gold-coated NAA bilayers (NAA with large pore diameters on the top layer and small pore diameters in the bottom layer) for biosensing by means of RIfS. The authors evaluated the sensing capabilities of this structure with bovine serum albumin. Kumeria et al. [Kumeria2014] engineered and optimized NAA rugate filters for biosensing aplications. The authors assessed their results with distinct solutions of glucose and validate them by a theoretical model.

Photoluminescence (PL)

Photoluminescence (PL) is the light emission by a material after being excited by means of electromagnetic radiation. The NAA can emit blue light under light excitation. Several authors reported that this phenomenon can be related to the anions distribution and concentration in the alumina matrix [Huang2003, Li2007a]. Another source of photoluminescence in NAA is the presence of oxygen vacancies in the aluminiumoxide molecular lattice. Such vacancies are also known af $F+$ or $F++$ colour centres, depending of the oxidation number of the vacancies [GopalKhan2013, Mukhurov2010].

Taking advantage of this kind of investigations, the use of PL-NAA based platforms in sensing or biosensing was reported in the literature. For example, Santos et al. [Santos2012b] developed a enzymatic sensor based on PL-NAA. The authors monitored the PL spectra of the NAA platform before and after the enzyme immobilization, detecting and quantifying it. Additionally, the authors also reported that the tunability of the structural parameters of the NAA structure (pore diameter and pore length) permitted improving and optimizing the enzyme detection. In another work, Santos et al. [Santos2012a] developed an encoding system based on the PL spectrum of the NAA. The authors reported the possibility of producing barcodes based on the width and the position of each bar, which in turn were related to the intensity and position of each oscillation of the spectrum. Concerning chemical sensing, Laatar et al. [Laatar2017] developed and employed a PL-NAA platform as a gas sensor. The authors embedded $CdSe$ nanoparticles into the NAA for the detection of ethanol under white illumination, enhancing the sensor sensitivity.

In consequence, as the aforementioned studies have demonstrated, engineering the structural parameters of the NAA by adjusting the fabrication conditions is a key

parameter to design and enhance the optical properties of the NAA in order to develop optical devices based on them. Therefore, in order to help to achieve a deep understanding on the optical properties of the NAA and to help to predict results, theoretical studies using numerical simulation models are decisive. Additionally, these investigations become crucial in the sense that they help in the optimization of devices based on NAA, favouring a reduction in the production time and also in the costs.

2.3 Simulation of the optical properties of NAA

This section is intended to be a review of researches referred to the simulation of the optical properties of porous materials, such as porous silicon (PSi) and NAA, with the most commonly methods for optical modelling. From the wide variety of methods for optical modelling existing in the literature, the commonly used to simulate the optical response of these porous materials are: the transfer matrix method (TMM), the finite difference in the time domain method (FDTD), the scattering-matrix method (SMM) and the rigorous coupled-wave analysis (RCWA). Chapter 3 will show the details of each method used in this thesis.

The transfer matrix method is a faster and simple numerical method that permits to model the propagation of electromagnetic waves through a multilayer thin film system. TMM is usually used in combination with an effective medium approximation (EMA) which makes possible approximate the 3D porous material towards a 1D-multilayer structure, such as a 1D-photonic crystal. Using this method as a computational tool with the Bruggeman's EMA (details will described in the next chapter), Patel et al. [N.Patel2012] simulated the optical properties of diverse porous silicon (PSi) structures: a single layer PSi structure, a distributed Bragg reflector (DBR) and a micro cavity (MC) as a more complex structure respectively. For the single layer structure, the reflectance spectrum was calculated using the effective optical thickness ($2nL$) of the whole structure. For the multilayer structures, the stack of layers were designed considering alternate layers of low refractive index with high refractive index. In a similar investigation , Maniya et al. [Maniya2014a] also employed the same modelling approach on a DBR-PSi structure. In the same line, a investigation was carried out by Mukherjee et al. [Mukherjee2013] studying the optical response of multi-layered PSi structures. The authors verified the calculated results on simulated structures considering superposition and sequential addition of refractive index profile functions with those obtained experimentally. Suárez et al. [Suarez2012] studied the sensing

capabilities of a PSi structure with a polymer layer added to the pore walls. Here, micro cavities and rugate filters structures were fabricated and also modelled with the Bruggeman's EMA and simulated with TMM.

When the subwavelength features of a 3D structure (that optically behaves like a 2D or 3D-photonic crystal) have to be considered, the scattering-matrix method (SMM) and the RCWA can be useful to obtain reflectance and transmittance calculations. Vonn Freymann et al. [VonFreymann2003] studied the diffraction properties of a 2D-PSi photonic crystal. To this end, the SMM simulations permitted the authors to obtain the reflectance and transmittance calculations corresponding to the diffracction spectra and being compared with experimental measurements. In this line, Deubel et al. [Deubel2004, Deubel2005] fabricated 3D photonic structures by direct laser writing. The authors used SMM to asses the high quality of the produced samples. They calculated the optical transmission and the angular dependence of the optical transmission spectra of a 3D-photonic crystal and validated them by experimental measurements. Sai et al. [Sai2006] proposed a technique to produce antireflective subwavelength silicon (Si) structures based oh NAA templates. The authors performed numerical simulations based on RCWA to estimate the optical properties of Si SWS surfaces. They reported experimental reflectivities below 1% over a wide spectral bandwidth as expected by numerical simulations.

Another one of the most used numerical methods is FDTD. Although it is computationally intensive, its demonstrated ability to take into account all the geometric complexities of the nanostructure, its accuracy and its rigour make it a good election. In this way, Rahman et al. [Rahman2011] simulated the transmittance spectra of NAA-patterned macroporous silicon by means of FDTD in order to study the existence of photonic band gaps. Block et al. [Block2005] performed reflectance and sensitivity simulations of a photonic crystal biosensor based on a porous glass device and compared with the experimental results. The simulations were performed with RCWA which provided the initial modelling and later were validated by FDTD. Chen et al. [Chen2016] theoretically investigated by means of 3D FDTD method the plasmonic absorption and the sensing performance of a 3D-array of rectangular nanoholes structure. This structure consisted in a dielectric layer placed between two nanopatterned gold thin films. Kee et al. [Kee2012] studied the optical biosensing capabilities of an hexagonal array of nanoholes on a gold-coated free standing Si_3N_4. The plasmonic effects and the structure sensitivities were investigated by means of FDTD method varying the gold

coated thickness, the hole diameter and the period of the lattice in order to obtain the optimum characteristics for fabricate the biosensor. A similar investigation was carried out by Cetin et al. [Cetin2015] on a hybrid substrate with silicon nitride. The authors performed the numerical simulations with FDTD on the plasmonic device to optimize the structure. The experimental results with the hybrid substrate were compared with those achieved with transparent substrates.

Focusing on the simulation of the optical properties of NAA structures, more specific investigations were found in the literature. Concerning the study of the optical response of complex pore morphology NAA structures, Rahman et al. [Rahman2013] simulated the optical properties of a NAA-based DBR with an EMA with TMM. In another work, Hernández-Eguía et al. [Hernandez-Eguia2014] studied the optical Fabry-Pérot interference pattern of single layer of NAA coated with gold on a substrate of aluminium. A theoretical model based on EMA with TMM was proposed and validated with experimental measurements. In another work, Král et al. [Kral2009] calculated the angular-dependence reflectance and the polarimetry spectra of NAA-based photonic crystal slabs. The authors simulated it in two different lattice structures using SMM to study and characterize this kind of NAA photonic crystals. Damm et al. [Damm2014] modelled plasmonic effects of free-standing gold nanorods with FDTD. The authors embedded gold nanorods in a NAA structure produced with sulfuric acid electrolyte for SERS and surface enhanced fluorescence (SEF). Li et al. [Li2014] used FDTD to study the optical properties of gold-coated NAA in relation with the structural parameters. The authors investigated the change of the structural colour varying the pore diameter in a range from 20 nm to 90 nm. The simulations indicated that the colour of the NAA film can be tuned changing the pore diameter.

The work that we present in this Ph. D. Thesis comes to cover an appreciable gap in the majority of these previous investigations. Most of these works are based on NAA which characteristic sizes are smaller than the wavelength of the incident light. In our work, we studied the suitability of the numerical method chosen in order to deal with all the geometrical features of the NAA depending on these characteristic sizes. As a result of this investigation, we develop a computer model suitable for a wide range of structural parameters that takes into account the geometrical features inherent to the fabrication process and even able to consider some chemical composition features in it.

Chapter 3

Numerical methods for photonic structures based on NAA

This chapter is devoted to the numerical methods used in this Ph. D. Thesis for the study of photonic structures based on NAA. This research cannot be addressed using a single numerical method due to the different types of structures to be considered. Thus, from the different techniques existing in the literature on numerical modelling, the chosen for our investigation had been restricted to those more widely used for the kind of structure we consider.

The first section of this chapter will provide an introduction to the Effective Medium Approximation (EMA) techniques. Although that is not a numerical method that permits to calculate the reflectance of the transmittance spectrum of a NAA structure, EMA permits to determine the effective refractive index of the nanostructured alumina oxide as a mixture of materials. This approach permits to consider the 3D structure of the NAA as a 1D-multilayer system.

Next, the Transfer Matrix Method (TMM) is introduced. TMM is a numerical method for the study of the optical properties of a thin film multilayer system. This method is based on the modelling of propagating and reflecting waves through the interfaces of a layered or multi-layered structure. Usually this method is used in combination with EMA.

For the analysis of the NAA considering its geometrical features (i.e. as a 2D-dimensional photonic crystal), we introduce the fundamentals of Finite-Differences in the Time Domain (FDTD) method. This is a rigorous and accurate method that permits the analysis of the reflectance and transmittance spectra taking into consideration all the subwavelength features of the NAA structure.

Finally, a brief description of other numerical methods such as rigorous coupled-wave analysis method (RCWA) and the finite element method (FEM) are given.

3.1 Modelling the NAA as a mixture of materials: effective medium approximation

The effective medium approximation (EMA) is not a numerical method in "strictus" sense. EMA can be considered as a method to compute the effective refractive index of a subwavelength structure (NAA in this case). As an approximation, EMA does not consider all the characteristic features of the nanostructure, such as the geometric arrangement of the pores, the diameters of the pores and the inter-pore distances. Instead, this method employs a combination of the refractive index of each material that compounds the nanostructure with its volumetric fill factor in order to determine the effective refractive index of the corresponding mixture of materials. Figure 3.1 illustrates schematically the NAA pore structure in terms on the refractive index of each material component and its approach when the EMA is applied. Figure 3.1.b shows a schematic of the NAA structure in which the porous material (treated as a mixture of NAA and air) is approximated by a layer with a resulting effective refractive index. The distribution in the Z direction of the effective refractive index of the whole structure is plotted in figure 3.1.c.

Nevertheless, as we have seen in Chapter 2, the optical properties of the NAA are affected by its nanostructure. The pore morphology of the NAA, consisting in cylindrical empty pores with compact pore walls, influences the dielectric response of the structure. Thus, when the geometric features of the NAA are much smaller than the wavelength of the incident light (i.e. NAA structures produced with sulfuric and oxalic acid electrolytes in mild anodization), retardation effects (i.e. effects due to the finiteness of the speed of the light) can be neglected and EMAs can be applied. On the other hand, for NAA with geometric features in the order of incident light wavelength or bigger (such as those prepared with phosphoric acid electrolyte), other methods (such as FDTD) are needed to deal with all the geometrical features of the NAA.

The effective medium approximations (EMAs) most commonly used are the Bruggeman's EMA [D.A.G.Bruggeman], the Maxwell-Garnet EMA [Markel2016] and the Lorenz-Lorentz EMA [Han2014]. The three EMAs assume that the constituent particles are approximately spherical and with sizes much smaller that the wavelength of the incident light. Additional EMAs can be used depending on the topology of the

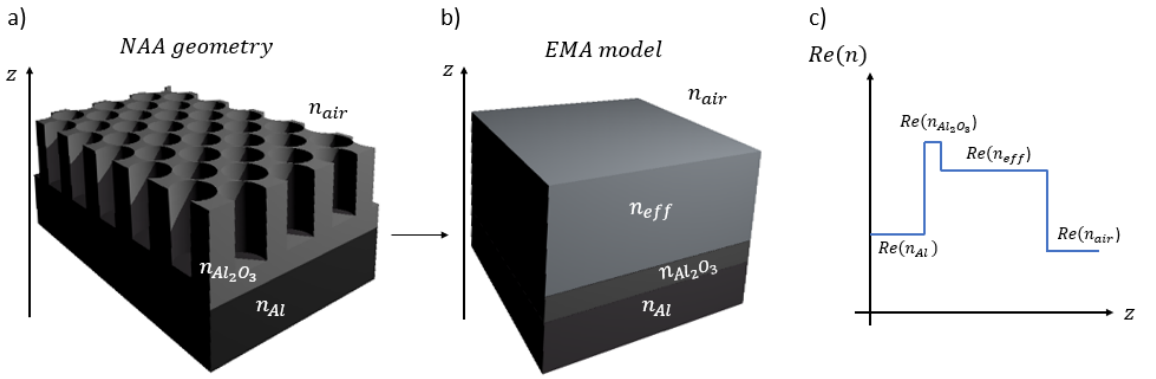

Fig. 3.1 (a) Schematic of NAA pore structure, (b) schematic of NAA pore structure considering the effective refraction index for the porous material and (c) plot of the real part of the effective refractive index in the Z direction.

NAA, such as Looyenga-Landau-Lifshitz (3L) EMA and Graded-index EMA. In the next paragraphs all these effective medium approximations are briefly described.

3.1.1 Maxwell-Garnet EMA

The Maxwell-Garnet EMA can be considered when the structure to model is formed by a homogeneous mixture of two components (labeled as 1 and 2). In this approximation, the material 2 (material with lower amount) is surrounded by the material 1. Therefore, the volumetric fill factor (f_2) is lower than the corresponding for the material 1.

The equation for the obtention of the effective refractive index of the resulting medium is

$$\frac{n^2 - n_1^2}{n^2 + 2n_1^2} = (1 - f_1)\frac{n_2^2 - n_1^2}{n_2^2 + 2n_1^2} \tag{3.1}$$

where n_1 and n_2 are the complex refractive index of each material, f_1 is the volume fill fraction of the material 1, and n the effective refractive index to be computed [Han2014]. Note that the model requires

$$f_2 = 1 - f_1 \tag{3.2}$$

3.1.2 Bruggeman EMA

The Bruggeman's EMA is appropriate for structures with more of two material components giving an effective medium which refractive index is related to the constituent materials. The equation that provides the effective refractive index for a mixture of several materials are

$$\sum_{i=1}^{N} f_i \frac{n_i^2 - n^2}{n_i^2 + 2n^2} = 0 \tag{3.3}$$

where n_i are the complex refractive index of each material, f_i are the volume fill fraction of each material, i is the optical constant for each component and n the effective refractive index to be computed.

3.1.3 Lorentz-Lorentz EMA

Another EMA that can deal with more of two components is the Lorentz-Lorentz EMA. Using the same notation as the Bruggeman's equation, the Lorent-lorentz equation takes the form

$$\frac{n^2 - 1}{n^2 + 2} = \sum_{i=1}^{N} f_i \frac{n_i^2 - 1}{n_i^2 + 2} \tag{3.4}$$

3.1.4 Looyenga-Landau-Lifshitz EMA

Despite of previous EMAs are the most commonly and successfully used approximations, we also consider another model to describe the effective medium approximation. Alekseev et al. [Alekseev2007] reported that the so-called Looyenga-Landau-Lifshitz (3L) model was specially reliable for porous silicon structures. Concerning the NAA, Santos et al. [Santos2016] applied the 3L model to NAA rugate filters (NAA-RF). The authors correlated its experimental measurements with the predictions of the 3L model, demonstrating the the NAA-RF structure can be described by the EMA.

The 3L EMA equation for the effective refractive index of the medium is

$$n^{2/3} = \sum_{i=1}^{N} f_i n_i^{2/3} \tag{3.5}$$

where n_i are the complex refractive index of each material, f_i are the volume fill factors, and n the effective refractive index to be computed. And of course, it is required that the equation

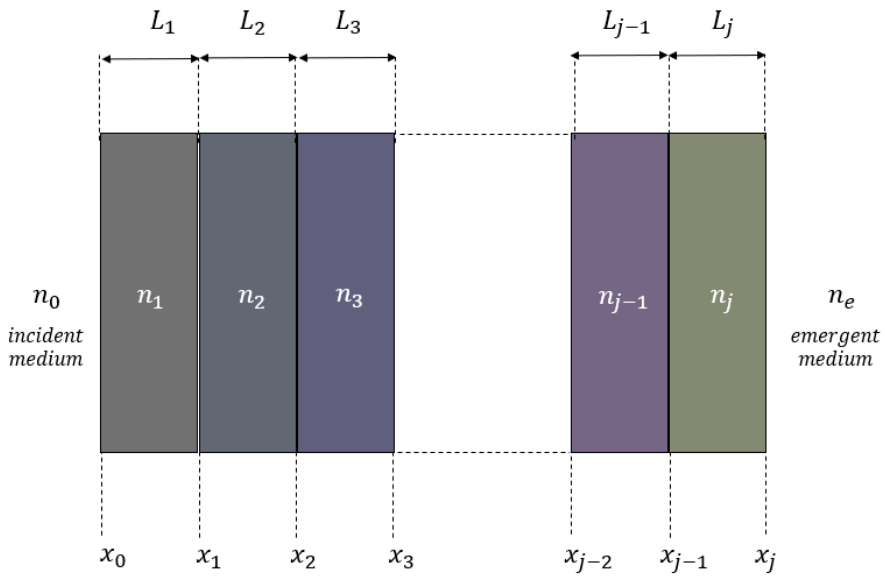

Fig. 3.2 Schematic view of a multi-layered system composed of j layers of a isotropic material with refractive n_i and thickness L_i respectively.

$$\sum_{i=1}^{N} f_i = 1 \tag{3.6}$$

be satisfied.

3.2 Transfer Matrix Method

TMM is a numerical method for the study of the optical properties of a thin film layers system. This method is based on the modelling of propagating electromagnetic waves through the layers and interfaces of a layered or multi-layered structure. TMM is based on the fact that if the electric field is known at the incident medium of the layer, then according to the Maxwell's equations and their boundary conditions continuity, the field at the end of the layer can be calculated by simple matrix calculations.

In order to study the reflectance and the transmittance of electromagnetic waves through a multilayer system we followed the same development performed by Cos in [Cos2011]. The considered structure is the illustrated in the figure 3.2. The figure is a schematic view of a multi-layered system composed of j layers of a isotropic material with refractive n_i and thickness L_i respectively.

The refractive index profile for this one-dimensional structure is defined as

$$n(x) = \begin{cases} n_0 & x < x_0 \\ n_1 & x_0 < x < x_1 \\ n_2 & x_1 < x < x_2 \\ & \vdots \\ n_j & x_{j-1} < x < x_j \\ n_e & x_j < x \end{cases} \tag{3.7}$$

Considering electromagnetic plane waves, the electric fields can be written as

$$E = E(x)e^{\mp ikz}e^{\pm i\omega t} \tag{3.8}$$

where the propagation is in the XZ plane and k is the the propagation wave vector. Thus, the solutions for the electric field distribution in the m-th layer will be represented by plane waves travelling to the right (incoming waves) and to the left (outcoming waves),

$$E_m(x) = (A_m e^{-ik_{mx}(x-x_m)} + B_m e^{ik_{mx}(x-x_m)}) \tag{3.9}$$

where A_m represent the amplitude of the incoming wave and B_m that of the outcoming wave at the interface $x = x_m$, c is the speed of the light, $k_{mx} = \omega n_m cos(\theta_m)/c$ is the x component of the wave vector, ω is the angular frequency and θ_m is the ray angle in the m-th layer.

Using a matrix notation and imposing the continuity conditions at the interfaces, the amplitudes at the interfaces can be related by

$$\begin{bmatrix} A_{m-1} \\ B_{m-1} \end{bmatrix} = D_{m-1}^{-1} D_m \begin{bmatrix} A_m \\ B_m \end{bmatrix} \tag{3.10}$$

where the matrix D is called the dynamical matrix, and can be expressed as

$$D_m = \begin{cases} \begin{bmatrix} 1 & 1 \\ n_m cos(\theta_m) & -n_m cos(\theta_m) \end{bmatrix} & TE\ polarization \\ \\ \begin{bmatrix} cos(\theta_m) & cos(\theta_m) \\ n_m & -n_m \end{bmatrix} & TM\ polarization \end{cases} \tag{3.11}$$

The matrix which describes the propagation wave in the incoming and outcoming directions with in the $m-$th layer is

$$P_m = \begin{bmatrix} e^{ik_{mx}L_m} & \\ 0 & e^{-ik_{mx}L_m} \end{bmatrix} \tag{3.12}$$

where L_m is the thickness of the m-th layer. Combining the eq. (3.12) with eq. (3.10) a expression for the so-called transfer matrix for the m-th layer is obtained

$$M_m = D_m^{-1} P_m D_m \tag{3.13}$$

and thereby, the transfer matrix for the whole multilayer system will be given by

$$M = \prod_{m=1}^{j} M_m = \begin{bmatrix} M_{11} & M_{12} \\ M_{21} & M_{22} \end{bmatrix} \tag{3.14}$$

The matrix expressed in eq. (3.14) permits to relate the electric field amplitudes in the incident medium with those in the emergent medium,

$$\begin{bmatrix} A_0 \\ B_0 \end{bmatrix} = \begin{bmatrix} M_{11} & M_{12} \\ M_{21} & M_{22} \end{bmatrix} \begin{bmatrix} A_e \\ B_e \end{bmatrix} \tag{3.15}$$

.

In the design of our structure (figure 3.2), we considered that the incident radiation comes from the left to the right, that is from the medium with refractive index n_0 to the one with refractive index n_e. The coefficients of reflection and transmission are defined as

$$r = \left(\frac{B_0}{A_0}\right)_{B_e=0} = \left(\frac{M_{21}}{M_{11}}\right) \tag{3.16}$$

$$t = \left(\frac{A_j}{A_0}\right)_{B_e=0} = \left(\frac{1}{M_{11}}\right) \tag{3.17}$$

The reflectance and transmittance are defined as

$$R = \left|r^2\right| = \left|\frac{M_{21}}{M_{11}}\right|^2 \tag{3.18}$$

$$T = \frac{n_e cos(\theta_e)}{n_0 cos(\theta_0)} \left|t^2\right| = \frac{n_e cos(\theta_e)}{n_0 cos(\theta_0)} \left|\frac{1}{M_{11}}\right|^2 \tag{3.19}$$

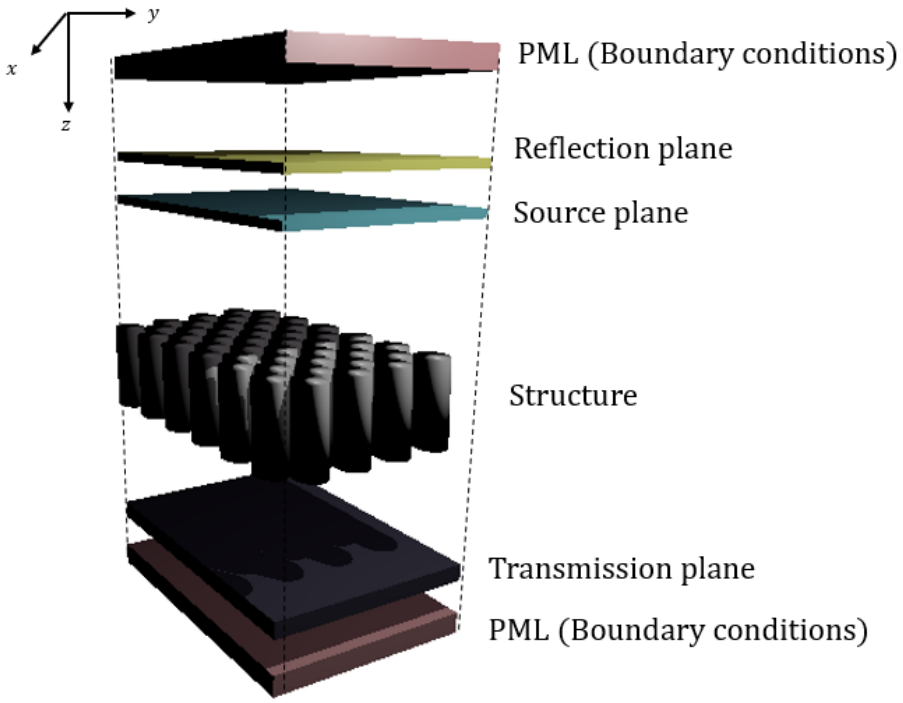

Fig. 3.3 Schematic concept view of the FDTD computational domain. The picture shows the perfect matched layers (PML) boundary conditions, the reflection and the transmission plane, the source plane and the structure.

3.3 Finite Differences in the Time Domain Method

The transfer matrix method is a simple and powerful method to calculate the reflectance and transmittance of a stack of thin films layers. However, with TMM it was not possible to investigate the optical properties of the NAA when all its subwavelength features need to be considered. Neither is it appropriate when the optical properties are influenced by aspects such as plasmonic and diffraction effects.

The Finite Differences in the Time Domain method (FDTD) is a numerical method characterized by the accuracy and rigour in order to model the optical properties (such as reflectance and transmittance) of structures taking into the account its subwavelength features. FDTD is generally computationally intensive, requiring a large amount of memory and computation time for some problems. The figure 3.3 illustrates a schematic concept of the FDTD computational domain.

In 1966, Yee [Yee1966] demonstrated how to obtain the Maxwell's equations solutions numerically for a boundary condition for a perfect conductor. Posterior works, such as Taflove et al. [Taflove1975] and Taflove [Taflove1980] promoted this method.

3.3.1 The Yee procedure for a finite differences system equations equivalent to Maxwell's

The numerical procedure consisted to introduce a set of finite differences for the differential equations which can be solved evaluating the fields components at appropriate chosen points. This mathematical procedure involved a discretization of the space into computational spatial cubes forming a 3D lattice in which each cube (Yee's cube) is the unit cell of the lattice.

To describe the Yee procedure we will follow that reported in [Yee1966] and [Taflove1975]. The Maxwell's equations (3.20 - 3.23) for a isotropic medium are the starting point:

$$\vec{D} = \varepsilon \vec{E} \tag{3.20}$$

$$\vec{B} = \mu \vec{H} \tag{3.21}$$

$$\nabla \times \vec{E} = -\frac{\partial \vec{B}}{\partial t} \tag{3.22}$$

$$\nabla \times \vec{H} = \frac{\partial \vec{D}}{\partial t} + \vec{J} \tag{3.23}$$

where ε is the permittivity and μ the permeability of the medium. Considering a three-dimensional Cartesian coordinate system and expanding the eqs. (3.22) and (3.23), a system of 6 scalar equations is obtained

$$\frac{\partial E_z}{\partial y} - \frac{\partial E_y}{\partial z} = -\frac{\partial B_x}{\partial t} \tag{3.24a}$$

$$\frac{\partial E_x}{\partial z} - \frac{\partial E_z}{\partial x} = -\frac{\partial B_y}{\partial t} \tag{3.24b}$$

$$\frac{\partial E_x}{\partial y} - \frac{\partial E_y}{\partial x} = -\frac{\partial B_z}{\partial t} \tag{3.24c}$$

$$\frac{\partial H_z}{\partial y} - \frac{\partial H_y}{\partial z} = \frac{\partial D_x}{\partial t} + J_x \tag{3.24d}$$

$$\frac{\partial H_x}{\partial z} - \frac{\partial H_z}{\partial x} = \frac{\partial D_y}{\partial t} + J_y \tag{3.24e}$$

$$\frac{\partial H_y}{\partial x} - \frac{\partial H_x}{\partial y} = \frac{\partial D_z}{\partial t} + J_z. \tag{3.24f}$$

Using the same notation that Yee in [Yee1966], a point and any function of the space and time in the spatial grid can be designated as

$$(i, j, k) = (i\Delta x, j\Delta y, k\Delta z) \tag{3.25}$$

and

$$F^n(i, j, k) = F(i\Delta x, j\Delta y, k\Delta z, n\Delta t) \tag{3.26}$$

respectively, being $\Delta x = \Delta y = \Delta z$ the space increment and Δt the time increment. Next, using the central difference approximation

$$\left.\frac{df(x)}{dx}\right|_{x=x_0} = \frac{f(x_0 + \Delta x/2) - f(x_0 - \Delta x/2)}{\Delta x}, \tag{3.27}$$

the function F can be approximate such as reported by Taflove et al. in [[Taflove1975]]

$$\frac{\partial F^n(i, j, k)}{\partial x} = \frac{F^n(i + 1/2, j, k) - F^n(i - 1/2, j, k)}{\Delta x} \tag{3.28}$$

$$\frac{\partial F^n(i, j, k)}{\partial t} = \frac{F^{n+1/2}(i, j, k) - F^{n-1/2}(i, j, k)}{\Delta t}, \tag{3.29}$$

considering Δx sufficiently small to neglect all the higher order terms in the approximation.

The approximation of F can be employed with $\vec{E}$ and $\vec{H}$ to replace the derivatives in (3.24a - 3.24f) with finite differences. To do this, the fields components are evaluated in the unit cell of the Yee cube [Yee1966] as illustrated in figure 3.4. At the same time, the components of $\vec{E}$ and $\vec{H}$ are evaluated at alternate half-time steps. This distribution of the points at which E and H fields are evaluated is key to the method, as every point at which E is evaluated is surrounded by six points at which H is evaluated in the previous half-time step, two in each direction of space. That leads the equation system (3.24a - 3.24f) into a discrete finite difference system

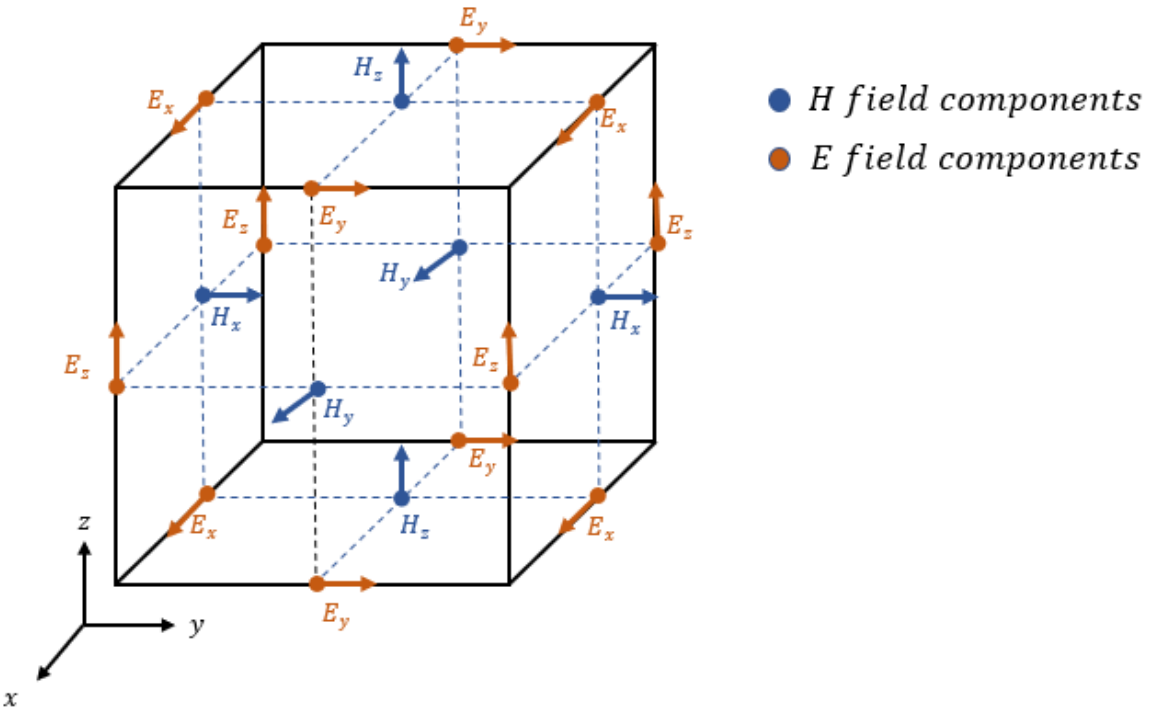

Fig. 3.4 Schematic view of the 3D Yee cell. The picture shows the positions of components of the $\vec{E}$ and $\vec{H}$. The components of $\vec{E}$ (orange arrows) are positioned in the middle of the edges whereas the components of the $\vec{H}$ (blue arrows) are placed in the centre of each face. The arrows indicate the directions of each field component.

$$\frac{E_z^n(i,j+1,k+1/2)-E_z^n(i,j,k+1/2)}{\Delta y}-\frac{E_y^n(i,j+1/2,k+1)-E_y^n(i,j+1/2,k)}{\Delta z}=\frac{B_x^{n+1/2}(i,j+1/2,k+1/2)-B_x^{n-1/2}(i,j+1/2,k+1/2)}{\Delta t} \tag{3.30a}$$

$$\frac{E_x^n(i+1/2,j,k+1)-E_x^n(i+1/2,j,k)}{\Delta z}-\frac{E_z^n(i+1,j,k+1/2)-E_z^n(i,j,k+1/2)}{\Delta x}=\frac{B_y^{n+1/2}(i+1/2,j,k+1/2)-B_y^{n-1/2}(i+1/2,j,k+1/2)}{\Delta t} \tag{3.30b}$$

$$\frac{E_x^n(i+1/2,j+1,k)-E_x^n(i+1/2,j,k)}{\Delta y}- \frac{E_y^n(i+1,j+1/2,k)-E_y^n(i,j+1/2,k)}{\Delta x}= \frac{B_z^{n+1/2}(i+1/2,j+1/2,k)-B_z^{n-1/2}(i+1/2,j+1/2,k)}{\Delta t} \tag{3.30c}$$

$$\frac{H_z^{n+1/2}(i+1/2,j+1/2,k)-H_z^{n-1/2}(i+1/2,j-1/2,k)}{\Delta y}- \frac{H_y^n(i+1/2,j,k+1/2)-H_y^n(i-1/2,j,k-1/2)}{\Delta x}= \frac{D_x^n(i+1/2,j,k)-D_x^{n-1}(i+1/2,j,k)}{\Delta t}+J_x^{n-1/2}(i+1/2,j,k) \tag{3.30d}$$

$$\frac{H_x^{n+1/2}(i,j+1/2,k+1/2)-H_x^{n-1/2}(i,j+1/2,k-1/2)}{\Delta z}- \frac{H_z^n(i+1/2,j+1/2,k)-H_z^n(i-1/2,j+1/2,k)}{\Delta x}= \frac{D_y^n(i,j+1/2,k)-D_y^{n-1}(i,j+1/2,k)}{\Delta t}+J_y^{n-1/2}(i,j+1/2,k) \tag{3.30e}$$

$$\frac{H_y^{n+1/2}(i+1/2,j,k+1/2)-H_y^{n-1/2}(i-1/2,j,k+1/2)}{\Delta x}- \frac{H_x^n(i,j+1/2,k+1/2)-H_x^n(i,j-1/2,k+1/2)}{\Delta y}= \frac{D_z^n(i,j,k+1/2)-D_z^{n-1}(i,j,k+1/2)}{\Delta t}+J_z^{n-1/2}(i,j+,k+1/2), \tag{3.30f}$$

in which the current value components of $\vec{E}$ depends only of the previous values of $\vec{H}$ and vice versa.

3.3.2 The stability criterion

In order to ensure the stability and the accuracy of the method, it is required that the electromagnetic field does not must change significantly under a increment of the space grid. Taflove et al. in [Taflove1975] reported that

$$\Delta x = \Delta y = \Delta z \tag{3.31}$$

must be a fraction of the minimum wavelength or the minimum dimensions of the scatterer. The authors reported that the condition to guarantee the stability of the mathematical procedure is

$$v_{max}\Delta t = \frac{1}{\sqrt{\frac{1}{(\Delta x^2)} + \frac{1}{(\Delta y^2)} + \frac{1}{(\Delta z^2)}}} \tag{3.32}$$

where the v_{max} is the maximum wave phase velocity

3.3.3 The boundary conditions

In order to avoid numerical contributions of the boundaries of the computational domain that reverberate in unwanted reflections, appropriate boundary conditions (BC) must be applied. Several BC can be implemented in FDTD, but for the study on the reflectance and transmittance in NAA we focused in absorbing and periodic BC.

Absorbing boundary conditions (ABC) :

The most commonly ABC used is the perfectly matched layer (PML) developed by Berenger in [Berenger1996]. The technique is based in the employment of a layer designed to absorb the electromagnetic waves and avoid the numerical reflections of these from the interfaces that delimits the FDTD unit cell.

In this thesis we have used a commercial-grade FDTD-based simulator [Lumerical]. The software permits users directly choose the necessary parameters that control the PML absorption properties, even choose between predefined profiles.

Periodic boundary conditions (BC) :

Periodic BC are simple and enable for modelling when periodic structures such as NAA are considered. Additionally, the software we used [Lumerical] has further BC implemented. One of them is that the program called Bloch BC, which can be applied if the structure is periodic but a phase shift appears in the fields between each period. Another one is the symmetrical/anti-symmetrical BC, which can be used when the problem under consideration has one or more planes of symmetry.

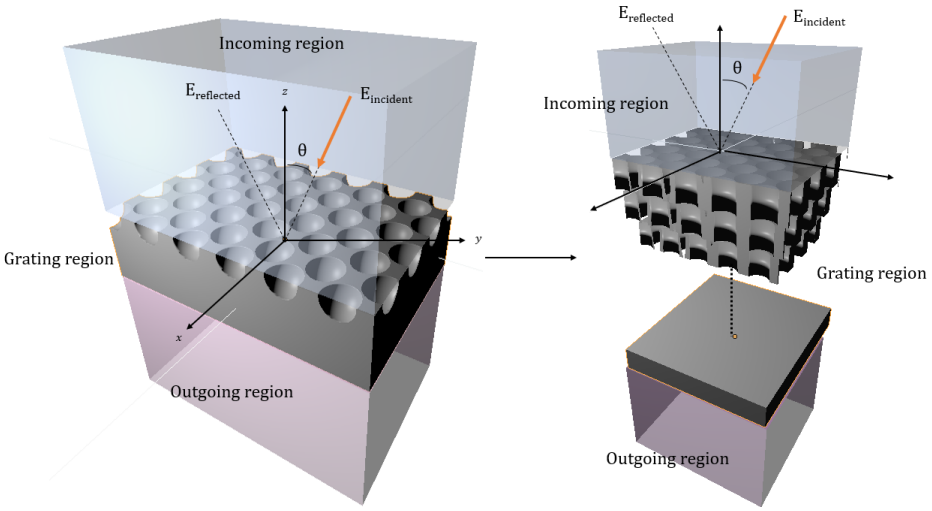

Fig. 3.5 Schematic concept view of the RCWA computational domain. The picture shows the regions within the domain: a incoming region, a grating region and a outgoing region. In the grating region, the periodic structure is decomposed in a system of multiple layers that are uniform in the Z direction.

3.4 Other numerical methods

3.4.1 The rigorous coupled wave analysis

In the study of periodic optical structures such as NAA, the rigorous coupled wave analysis (RCWA) [Moharam1995] is one of the most widely numerical method employed.

RCWA is a semi-analytical frequency-based numerical method that permits the simulation of the optical properties of, for example, periodic structures. This method considers three regions in its computational model: the incoming region, the grating or nanostructured region and the outgoing region [Mirotznik2010]. Figure 3.5 can illustrate a geometrical conception of the RCWA modelling. The incoming region is the system region formed by a superstrate. Generally is assumed that corresponds to an infinite half-spaced dielectric media index with a lossless refractive index $n_{incident}$. The grating region may be formed by a periodic nanostructured medium. The periodic structure is decomposed in a system of multiple layers that are uniform in one direction (such as Z direction) of its computational domain. The outgoing region corresponds to the substrate, which can be assumed as another infinite half-spaced with a lossless refractive index $n_{outgoing}$.

Due to the periodicity of the structure, in order to calculate the field inside the grating, this is decomposed in terms of their Fourier series. This expansion transforms the Maxwell's partial differential equations into a system of ordinary differential

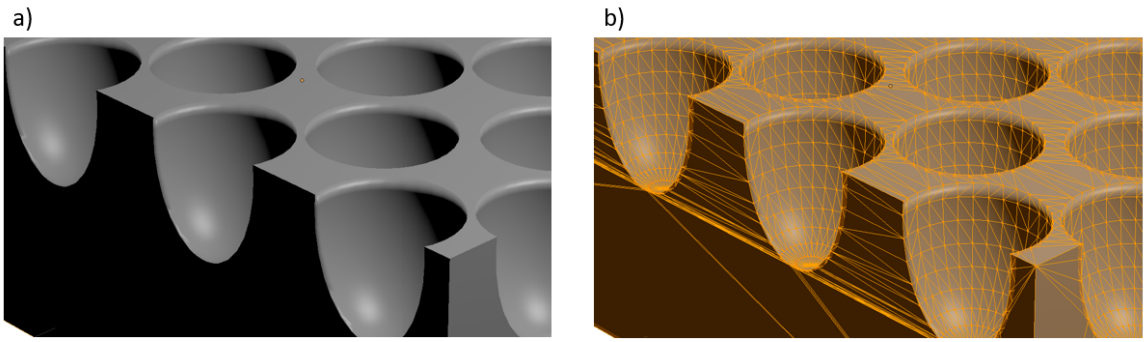

Fig. 3.6 Schematic concept view of the FEM meshing. The picture shows a diagram of (a) a NAA structure and (b) the corresponding with triangular meshing.

equations which can be solved as a eigen-value problem. The boundary conditions of continuity of the tangential components of $\vec{E}$ and $\vec{H}$ at the interfaces are employed to obtain a system of linear equations. Thus, truncating this system of equations the amplitudes of the propagating fields can be calculated with a specified level of accuracy.

3.4.2 The finite element method

The finite element method (FEM) is a frequency-based optical method that gives approximate values of the $\vec{E}$ and $\vec{H}$ at a set of discrete points in the computational domain. The numerical method is characterized by divide a larger problem into a set smaller ones called finite elements. FEM uses a meshing procedure to discretize the domain using small entities with a well-known shape such as triangular polygons. Then, these elements are modelled with set of equations which can be solved separately for tiny simulations or iteratively assembled in a bigger system of equations that model the entire problem [Han2014]. Therefore, the meshing plays a determinant role on the accuracy of the FEM model. Figure 3.6 illustrates a schematic computer view of a NAA triangular meshing.

In contrast with other methods, such as the TMM or the RCWA methods, the FEM method works in the real space handling finite real systems. Just to cite an example, Andonegui et al. [Andonegui2013] studied the transmissions coefficients, the band structures and the quality factors of several two-dimensional photonic crystals employing the finite element method. The authors also made an assessment of the FEM method comparing its results with those achieved using the plane wave expansion and the FDTD methods.

UNIVERSITAT ROVIRA I VIRGILI
NUMERICAL MODELLING OF NANOPOROUS ANODIC ALUMINA PHOTONIC STRUCTURES FOR OPTICAL BIOSENSING
Francisco Bertó Roselló

Chapter 4

Analysis and modelling of the optical behaviour of the NAA

The capacity to predict the optical behaviour of NAA is critical in order to design and develop future applications based on this material. In this process, it is crucial to have a solid theoretical framework that permits to establish the foundations for the analysis of the optical behaviour and the performance of the future devices. In this respect, the FDTD method for mathematical modelling described in the Chapter 3 provides the adequate method for the optical modelling of NAA structures.

In this chapter, an assessment on the capabilities of the FTDT method as a scheme for the numerical modelling of the optical properties of the NAA structures is presented. To this end, a geometric modelling procedure was described and evaluated by applying the EMA-TMM and the FDTD numerical methods on two types of NAA structures with different structural parameters. Finally, the optical response of each NAA structure considered was analysed.

4.1 Introduction

Investigations in research areas such as biotechnology [Macias2013, Baranowska2014, Santos2013a], energy [Aryal2008, Huang2008] and medical science [Kumeria2012a, Gultepe2010, Losic2009, Anglin2008] are some examples where the NAA has shown its increasing relevance. A particularly important aspect of such nanomaterial is the study of their optical properties. These are decisive in the development of devices or applications based on the behaviour of the light interaction on NAA structures, as for example in optical biosensing or in photovoltaic energy conver-

sion [Alvarez2009, Anglin2004, Balderrama2015, Santos2014, Ferre-Borrull2015]. The suitability of NAA for being used in optical biosensing lies in their optical properties in the visible range [Kumeria2014, Kumeria2012], their chemical and biochemical stability and compatibility [Kumeria2014a] and the high tunability of their structural parameters [Lee2006a, Ferre-Borrull2014]. Additionally, the NAA provides a structure that facilitates an important requirement: a selective identification of the analytes [Lin1997]. The NAA structures present a high surface area in relation with their volumetric size and their pores can act like containers or holders of physical objects like analytes. These features confer NAA the possibility to study the analyte binding process not only in a planar way but also in depth. The combination of all of these properties with a high sensitivity and selectivity [Gyurcsanyi2008] makes the NAA a good candidate to be used as a platform material, especially when compared with planar geometries.

On the other hand, another significant aspect in optical biosensing must be considered: a transduction mechanism [Lin1997]. That is, the biosensor must have a system thereby the detection of the analytes results in a measurable and quantifiable optical signal. There are some sensing approaches currently being adopted in research for this purpose. Several of them were reported by Kumeria et al. where the authors classify in detail different detection methods, both optical and physical [Kumeria2014a]. Taken together, these features make NAA structures particularly appropriate as a platform for optical biosensing.

Having introduced the suitability of the NAA for optical biosensing and having established their optical properties as a key point, we will now move on to discuss the different considerations to take into account in order to perform the numerical modelling. As was explained in Chapter 2, the optical properties of the NAA are very sensitive to the anodization conditions. Specifically, the acid electrolytes commonly used in the fabrication process strongly influence the NAA structural parameters [Kumeria2014a] and the chemical composition of the constituents materials. Therefore, the different geometrical and chemical characteristics have to be considered for the optical modelling of NAA. With regard to the geometrical characteristics, the main structural parameters of NAA (the interpore distance (d_{int}), the pore diameter (d_p), the barrier layer thickness (t_b), the pore length (L)) have to be included in order to model the optical properties. In addition to these geometrical parameters, further structural features must be considered in the numerical modelling. These are the corresponding to the interfaces texturization occurred during the alumina growth process, when a hemispherical concavity pattern of the interfaces is conferred. Concerning the chemical

characteristics of the NAA structure and in addition to the optical constants of the different material constituents, it is clear that anionic species have migrate from the acidic electrolyte to the NAA modifying the chemical composition of the alumina. This modification does not only affect to the chemical composition but also the spatial distribution of the optical properties of the NAA. Several authors reported that the NAA structures display an onion-like layered structure in the chemical composition of the pore wall oxide, being the layer closest to the pore the one with the highest anion concentration. However, the number of layers that forms the pore wall is different for distinct investigations: some authors [Santos2014a] reported that the number of layers is four, whereas others [Thompson1997] reported only a dual layer structure in the pore wall for the distribution chemical composition.

Let us now to consider the numerical methods employed to predict the optical behaviour of the NAA. As we said previously at the beginning of this chapter and detailed in chapter 3, the TMM is a numerical method widely used not only for modelling the optical behaviour of thin films [M.Born1999] but also photonic crystals [Joannopoulos2011, Whittaker1999] for instance. In order to model the NAA structure with TMM, the refractive index of the porous alumina must be obtained. To achieve this, we can employ an effective medium approximation (EMA), for instance such as of Bruggeman or Maxwell-Garnett [Bosch2000, Bosch2001], and obtain an effective refractive index corresponding to the porous alumina. However, when modelling the NAA produced with some acidic electrolytes (phosphoric acid electrolyte, for instance) the consequent patterning in the substrate and the top of the structure results in non-flat interfaces. Besides, the dimensions of some structural parameters, like the pore diameter and the interpore distance, reach values between 400 nm and 500 nm, being in the order of the wavelength of the incident light for applications working in the visible. As a consequence, although EMA-TMM can be used in many cases, it is clear that EMA is not a suitable option for all the range of the NAA structural parameters and, therefore, other numerical modelling methods have to be employed. From the different existing methods, described in the previous chapter, the ability to deal with complex structures and the accuracy makes the FDTD method the chosen for our purpose. Our objective is to evaluate the capabilities of FDTD as a framework for the numerical modelling of the optical properties of NAA when all the features described above are considered. Furthermore, we also establish the conditions in which EMA-TMM is adequate for the simulation of NAA by comparing its results to FDTD and to experimental measurements.

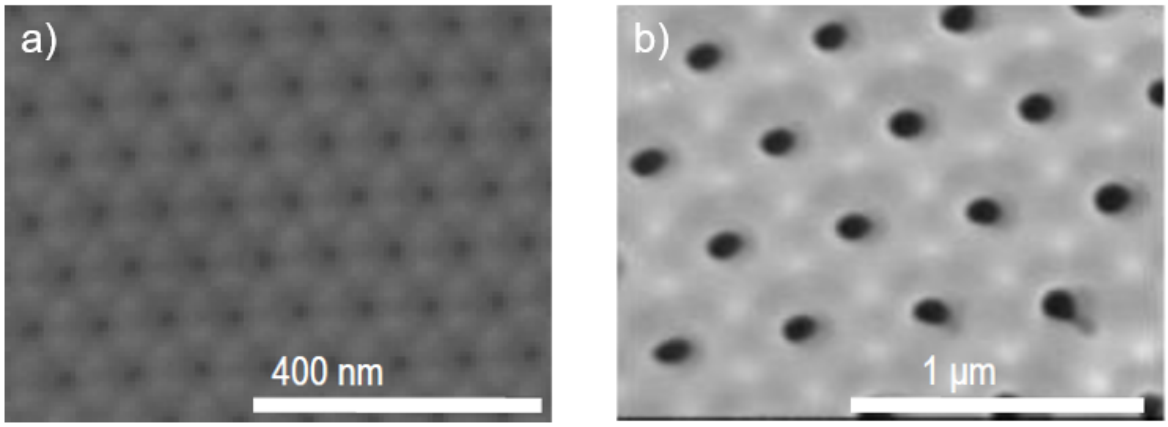

Fig. 4.1 SEM images of the NAA structures. (a) Top view SEM image for short interpore distance NAA. (b) Top view SEM image for long interpore distance NAA. Adapted from [Berto-Rosello2016].

In this sense and to assess the accuracy of the method, two types of NAA samples with distinct structural parameters were prepared. The first type was produced with oxalic acid electrolyte obtaining NAA structures with short interpore distances, whereas in the second type, the NAA structures obtained have long interpore distances and were produced with phosphoric acid electrolyte. Reflectance spectra of these samples were measured. Subsequently, in order to provide comparison, reflectance spectra of these real samples simulations were performed with different numerical methods.

4.2 Fabrication and characterization of the NAA samples

The two-step anodization process [Masuda1995, Masuda1997] described in Chapter 2 was used to produce the NAA samples. We obtained two types of NAA samples distinguished by different structural parameters. Figure 4.1 shows top view SEM images of two of the samples. The first sample is produced with oxalic acid (0.3M, 40V, 5ºC) as the electrolyte acid (figure 4.1.a). From the corresponding SEM image, the main structural parameters for the samples obtained with this electrolyte were estimated: interpore distance, d_{int} = 100 nm, pore diameter, d_p = 21.5 nm, and pore length (or equivalently, porous layer thickness), L= 1200 nm. The second sample is obtained using phosphoric acid (1% wt. with ethanol, 195V, -5ºC) as the electrolyte (figure 4.1.b). In this case, the structural parameters characterizing the sample also are estimated: d_{int} = 440 nm, d_p=125 nm and L = 2400 nm. In these structures the

Table 4.1 Porosity and alumina thickness for the different NAA samples

Parameter	interpore distance	
	d_{int}= 100 nm	d_{int}= 440 nm
Porosity (%)	4.19	7.31
Alumina thickness (nm)	1200	2400

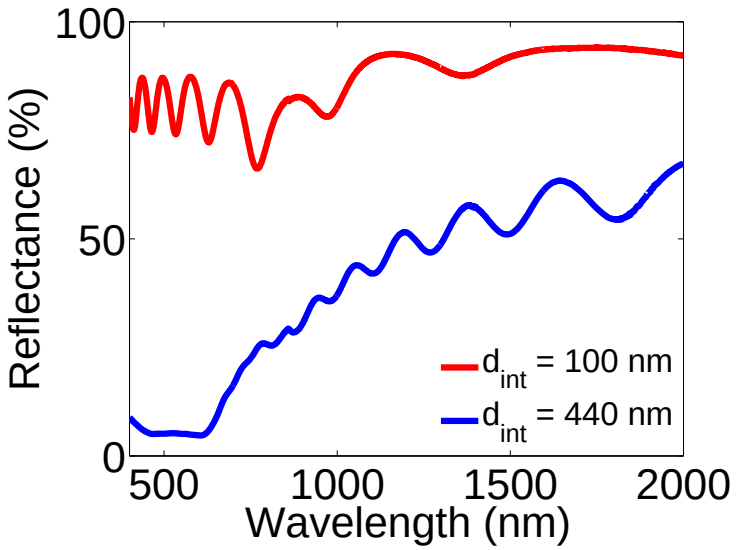

Fig. 4.2 Measured reflectance spectra of NAA samples. Measured reflectance spectra of NAA samples with $d_{int} = 100$ nm (produced with oxalic acid electrolyte), and $d_{int} = 440$ nm (produced with phosphoric acid electrolyte). Adapted from [Berto-Rosello2016].

porosity depends of d_{int} and d_p (eq. 2.2), and the aluminium substrate is preserved in all the samples. The Table 4.1 summarizes the porosity and the thickness of the porous alumina layer being of 4.19% and 1200 nm respectively for short-interpore distance NAA, and 7.31% and 2400 nm respectively for long-interpore distance NAA.

In order to characterize the samples, spectroscopic reflectance measurements were carried out. To this end, a Lambda 950 spectrophotometer from PerkinElmer (Whaltham, MA, USA) equipped with a tungsten lamp as the light source and using a Universal Reflectance Attachment is used. The incidence angle is set very close to the normal incidence (6º) and the wavelength range was set from 400 nm to 2000 nm.

One of the obtained reflectance spectra is shown in figure 4.2. Here, both spectra are illustrated: the solid red line corresponds to the sample with $d_{int} = 100$ nm, that is, the sample with short interpore distances, whereas the blue solid line corresponds to the sample with $d_{int} = 440$ nm equivalent to long interpore distances. In both cases

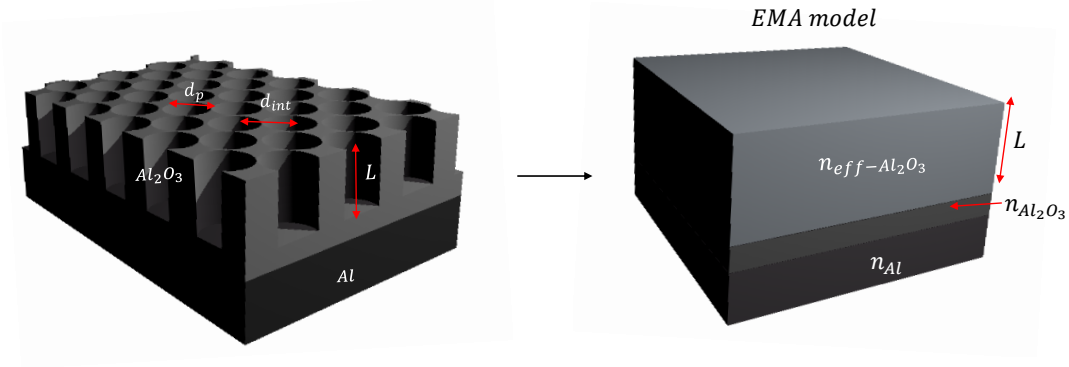

Fig. 4.3 Schematic view of the EMA model where each compound layer has their effective refractive index. The model consists of a three layered system formed by a substrate layer with refractive index $n_{aluminium}$ corresponding to the refractive index of aluminium, a thin barrier layer with refractive index $n_{alumina}$ corresponding to the non-porous alumina and a top layer with effective refractive index $n_{eff-alumina-air}$ corresponding to the porous alumina.

we observe an oscillating behaviour due to the Fabry-Pérot interferences in the NAA thin film. However, the picture shows a significant reduction of the reflectance in the visible range for long interpore distances.

4.3 Design and numerical modelling

4.3.1 Effective medium approximation with TMM and limitations to the approach.

As we have exposed in Chapter 3, in the case of thin film modelling with EMA, flat interfaces and layers of homogeneous materials are considered. The EMA permits in combination with TMM to obtain the effective refractive index of such layers when one of the materials in the structure is actually a mixture of materials [D.A.G.Bruggeman]. The EMA simulations were designed by considering the structure as a multi-layer system, where each compound layer has their effective refractive index. The figure 4.3 shows a schematic view of the EMA model and how the resulting effective system is formed. This picture shows a final system composed of a substrate and two thin film layers. One layer is a thin barrier layer with refractive index, $n_{alumina}$, corresponding to the non-porous alumina, whereas the another one is a top layer considered as an amalgamation of air and

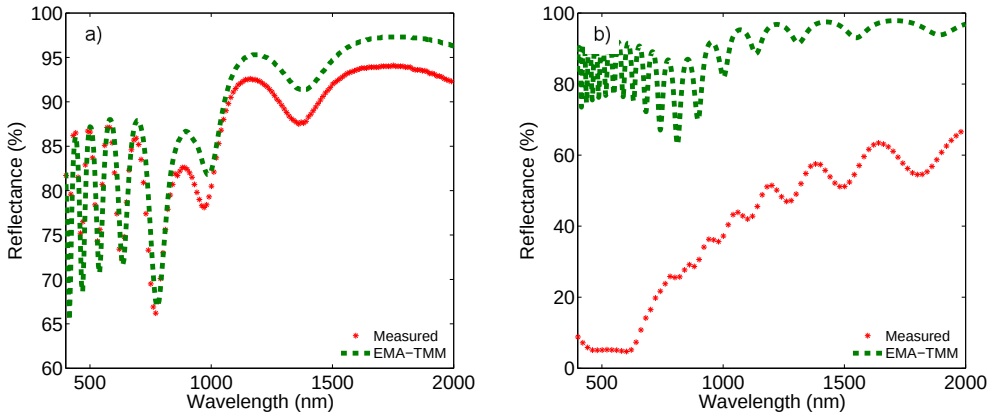

Fig. 4.4 Plot of the measured and the calculated reflectance spectrum using EMA model with TMM. a) d_{int}= 100 nm and b) d_{int} = 440 nm. The red dots represent the measured reflectance spectra and the green dashed line the EMA-TMM result for the flat interfaces model. Adapted from [Berto-Rosello2016].

the alumina matrix with effective refractive index, $n_{eff-alumina-air}$, corresponding to the alumina porous layer. The substrate has a refractive index, $n_{aluminium}$, corresponding to the refractive index of aluminium. The EMA provides the effective refractive index of the porous layer as a mixture of the refractive indices of the air that fills the pores and the refractive index of the alumina. This effective refractive index of the porous alumina can be calculated by means of the Bruggeman's formula, considering the refractive index of the non-porous alumina from ref. [Palik2012].

The reflectance calculations are performed with TMM as a computational tool, and the obtained results are shown in figure 4.4. Figure 4.4 shows a comparison between the reflectance spectrum calculated using the EMA-TMM approximation and the measured reflectance spectrum. Figure 4.4.a corresponds to NAA with an interpore distance of d_{int} = 100 nm (short interpore distance) while Figure 4.4.b corresponds to an interpore distance of d_{int} = 440 nm (long interpore distance). The oscillating behaviour of the measured spectra observed are due to the Fabry-Pérot interferences in the alumina thin film. However, for long interpore distances NAA a strong reduction of the measured reflectance is observed in the visible range. The EMA-TMM simulation method is able to reproduce the aforementioned oscillation behaviour but fails to predict the decrease in reflectance for long interpore distance. The possible source of the divergence between the measured and simulated reflectance spectra may lie in the suitability of applying EMA as a modelling tool. It should be noted that EMA considers that the distinct materials that build into the effective medium have characteristic structural parameters much smaller than the wavelength of the incident light. However, when the

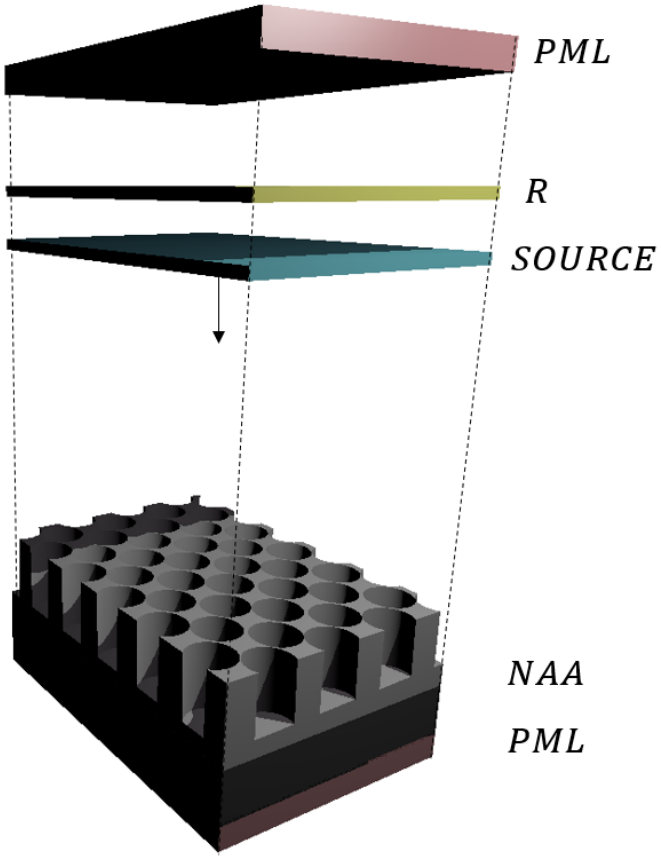

Fig. 4.5 Schematic view of the FDTD computational domain: R denotes the reflectance monitor, NAA denotes the structure, PML denotes de perfect matched layers and the source are explicitly indicated.

wavelength becomes of the order of the wavelength of the visible range, the previous statement is not satisfied being particularly noticeable for the long interpore distance NAA structures. It could be inferred therefore that EMA can be adequate to reproduce the measured reflectance spectrum for short interpore distance NAA which structural parameters in the order of the incident wavelength. Nevertheless, when the geometric parameters are of the order of the wavelength of the incident light, the EMA is no longer adequate and it is necessary to employ an alternative numerical method to deal with the geometrical features of a wide range of structures. The method we have chosen is FDTD because of its accuracy and ability to deal with complex structures.

4.3.2 FDTD modelling

In order to model with FDTD, we follow the modelling procedure established in the previous chapter, using a commercial-grade FDTD-based simulator [Lumerical].

First, the definition of the computational domain for the FDTD calculations must be established. Therefore, for each interpore distance considered, the computational domain used in the simulations (Figure 4.5) has dimensions of d_{int} nm in the X direction, $\sqrt{3}d_{int}$ nm in the Y direction and 14000 nm in the Z direction. The structure to simulate consists in a hexagonal array of cylindrical pores in an alumina matrix perpendicular to the surface, onto an aluminium substrate. The NAA structure was designed from a triangular unit cell in order to reproduce the hexagonal arrangement of pores and was placed in the centre of the computational domain. In the way that the domain was designed, the computational cost for this kind of simulations could be very intensive. Fortunately, the NAA platform exhibits a 2D-photonic crystal symmetry (Figure 4.6). Therefore, we took advantage of the symmetry of the structure in order to reduce the computational time. We applied periodic boundary conditions in the X and Y directions. The computational time was reduced in a 25% and the periodicity leading for an infinite structure in these directions was preserved. For the Z direction the situation was quite different. Computationally, the interacting light with the boundaries of the computational domain in this direction can introduce non-physical reflections with origin in the numerical procedures back again in the unit cell. Thus, we established perfectly matched layers (PML) as a boundary condition, which will absorb the light in this direction and avoid the unwanted reflections. Next, the optical constants of each material we used were defined. The software we used has their own material database (based in ref. [Palik2012]) for the complex refractive index of each compound. The optical source was plane wave incident on the alumina layer side with wavelengths in a range from 400 nm to 2000 nm. The direction of propagation was backwards in the Z direction and perpendicular to the structure (X-Y plane). Finally, a monitor (Figure 4.5) at the top of the NAA structure to collect the optical reflectance spectrum as a function of wavelength was included.

The refractive index distribution profile of the NAA structure depends, among others, on the geometrical parameters and also on the chemical properties of the NAA. Therefore, four distinct geometric models are taken into consideration in different FDTD simulations: i) a initial model that considers the aluminium-alumina interface flat, ii) a second model that considers the interface between the aluminium substrate and the alumina layer texturized with the hemispherical concavities, as well as the alumina barrier layer and the top surface of the alumina layer, iii) a third improved model that considerate a conformal anionic layer in the inner pore wall layer with distinct optical properties and iv) a last fourth model which contemplates absorption in

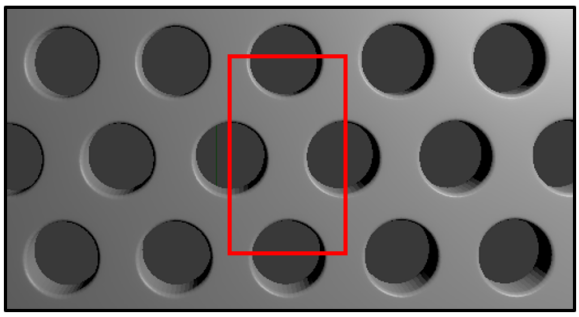

Fig. 4.6 Schematic planar view of the FDTD unit cell: the black circles denote the pores in a hexagonal arrangement, while the red square denotes the unit cell in the XY plane. Adapted from [Berto-Rosello2016].

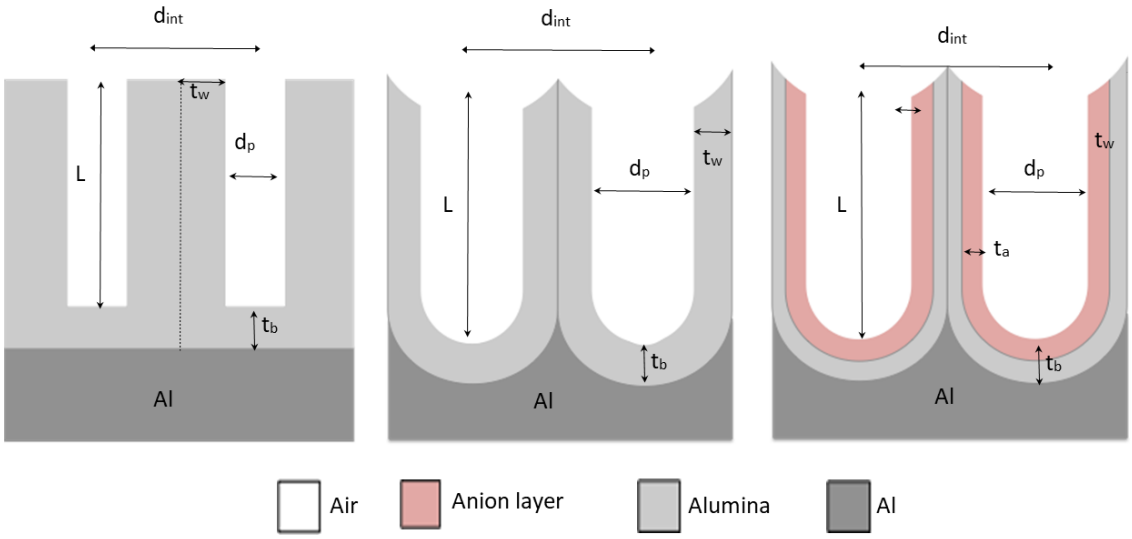

Fig. 4.7 Schematic draw of the different geometrical models. a) First model with flat interfaces between the aluminium substrate and the porous layer. b) Second model with the texturization of the interfaces with hemispherical concavities. c) Third and fourth models with the dual layer structure in the pore walls, without and with absorption, respectively. Adapted from [Berto-Rosello2016].

the anionic layer. Each model differs from the previous one in a increasing complexity of the geometry and of the refractive index distribution

Figure 4.7 represents a schematic draw of these models. The key parameters specified in the picture are d_{int} as the interpore distance, d_p as the pore diameter, t_w as the pore wall thickness, L as the pore length and t_b as the barrier layer thickness. Additionally, the Table 4.2 summarizes these values for each kind of NAA.

Table 4.2 Key parameters of the NAA for each interpore distance considered. Adapted from [Berto-Rosello2016].

Key Parameter	interpore distance	
	d_{int}= 100 nm	d_{int}= 440 nm
L(nm)	1200	2400
d_p (nm)	21.5	125
t_b (nm)	$0.5 \cdot d_{int}$	$0.5 \cdot d_{int}$

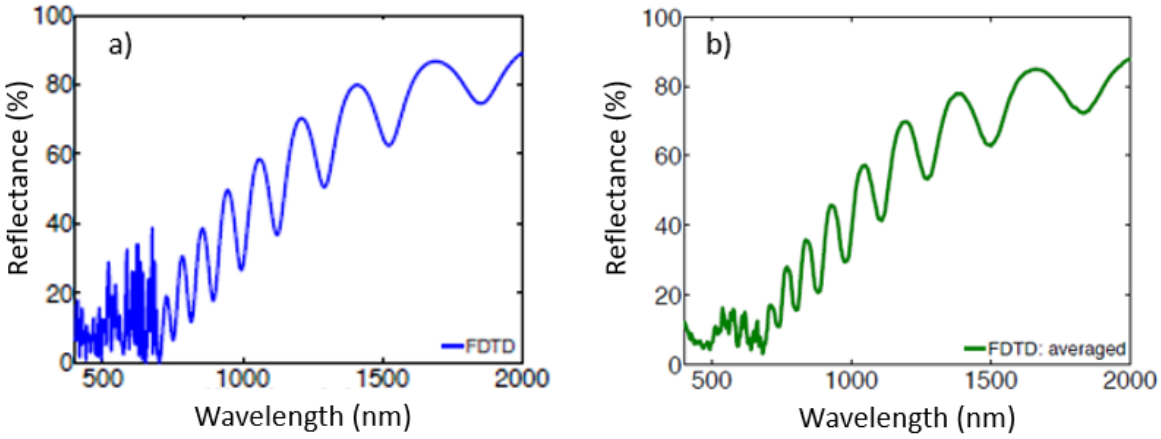

Fig. 4.8 Plot of the calculated reflectance spectrum and the averaged spectra using the procedure to take into account the non-periodicity of the pores in the FDTD simulations for NAA structures with long interpore distances. a) Calculated reflectance spectra showing the peaks associated with diffraction modes. b) Average of the calculated reflectance spectra.

Procedure to take into account the non-periodicity of the pores

These FDTD simulations are performed considering a NAA structure with an ideal hexagonal arrangement of the cylindrical pores and completely periodic. The optical reflectance spectra obtained in the simulation of NAA periodic structures, shows peaks associated with diffraction modes in the visible range (figure 4.8.a). These diffraction features are particularly relevant for NAA structures with their interpore distance in the order of the incident light wavelength. However, the measured spectra are absent of this kind of diffractive effects. The reason of these discrepancies lies in the fact that real NAA structures have a non-ideal pore ordering and their pore arrangement is broken into domains. Therefore, the disorder or the broken order of the NAA has to be contemplated although we considered perfectly ordered NAA structures when perform the simulations. Thus, we followed a procedure described in [Porta-i-Batalla2016] to

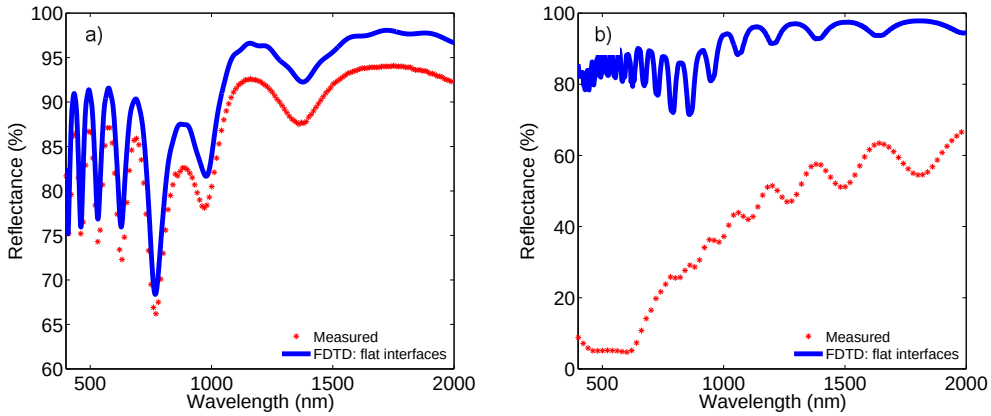

Fig. 4.9 Plot of the measured and the calculated reflectance spectrum using FDTD considering the flat interfaces. a) d_{int}= 100 nm and b) d_{int} = 440 nm. The red dots represent the measured reflectance spectra and the blue solid line the FDTD result for the flat interfaces model.

take into account the non-periodicity of the pores in the FDTD simulations for NAA structures with long interpore distances (figure 4.8.b).

Flat interfaces

The first model we considered consisted of a layer of NAA on a flat aluminium substrate (figure 4.7.a). Figure 4.9 shows a comparison between the reflectance spectrum calculated using the FDTD method considering flat interfaces and the measured reflectance spectrum. Figure 4.9.a corresponds to NAA with an interpore distance of d_{int} = 100 nm (short interpore distance) while Figure 4.9.b corresponds to an interpore distance of d_{int} = 440 nm (long interpore distance). In the same way that occurs with the EMA approach in the case of short interpore distances NAA, the oscillating behaviour of the measured spectrum can be also reproduced with FDTD with flat interfaces. However, in the case of long interpore distance NAA, the FDTD method leads to the same result as obtained with EMA-TMM, and does not reproduce the strong reductions of the reflectance observed in the range from the near-infrared to the visible range.

Figure 4.10 shows the simulated reflectance spectra with both methods (EMA-TMM and FDTD with flat interfaces) and the measured reflectance spectra, in order to establish a comparison. Figure 4.10.a corresponds to NAA with short interpore distance (d_{int} = 100 nm) while Figure 4.10.b corresponds to the long interpore distance (d_{int} = 440 nm). The reflectance scales of these two figures are adjusted to maximize visibility

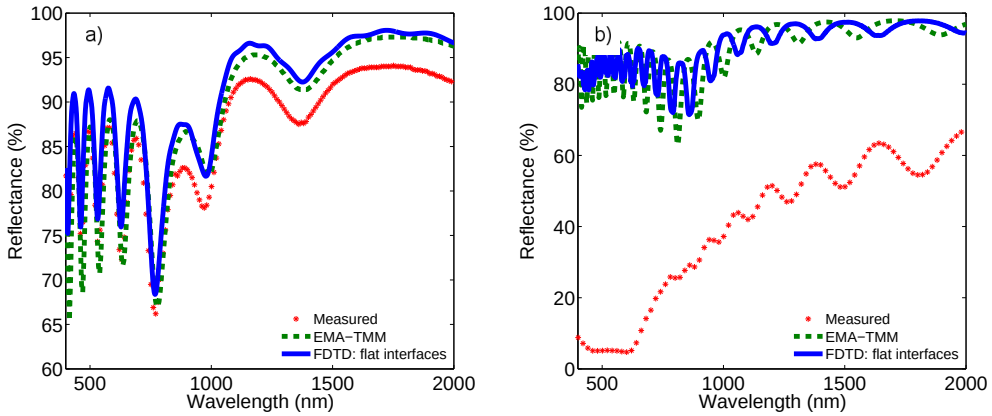

Fig. 4.10 Comparison of the measured and the calculated reflectance spectra by means of EMA and FDTD considering the flat interfaces. a) d_{int}= 100 nm and b) d_{int} = 440 nm. The red dots represent the measured reflectance spectra, the green dashed line the EMA result and the blue solid line the FDTD result for the flat interfaces model. Adapted from [Berto-Rosello2016].

of the results. As previously stated, both simulation methods are able to reproduce the oscillation behaviour but fail to predict the decrease in reflectance for long interpore distance. However, the structural parameters of the NAA with long interpore distances are in the order of the wavelength of the incident light. Furthermore, these results indicate that although the FDTD method is able to take into account naturally the different characteristic sizes of the NAA, the presumption of flat interfaces for long interpore distance in the visible region is not adequate.

Consequently, the geometric model must be improved in order to take into consideration the geometric features of the NAA, such as the hemispherical concavities placed in the substrate and in the top of the alumina layer.

Texturization of the interfaces

To incorporate the particular NAA nanostructuring to the investigation we consider the second model. This takes into account the texturization of the interface between the aluminium substrate and the alumina layer with hemispherical concavities. Additionally, it also considers the texturization of the alumina barrier layer and the top surface of the alumina layer. Figure 4.7.b shows a schematic cross section of this improved geometric model with a new pore morphology with texturized interfaces, maintaining the same structural parameters as those depicted in Figure 4.7.a.

Figure 4.11 shows the same measured spectra and the same calculated spectra with FDTD with flat interfaces as in Figure 4.10 as a reference to evaluate the influence of

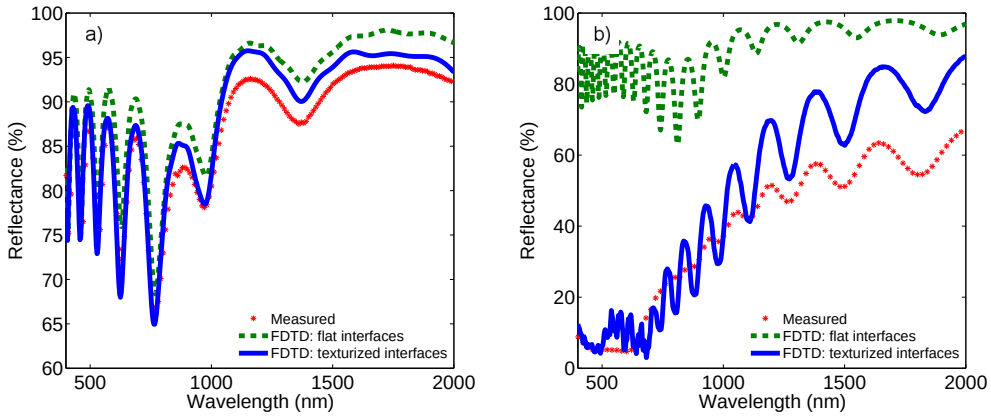

Fig. 4.11 Comparison of the measured and the calculated reflectance spectra by means of FDTD considering flat interfaces and the texturized interfaces. a) d_{int}= 100 nm and b) d_{int} = 440 nm. The red dots represent the measured reflectance spectra, the green dashed line the FDTD with flat interfaces result and the blue solid line the FDTD result for the texturized interfaces model. Adapted from [Berto-Rosello2016].

the texturization of the interfaces. Besides, in figure 4.11 is also depicted the result of FDTD when the texturized interfaces are considered. Concerning short interpore distances NAA (figure 4.11.a), both calculated spectra shows a good agreement with the measured spectrum, revealing a better adjustment in the case of FDTD with texturized interfaces. A closer analysis reveals a smaller difference between the reflectance spectra in the IR region, while in the visible region a better adjustment of the amplitude of the oscillations was achieved. Instead, major differences between in the simulated and measured reflectance spectra for long interpore distance NAA structures (figure 4.11.) are observed. The strong reduction of the reflectance in the visible range is replicated by FDTD. The explanation to this substantial reduction of the reflectance could lie in the scattering produced by the nanopatterning of the NAA with the interaction with the incident light. The characteristic dimensions of the long interpore NAA become similar the wavelength of light and therefore this scattering is more intense than for short interpore distance NAA. This result lead us to assume that for a convenient modelling of NAA structures in a broad range of interpore distances, it is crucial to incorporate into the model the texturization of the aluminium-alumina interface. Additionally, this result also suggests FDTD as the most suitable method for the simulations.

Although the ability of this model in the replication of the reflectance for a wide range of NAA structures has been proved, a more accurate adjustment of the oscillations remains pending. Until now the only considerations incorporated to the model are geometrical. As we have seen in Chapter 2 and in the introduction, the fabrication

Table 4.3 Widths and refractive indexes of the anionic layer for each kind of NAA. Adapted from [Berto-Rosello2016].

Key Parameter	interpore distance	
	d_{int}= 100 nm	d_{int}= 440 nm
t_a (nm)	$\frac{2}{3} \cdot d_{int}$	$\frac{2}{3} \cdot d_{int}$
$n_{anionic\ layer}$	1.67	1.67

conditions of the NAA influences the structural parameters as well as the chemical composition of the alumina. Therefore, we can evolve the pore morphology model into a new third model that takes into account, in a geometrical manner, chemical features of the structure.

Consideration of the existence of anionic species into the alumina in the geometric model

As we said in the introduction of this chapter, during the electrochemical process exists an incorporation of anions from the electrolyte acid to the NAA. This incorporation influences the chemical composition of the NAA and in consequence its optical properties. In order to incorporate these anionic species as a result of the electrolytic acid action, a third model is developed. This model is schematically depicted in Figure 4.7.c. Here, starting from the second model which considers the texturized interfaces, we take into account the anion addition by considering a double layer structure in the pore wall. The modelling is performed by considering such double layer structure in the computational domain. Figure 4.7.c shows a schematic picture of the texturized model with the consideration of the anionic layer in the pore wall, where t_a indicates its width. The first layer forms the inner pore wall without incorporated anions, and the second layer forms the outer pore wall (nearest to the pore and depicted in a different colour) with a higher anion concentration. This layer extends from the alumina-air interface within the pore up to about two thirds of the barrier layer [Thompson1997]. The refractive index of this anionic layer is different from the bulk alumina. The table 4.3 shows the widths and the refractive indexes of the anionic layer we considered.

Figure 4.12 shows the simulated spectra considering the existence of the anionic layer into the pore wall. As we did previously and to provide a reference, we included both the measured spectra and the simulated spectra depicted in Figure 4.11 and corresponding to the second model. In this way, it is easier to carry out an evaluation of the contribution to the spectra of each incremental step in model complexity. We

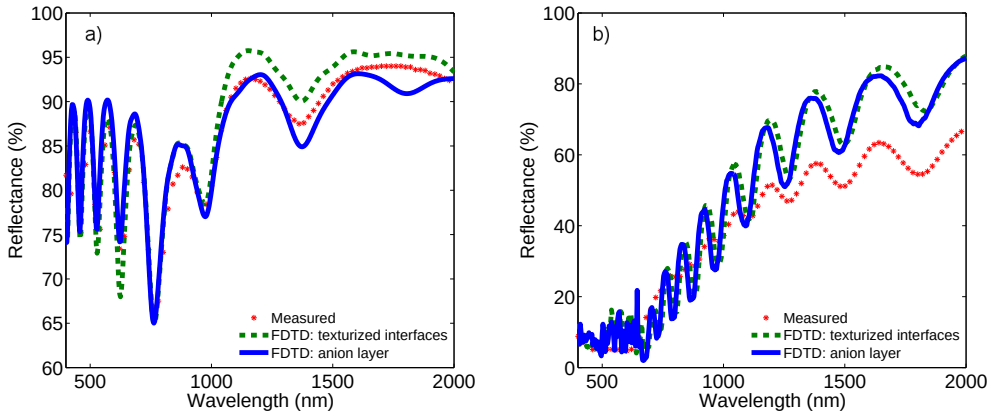

Fig. 4.12 Comparison of the measured and the calculated reflectance spectra by means of FDTD considering the texturized interfaces and the anionic layer model. a) d_{int}= 100 nm and b) d_{int} = 440 nm. The red dots represent the measured reflectance spectra, the green dashed line the FDTD result for the texturized interfaces model and the blue solid line the FDTD result for the anionic layer model. Adapted from [Berto-Rosello2016].

observe that the introduction of the anionic layer in the model contributes in a slight way to the a better adjustment of the calculated spectrum. The figure 4.12.a shows the simulated spectra related to the short interpore distance NAA. Analysing the graph, we observe that in the visible region the variation introduced when considering the anion-incorporated layer is quite small whereas in the infrared region the calculated reflectance is reduced. Next, we analyse the measured and calculated spectra corresponding to the long interpore distance NAA depicted in figure 4.12.b. When we focus in the infrared region, the reduction in the reflectance observed in Figure 4.12.a also is observed here. Besides, the amplitude of the oscillations also is reduced. Thus, these variations in the calculated reflectance spectra contributes to a slight adjustment with the measured spectrum. Therefore, we can make the statement that the inclusion of the anionic layer into the model enhances the simulation of the reflectance spectra of the NAA.

On the other hand, it is known from literature, as stated in chapter 2, that the phenomena of the absorption and emission of light of the NAA comes from the incorporated anionic species. The next aspect of the study is to consider how the incorporation of absorption in this anionic layer would affect the simulation of optical properties of the NAA.

Consideration of absorption in the anionic layer

In order to deal with the absorption in the anionic layer, we updated our third model by the addition of an absorptive term. Therefore, we developed a new model, the

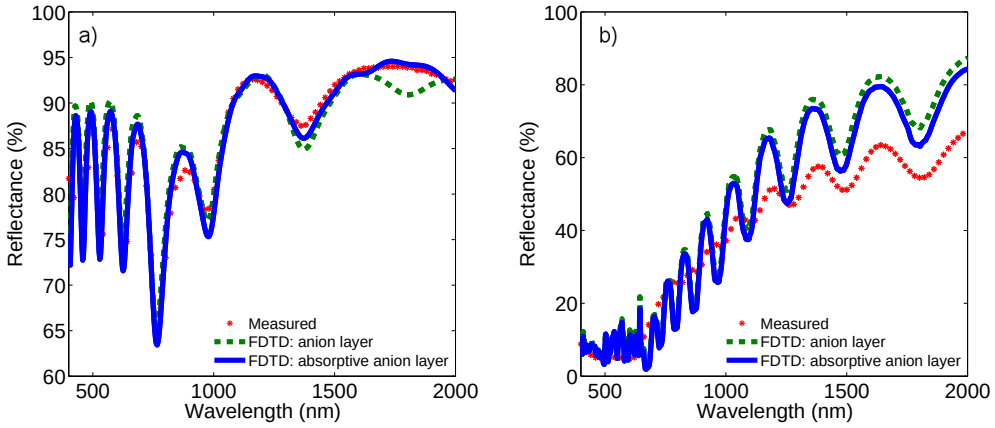

Fig. 4.13 Comparison of the measured and the calculated reflectance spectra by means of FDTD considering the anionic layer model, with and without absorption. a) d_{int}= 100 nm and b) d_{int} = 440 nm. The red dots represent the measured reflectance spectra, the green dashed line the FDTD result for the anion layer model without absorption and the blue solid line the FDTD result for the anionic layer model with absorption. Adapted from [Berto-Rosello2016].

fourth model, where the inclusion of this absorptive term in the anionic layer involves a change in each component of the complex refractive index of the affected region. Thus, we considered the same complex refractive index, $n_{absorptive\ anionic\ layer} = 1.67 + 0.002i$, for each kind of NAA. The results of the simulations for the model with the absorptive anionic layer are summarized in figure 4.13. The figure 4.13.a corresponds for the short interpore distances NAA whereas figure 4.13.b corresponds for the long interpore distances NAA. In both pictures we also included the measured reflectance and the simulated FDTD reflectance corresponding to the third model to use it as a reference. Figure 4.13.a shows that the amplitude of the oscillations in the simulated reflectance is slightly reduced when including an absorption in the anion-incorporated layer. If we focus now in the infrared region, the simulated spectrum with the absorptive anionic layer shows a better agreement with the measured spectrum in comparison with the corresponding without absorption. This agreement even wipes out a deviant oscillation present in the non-absorbing spectrum and absent in the measured spectrum. At this point we focus on the long interpore distances NAA. The figure 4.13.b shows a small shift of the simulated reflectance spectrum corresponding to the anionic layer with absorption towards shorter wavelengths with respect to the simulated reflectance spectrum with the corresponding anionic layer without absorption. Besides, the figure also shows a minor reduction of the simulated reflectance for the absorptive anionic layer what makes the simulated spectrum slightly more similar to the measured one.

In summary, the consideration of an absorptive anionic layer into the model induces a slight modification of the spectral Fabry-Pérot oscillations. This minor correction represents a tiny adaptation of the spectrum.

4.4 Conclusions

In this chapter, we exposed a numerical procedure which is based on 3D FDTD simulations in order to study their accuracy in the prediction of the optical behaviour of the NAA structures with a wide range of interpore distances. To this end, we collected reflectance measurements from real samples produced with oxalic (interpore distance smaller than wavelength) and with phosphoric (interpore distance of the order of wavelength) electrolytes. Subsequently, these real samples were simulated for each corresponding type of NAA structure. Henceforward, we considered various models of increasing geometric and chemical complexity in our simulations: i) a initial model that considers the flat aluminium-alumina and alumina-air interfaces, ii) a second model that considers the interface between the aluminium substrate and the alumina layer texturized with the hemispherical concavities caused by the preparation procedures, as well as the alumina barrier layer and the top surface of the alumina layer, iii) a third improved model that considers a anionic layer in the inner pore wall layer with distinct optical properties and iv) a last fourth model which contemplates absorption in the anionic layer.

The analysis of the computed results endorses us to conclude:

- The limits of the EMA-TMM approach has been entrenched with the assumption of flat interfaces between aluminium substrate and the alumina layer, and at the same time supports FDTD as more convenient method to apply.

- The assumption of flat interfaces is not appropriate for long interpore distances NAA. Although FDTD and EMA-TMM correctly predicts the optical behaviour for short interpore distances NAA, both methods fail in the prediction of the reflectance fall in the visible range for long interpore distances NAA.

- The consideration of the interfaces texturization leads to the expected reduction of reflectance for long interpore distances NAA in the visible range, meanwhile the reflectance for the short interpore distances NAA maintains a good agreement with the measured data.

- The inclusion into the model of an layer in the dual pore wall structure that takes into account different optical properties (with or without absorption) is traduced into a more distillate model predictions, leading to minor corrections of the obtained spectra with a better adjustment with the measured spectra.

In summary, the results presented in this chapter show that in order to have precise predictions of the optical behaviour of the NAA for a wide range of characteristics parameters of the structure, the consideration of the texturization of the interfaces is crucial. However, the consideration of the dual structure of the pore walls by the addition of a layer in the inner pore wall with different optical properties into the models introduces a next-to-leading order in the predictions, even though it allows a slight adjustment with the experimental measurements.

UNIVERSITAT ROVIRA I VIRGILI
NUMERICAL MODELLING OF NANOPOROUS ANODIC ALUMINA PHOTONIC STRUCTURES FOR OPTICAL BIOSENSING
Francisco Bertó Roselló

Chapter 5

Theoretical study of the optical behaviour of gold-coated NAA for optical biosensing

In this chapter, the optical response of a gold-coated NAA structure is analyzed using our FDTD simulation model developed in the previous chapter. Our goal is to study the suitability of gold-coated NAA structures as a platform for reflectometry-based plasmonic biosensors. In this sense, we start the study with numerical simulation of the reflectance spectrum of the gold-coated NAA structures. Next, the reflectance spectrum is simulated upon the adsorption of analytes which is modelled as a conformal "biolayer" on the gold coating layer and the inner pore walls. In this sense, a study on the coupling of the incident light to a localized surface plasmon resonance because of the nanostructuring provided by the pore arrangement with the absorption of the biolayer is presented. Finally, a sensitivity study on the biolayer thickness and the gold thickness is performed.

5.1 Introduction to plasmonic structures

Plasmonic structures have experimented a huge relevance in several investigation fields such as optical devices [Dragoman2008, Maier2001, Yokogawa2012], energy [Atwater2010, Pillai2010, Nakayama2008], or in more specific areas such as sensing or bio-sensing [Homola2008, Yanik2010, Nusz2009, Anker2008, Jain2008, Marinakos2007, Lee2011]. In addition, the use of enhanced spectroscopies in optical biosensing by means of enhanced spectroscopies has been widely reported. In this line, investigations

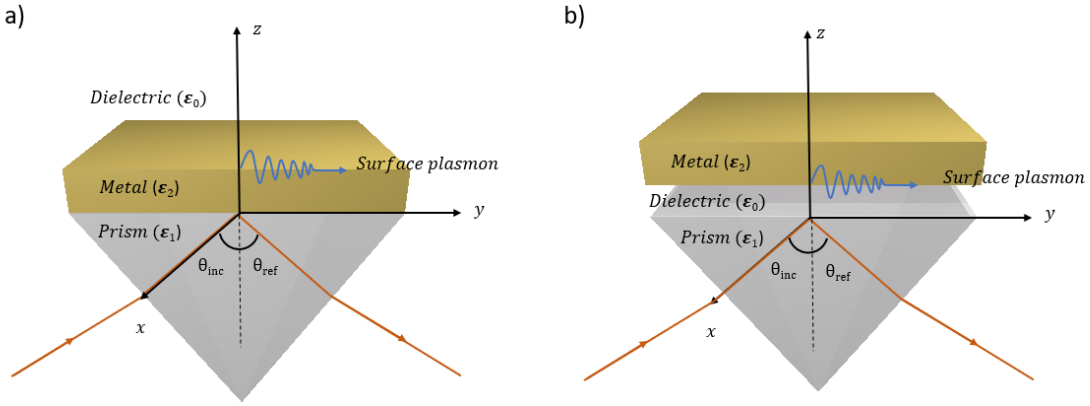

Fig. 5.1 Schematic view of (a) the Kretschmann and (b)Otto configurations for surface plasmon excitation.

on Surface Enhanced Fluorescence (SEF) [Damm2014, Abdulhalim2014, Gordon2008] and Surface Enhanced Raman Scattering (SERS) [Abdulhalim2014, Srivastava2015, Vo-Dinh2015] are some examples in the literature on the use of nanostructured plasmonic thin films in biosensing.

In general, these plasmonic structures consist of planar or nanostructured metallic elements which permit a sustained excitation of its surface plasmons (SP) [Zayats2005]. SPs are collective electronic excitations at a metal-dielectric interface that propagate like an electromagnetic waves along its planar surface. These SPs can be excited with an electromagnetic wave if the component of the wave vector of the incident light parallel to the metallic surface matches the wave vector of the parallel component of the surface plasmon. The SPs excitation can be carried out using different techniques and also using different type of nanostructures. Thus, basically SP's excitations can be classified into propagating surface plasmons (surface plasmon polaritons, SPP) or localized surface plasmons (LSP) [Gray2012].

There exist a wide variety of structures which can generate or provide a SPs excitation. Concerning SPPs, among the structures that can provide this excitation, the simplest one may be a metallic thin film on a dielectric substrate. The most commonly mechanisms to excite the SPP with this kind of structures are the Kretschmann and Otto configurations (figure 5.1). These configurations consist of illuminating a dielectric prism under the appropriate reflection conditions with its base coated with the metal. The incident light travels trough the prism and is reflected at the coated metal base. This generates an evanescent wave which penetrates the metal thin film propagating along its surface. Using the prism to adjust the incidence angle of the propagation the wave vector of the evanescent wave can be matched to the wave vector of the surface

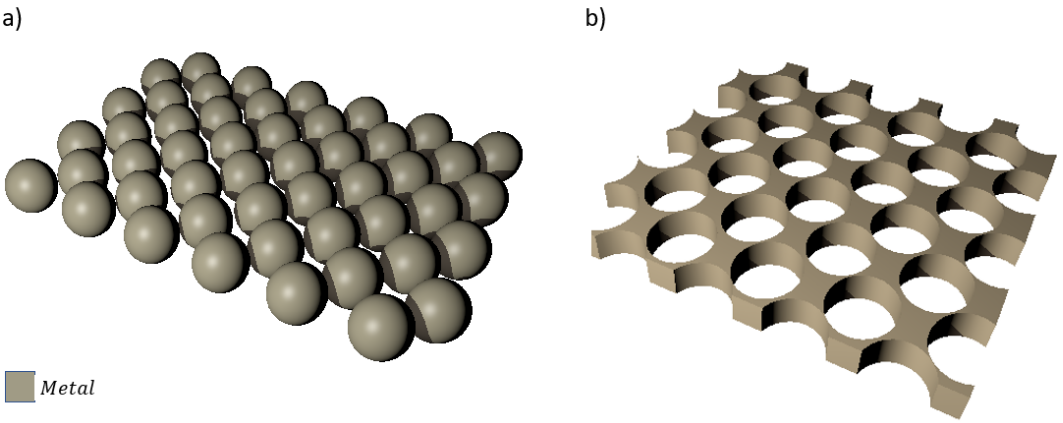

Fig. 5.2 Schematic view of (a) metallic nanoparticles array and (b) metallic nanoholes array.

plasmon, and therefore provide the optical excitations of the SPPs into the so-called surface plasmon resonance (SPR) [Homola2008]. The sensing principle of the system lies in the fact that the SPR is hugely sensitive to changes in the refractive index of the surrounding medium up to distances of a few hundred of nanometres from the metal surface.

On the other hand, LSPs are generated when the light interacts with metallic nanoparticles with sizes smaller that the wavelength of the incident light. In that case, this interaction leads to an oscillation of the plasmon around the nanoparticle with a resonant frequency corresponding to those of the excitation light (LSPR). Similar to the SPR case, the LSPRs are also very sensitive to changes in the refractive index of the surrounding medium. In contrast with the SPPs, the LSPs can be excited simply with the incident light without any intermediated mechanism. One of the most commonly mechanism to optically excite the LSPs is using metallic nanoscatterers. Figure 5.2 illustrates such scatterers as a metalic nanoparticles [LeifJ.Sherry2005] or nanoholes arrays [Kee2012].

5.1.1 Nanoporous plasmonic structures

In this chapter, we focus in structures with periodic arrays of nanoholes or nanopores in a thin slab of metal as a type of nanostructures that can sustain LSPs excitation. The periodic patterning of nanopores in a thin slab of a metal such a gold provides the appropriate conditions to optically excite the LSPs [Kee2012, Sannomiya2011].

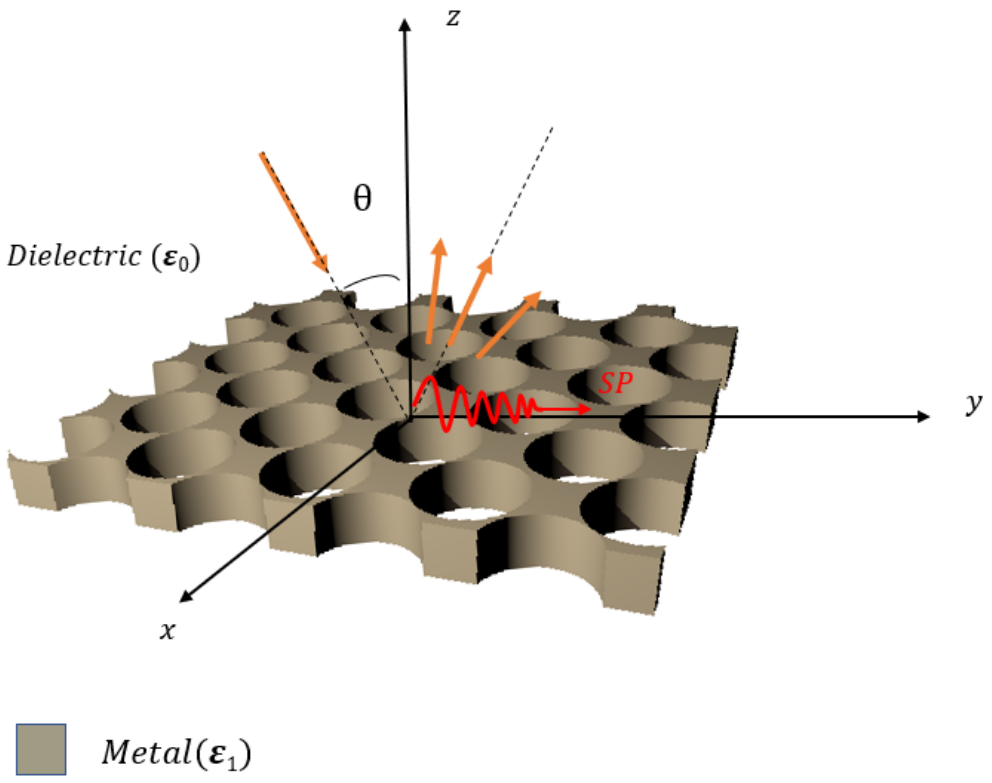

Fig. 5.3 Schematic view of the grating mechanism to optically excite the LSPs by a metallic nanoholes array. The nanopore patterning enables that the structure acts like a diffraction grating providing the mechanism to excite the LSPs.

Indeed, the pore patterning enables that the structure acts like a diffraction grating and therefore providing the mechanism to excite the LSPs (figure 5.3). Kee et al. [Kee2012] studied the optical behaviour of the porous gold-coated structures varying the pore diameter, the pitch, the gold film thickness, and the refractive index of the environment around the holes. The authors confirmed, among others in the literature, that the optical response corresponding to the LSPs generated or excited in periodic arrays of nanopores are strongly dependent of their geometrical parameters.

In order to perform the optical detection of analytes with this kind of structures it is necessary to consider the structures embedded in an aqueous medium. Formerly, the metal surface is functionalized to enable or enhance the chemical or biological binding analytes which finally are attached forming a biolayer. Figure 5.4 illustrates the analyte process binding in a liquid environment. Figure 5.4.a shows a schematic picture of the nanohole array with the analytes, whereas the figure 5.4.b shows a picture

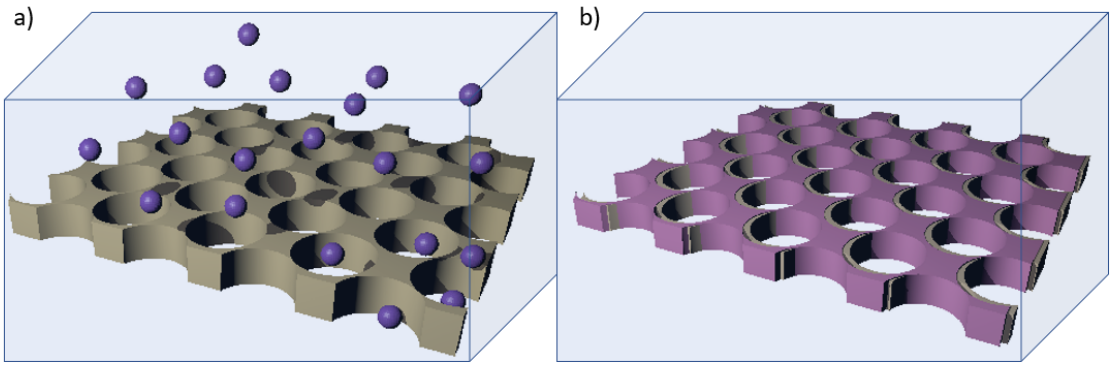

Fig. 5.4 Schematic view of (a) the chemical or biological binding analytes (purple spheres) in aqueous media (blue box) and (b) attached analytes forming a biolayer (purple coating layer).

illustrating the biolayer formation by attachment of these analytes. This biolayer changes the refractive index of the surrounding medium at the metal surface and into the pores which, in terms of optical behaviour, is translated into a shift in the resonant wavelength of the LSP [Stewart2008].

However, although this property makes this type of structures a suitable candidate for optical sensing, an important drawback indicates that caution must be applied. The current fabrication of very thin free-standing nanopatterned metal structures that can sustain LSP excitation may be extremely difficult to make. From this fabrication challenge, it is clear the necessity to take into account a substrate that allows to hold the nanoporous metal structure. However, the adoption of a substrate is not without its drawbacks. From the optical point of view, the chemical properties of the chosen material are determinant in the optical properties of the whole structure insofar as they significantly affect the optical response of the biosensor. Therefore, the choice of the material to be used as substrate is crucial.

5.1.2 Nanoporous anodic alumina as a substrate for plasmonic structures

Nanoporous anodic alumina (NAA) is a nanomaterial for which preparation technology has reached a remarkable level of control on its geometrical, physical and chemical properties by means of nanopore engineering [Ferre-Borrull2014].

Significantly interesting is the control over the interpore distance that can be achieved using different electrolyte compositions (i.e. with different acids electrolytes).

This distance fall up to in the range of a few tens of nanometres (using sulfuric acid electrolytes) from a few hundred nanometres (using oxalic or phosphoric acid electrolytes) [Kumeria2014, Lee2006a]. Additionally, the optical biosensing properties has been widely reported in the literature [Santos2013, Macias2013, Baranowska2014, Alvarez2009]. Reflectometric techniques can detect the changes in the refractive index of the NAA structure induced by an attachment of the analytes and the posterior formation of the bio-layer onto the inner pore walls. Thus, it is important to understand how the optical properties of the NAA vary with formation of such biolayer.

Therefore, the nanostructure of NAA makes it a good candidate to be used as a platform to hold a nanohole-structured gold thin film at its surface in order to realize plasmonic sensing devices [Macias2013, Hernandez-Eguia2014]. However, it should be noted that although the optical properties of these NAA structures are suitable for enhanced spectroscopies such as SERS and SEF biosensing, these are out of the scope of this work.

Here, we aim at studying, by means of numerical simulations, the suitability of gold-coated NAA structures for optical bio-sensing as a platform a biosensor by means of reflectometric techniques.

5.2 Description of the simulated structures

Figures 5.5, 5.6 and 5.8 illustrate the structures which we considered in the study of the LSPR generation in gold-coated NAA.

The basic structure we have simulated is a NAA membrane (NAAM). This consisted of a matrix of aluminium oxide with a hexagonal arrangement of cylindrical pores perpendicular to the surface (figure 5.5.a). In addition, figure 5.5.b illustrates the cross-section of two contiguous pores in this arrangement and indicates the main characteristic geometric parameters, namely the interpore distance (d_{int}), the pore diameter (d_p) and the pore length or depth (L). In this chapter, we considered two particular ranges of interpore distances: one corresponding to NAAM obtained with oxalic acid electrolytes (short interpore distances) and the second corresponding to NAAM obtained with phosphoric acid electrolytes (long interpore distances). The values of these geometric parameters corresponding to NAAM with short inter-pore distances were $d_{int} = 100\,nm$ and $d_p = 33\,nm$, whereas for the long inter-pore distances were $d_{int} = 450\,nm$ and $d_p = 150\,nm$. In both cases, we considered $L = 60\,\mu m$ for the pore length. Table 5.1 summarizes these geometric parameters for the NAA membranes produced with each acid electrolyte.

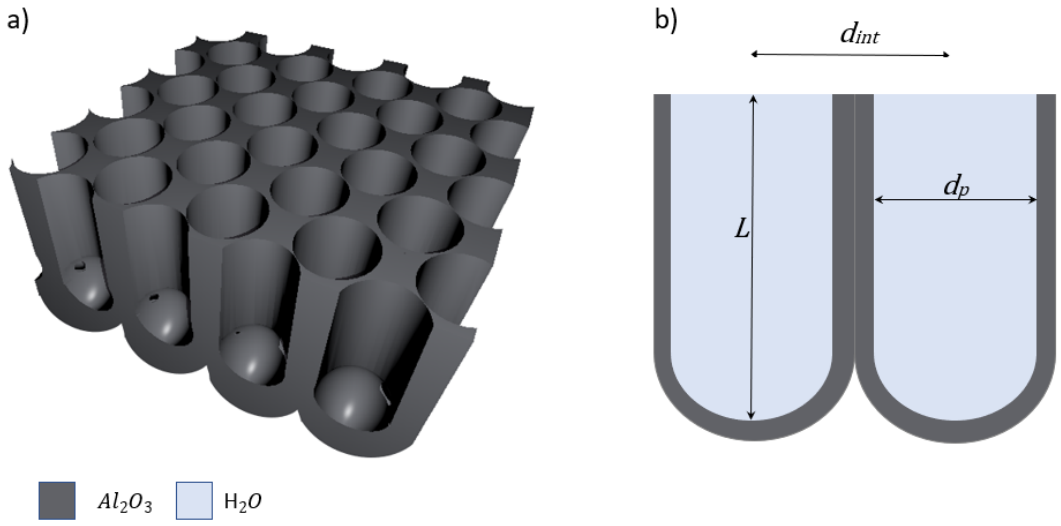

Fig. 5.5 Schematic view of the geometric model of the NAA membrane. The picture shows (a) a perspective view of the NAAM and (b) a cross section view of the basic geometric model, in which the main geometric parameters are indicated: the average interpore distance (d_{int}), the pore diameter (d_p) and the pore length or depth (L).

Table 5.1 Structural parameters considered in each NAA platform

Structural Parameter	Electrolyte acid	
	Oxalic	Phosphoric
$L(\mu m)$	60	60
d_p (nm)	33	150
d_{int} (nm)	100	450

The interpore distance values we considered have been taken from actual values reported from literature [Berto-Rosello2016]. Concerning the pore diameter values, they have been obtained from the interpore distance values by assuming an average porosity of 10% and an ideal hexagonal arrangement. It should be noted, that the porosity considered here is not casual. In Chapter 2, we have cited a key work of Nielsch et al. [Nielsch2002] in which the authors demonstrated that in order to obtain an optimum hexagonal pore arrangement in the self-ordered regimes using the two-step mild anodization process, the values for the porosity have to be about 10%.

In order to investigate the existence of LSPR on gold-coated NAAM, figure 5.6.a illustrates the same NAAM structure depicted in figure 5.5 with an additional gold

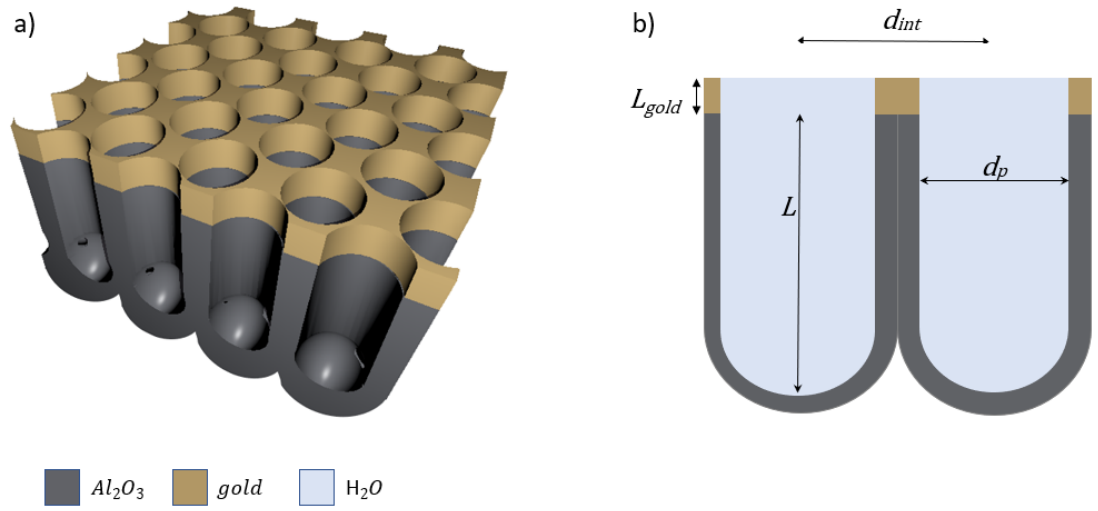

Fig. 5.6 Schematic view of the geometric model of the NAA membrane with the gold coating layer. The picture shows (a) a perspective view of the NAAM and (b) a cross section view of the geometric model, in which the main in addition to geometric parameters indicated in the figure 5.5, the gold layer thickness (L_{gold}) are also named.

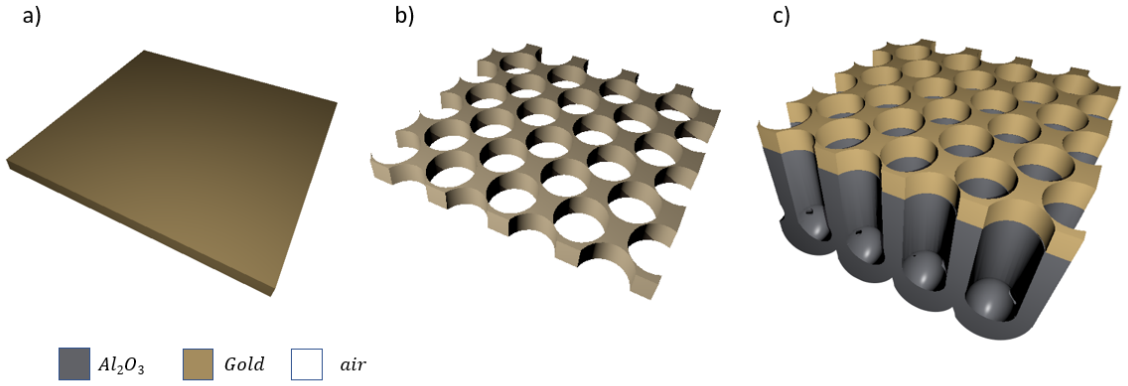

Fig. 5.7 Schematic view of the structures simulated for comparison. The picture shows (a) a continuous (non-porous) free-standing gold thin film, (b) a free-standing gold thin film with equivalent pore configuration as the corresponding NAA membrane and (c) a NAA membrane with the gold coating layer.

layer on top of the alumina matrix. Additionally, to provide a better readability of the geometrical parameters of the gold-coated NAAM, the figure 5.6.b shows a schematic picture of the pore structure with the gold-coating layer, where L_{gold} stands for the gold layer thickness. Here, at this point, a note it is necessary to point out. The gold layer is coating the top surface of the alumina matrix and it is not entering the pores.

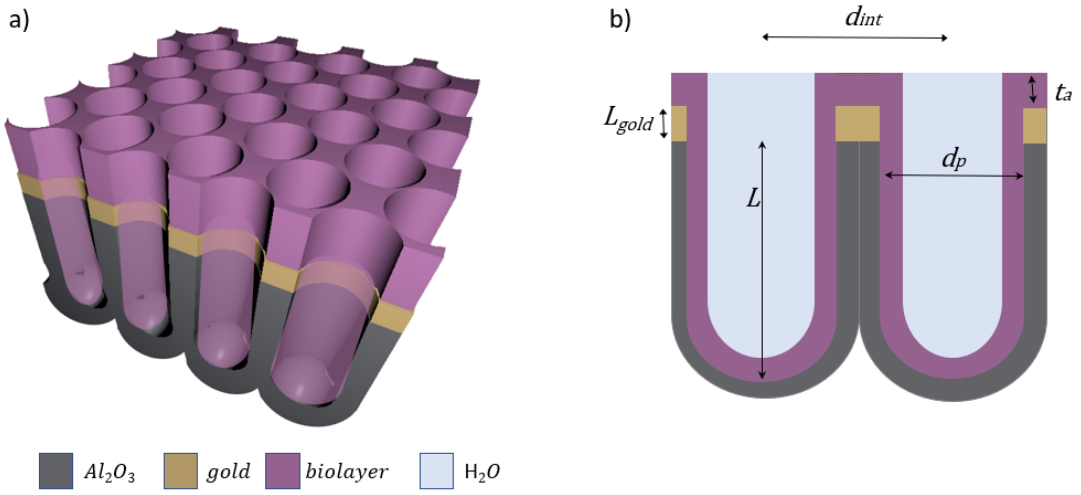

Fig. 5.8 Schematic view of the geometric model of the NAA membrane with the gold coating layer and the biolayer. The picture shows (a) a perspective view of the NAAM and (b) a cross section view of the geometric model with the gold coating layer and the biolayer indicating its main geometrical parameter, the layer thickness t_a.

Experimentally such structure can be produced by evaporating or sputtering gold on the NAA [Hernandez-Eguia2014].

In the simulations, this gold-coating layer thickness is varied between 20 nm and 70 nm. Three structures were considered for comparison and as reference, which are illustrates in figure 5.7: (a) a continuous (non-porous) free-standing gold thin film (figure 5.7.a), (b) a free-standing porous gold thin film and (c) a NAA membrane with the gold coating layer (5.7.c). It should be noted that the free-standing porous gold layer has a equivalent pore distribution as the corresponding NAA membrane.

The optical response of the different structures in the sensing process is simulated by considering that the medium filling the pores is water, with a refractive index of 1.33. The adsorption of the chemical/biological species to be detected onto the inner surface of the pores and on the gold surface was simulated as a conformal layer with a refractive index that can be different with respect to the medium filling the pores and with a given thickness (figure 5.8.a). From now on we will refer to this layer as a “biolayer". Figure 5.8.b illustrates such biolayer and indicates its main geometrical parameter, the layer thickness t_a.

5.3 Numerical modelling with FDTD and computational details

In order to model with FDTD, we follow the modelling procedure established in the chapter 3, using a commercial-grade FDTD-based simulator [Lumerical]. First, the definition of the computational domain for the FDTD calculations was established. Figure 5.9 shows both the computational domain and the unit cell designed for the simulations. Thus, the computational domain used in the simulations (Figure 5.9.a) had dimensions of d_{int} nm in the X direction, $\sqrt{3}d_{int}$ nm in the Y direction and 83 μm nm in the Z direction. The structure to simulate consists in a hexagonal array of cylindrical pores in an alumina matrix perpendicular to the surface with a porous gold-coating layer on the top with the same equivalent pore configuration. The NAA structure was designed from a rectangular unit cell in order to reproduce the hexagonal arrangement of pores and was placed in the centre of the computational domain (Figure 5.9.b).

As we have seen in chapter 4, and because of the domain definition, the computational cost for this kind of simulations could be very intensive. Taking advantage of the symmetry of the structure (2D-photonic crystal), periodic boundary conditions in the X and Y directions were applied in order to reduce the computational cost. As for the previous chapter, the computational time was reduced in a 25% and the periodicity in these directions was preserved. In the Z direction perfectly matched layers (PML) as a boundary condition were established, which will absorb the light in this direction and avoid the unwanted reflections. Next, the optical constants of each material we used were defined. The software we used has their own material database (based in ref. [Palik2012]) for the complex refractive index of each compound. The optical source was a plane wave incident on the alumina layer side with wavelengths in a range from 400 nm to 2000 nm. The direction of propagation was backwards in the Z direction and perpendicular to the structure (X-Y plane). Finally, a monitor at the top of the NAA structure to collect the optical reflectance spectrum as a function of wavelength was included.

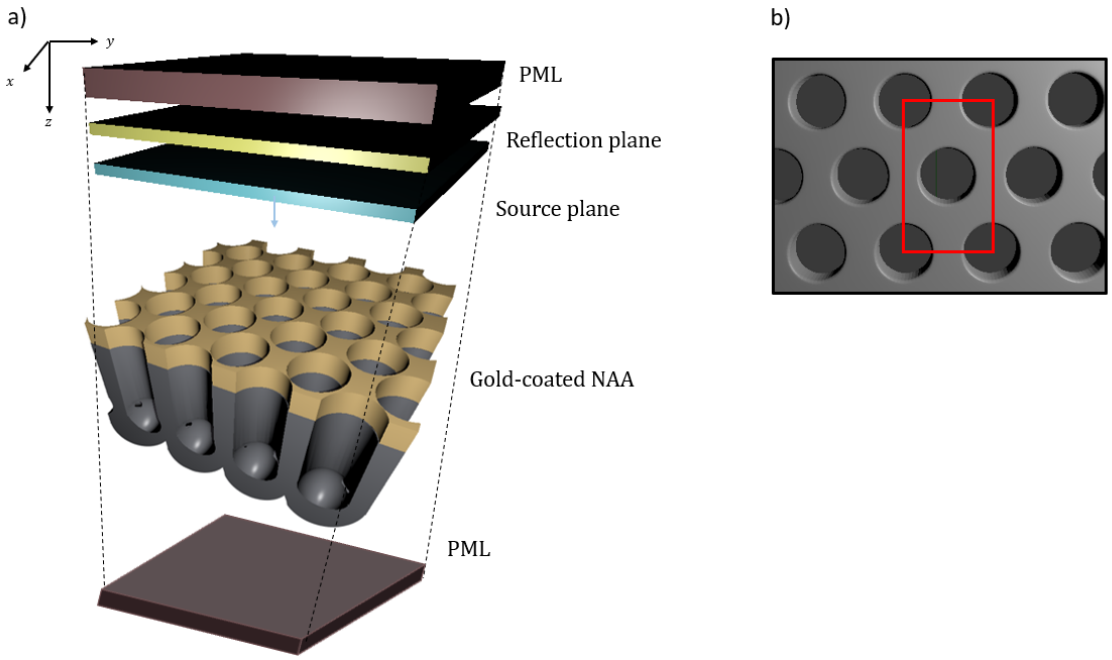

Fig. 5.9 Schematics of computational domain in FDTD. (a) Schematic view of the computational domain: R denotes the reflectance monitor, NAA refers the structure, PML for Perfectly Matched Layers and the source is explicitly indicated. (b) Plain view of the FDTD unit cell: the red square denotes the unit cell in the XY plane.

5.4 Study of the LSPR excitation on gold-coated NAA

In this section the sensing possibilities of the gold-coated NAAM with short and long interpore distances previously introduced are assessed.

The calculations of the optical reflectance spectra are performed considering the three structures previously defined (figure 5.7). Figure 5.10 shows the reflectance spectra of gold-coated NAAM structures considering a gold thickness of 20 nm (black curve). In the same figure the reflectance spectra of two related additional structures are depicted: the corresponding for a free-standing non-porous gold thin film with the same thickness (dotted green curve) and a free-standing porous gold thin film (dashed red curve) also with the same thickness and with equivalent pore structure to the NAAM. Although the considered free-standing structures in air are not a realistic case, their spectra permit a comparison with those of the gold-coated NAAM.

Figure 5.10.a corresponds to short interpore distance NAAM produced with oxalic acid electrolyte while 5.10.b corresponds to long interpore distance NAAm produced with phosphoric acid electrolyte. For all the structures considered the reflectance

spectra presents a similar behaviour: a gradual decrease with decreasing wavelength with a significantly marked drop in the visible wavelengths.

For the short interpore distance structures (figure 5.10.a), it can be observed that the reflectance of the free-standing porous gold thin film shows a minor dip around 600 nm, not present for the free-standing solid gold thin film. Such a little dip observed in the porous gold thin film is in good agreement with the predictions of ref. [Martin-Moreno2001] and thus it can be concluded that the nanoporous patterning in the gold layer acts like a diffraction grating enabling the coupling of the incident light to LSPs. The analysis of the spectrum corresponding to the gold-coated NAAM reveals a similar plasmonic resonance-related dip but redshifted respect to the previous one. This fact suggests that despite of the NAA porous substrate, the light coupling to the localized surface plasmons is produced.

Consider now the case of the gold-coated NAA with long interpore distance (figure 5.10.b). The analysis of the picture indicates that the porous patterning of the gold thin film induces also a plasmonic resonance, but in this case, the observed dip is deeper (i.e. with much stronger intensity) than in the short interpore distance. The sharp dip is present in the spectrum corresponding to the free-standing porous gold thin film and in the corresponding to the gold-coated NAAM. In the case of the free-standing porous gold thin film the major resonance is centred approximately at 750 nm, with additional secondary minor dips around 800 nm and 1350 nm. Similar resonances are present in the spectrum corresponding to the gold-coated NAAM, but here are redshifted with respect to the previous ones, being approximately at 875 nm, with additional secondary minor dips around 975 nm and 1350 nm.

The present results are significant in at least two major respects. First, these results comes to demonstrate that a gold coating thin layer deposited onto NAAM may be suitable as platform to couple normally incident light onto localized surface plasmon resonances. And second, the results indicates that the interpore distance is a decisive key parameter that strongly influences the coupling efficiency to the resonance. Thus, according to this, NAAM with long interpore distance which can be produced in phosphoric acid electrolytes, are more convenient in order to sustain LSP resonances that can be further applied to sensing.

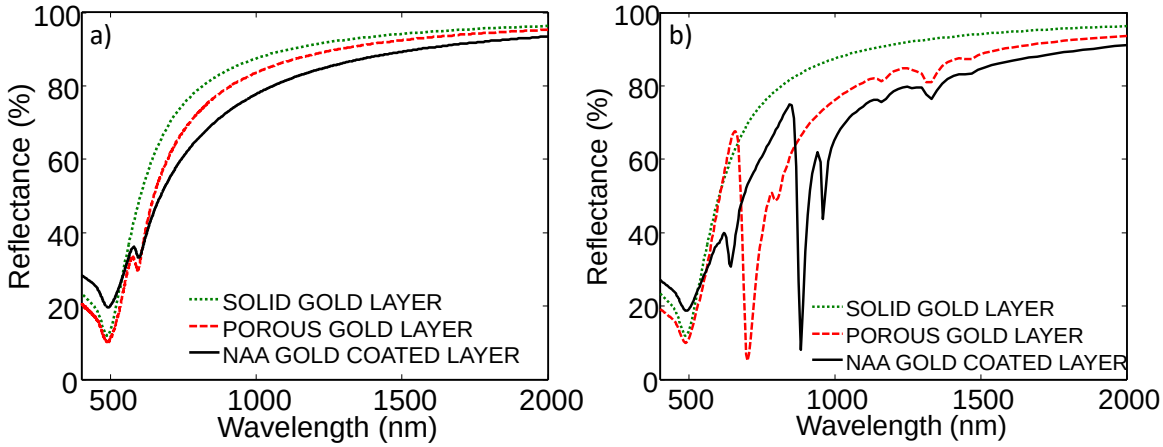

Fig. 5.10 Calculated reflectance spectra of gold-coated NAA structures with a gold thickness of 20 *nm*. a) NAA structures with to short interpore distance while b) corresponds to long interpore distance. The curve in black corresponds to the reflectance spectra for the gold-coated NAA, whereas the dotted green curve corresponds to a gold thin film with the same thickness and the dashed red curve corresponds to a porous gold thin film with the same thickness and with equivalent pore structure to the NAA. Adapted from [Berto-Rosello2018].

5.4.1 Influence of the gold-coated NAAM thickness on the LSPR excitation

Having established that the porous gold-coated NAAM may be suitable as platform for optical biosensing and having demonstrated that the interpore distance is a decisive key parameter as a key point to obtain a LSPR, we will now move on to discuss the influence on the LSPR of the gold thin film thickness deposited on the long interpore distance NAA.

To this end, the gold layer thickness was varied from 20 *nm* to 70 *nm* in steps of 10 *nm* in the simulations. Figure 5.11 illustrates the obtained results, showing the calculated reflectance spectra in the range between 750 *nm* and 1000 *nm* and plotted for the different gold thicknesses.

The picture shows the same two dips already observed in figure 5.10.b for all the studied cases. In this case, however, a blue shift of the main dip as the gold thickness increases is observed. Similarly to the main dip, it can be observed that the secondary dip also experiments a blue shift but to a much smaller extent. Furthermore, it is important to point out that as the gold layer thickness increases the main dip

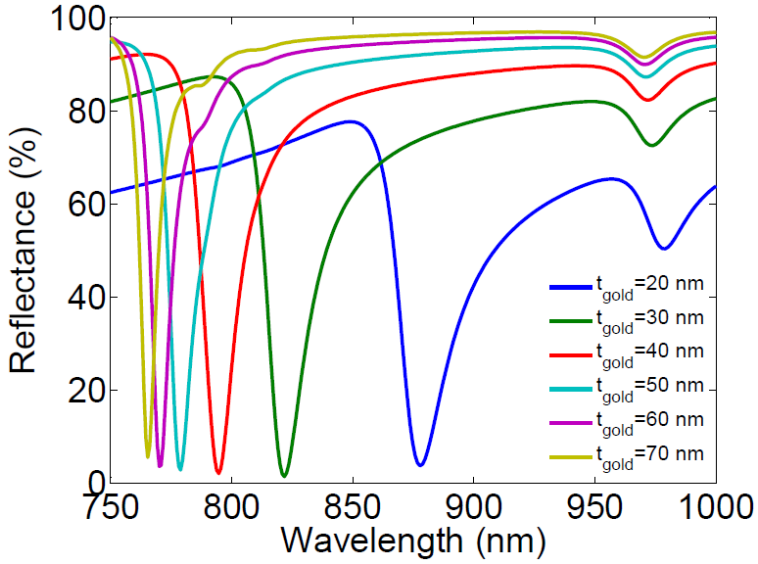

Fig. 5.11 Plot of the calculated reflectance spectra for gold-coated NAAM structure with the long interpore distance varying the gold layer thickness from 20 *nm* to 70 *nm*. Adapted from [Berto-Rosello2018].

becomes narrower. The width of such dip could be meaningful when considering sensing applications, which will be discussed in the next sections.

5.5 Study of LSPR sensing with gold-coated NAAM

This section is devoted to the theoretical evaluation of the possibility of using the existence of LSPR in the spectra of gold-coated NAAM described in the previous section as a sensing mechanism. The basis of such mechanism would lie on the selective detection or quantification of the specific analytes attached onto the gold surface or onto the inner NAAM pore surface.

In order to carry out and assess this feasibility, the attached analytes were modelled as a biolayer (figure 5.8) with a specific thickness and a refractive index different to that medium which fills the pores. From a quantitative point of view, a parameter which permits us to evaluate the sensing mechanism by comparison between the different NAAM is needed. Thus, a sensitivity parameter is defined as the rate of change in the LSP resonant wavelength for increasing refractive index of the biolayer.

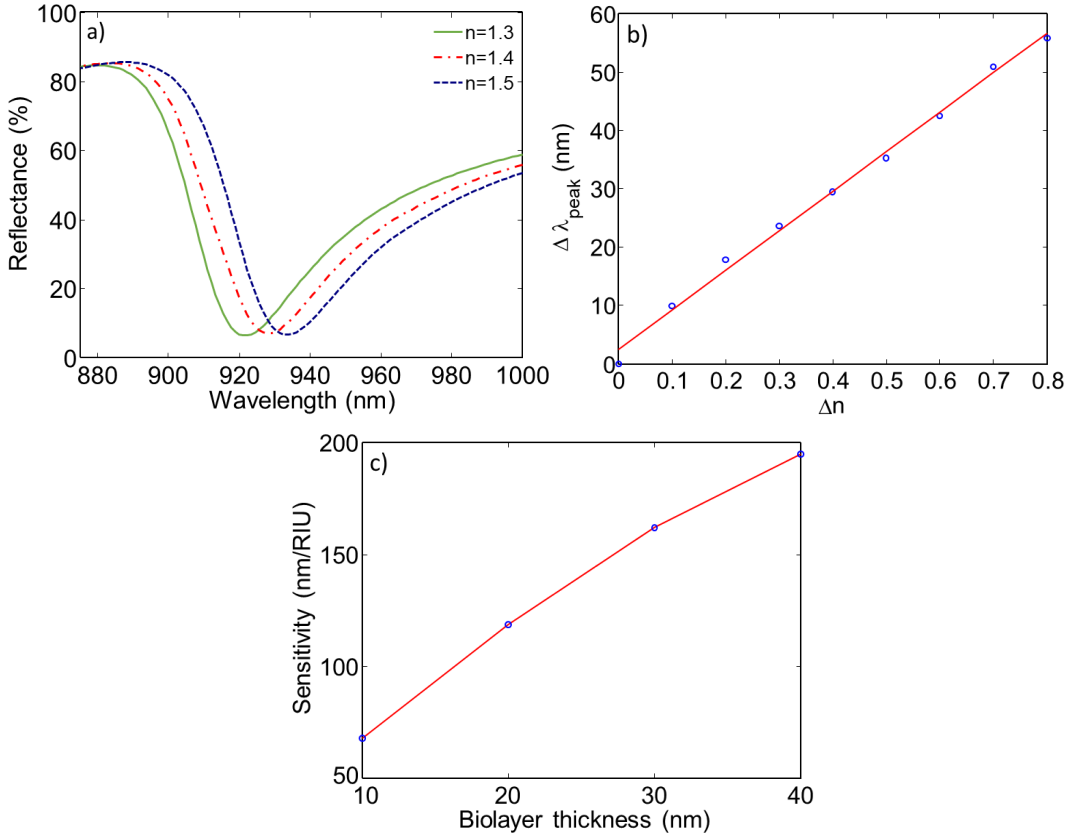

Fig. 5.12 Optical study for the gold-coated NAAM. a) Simulated reflectance of the gold-coated NAA under three different values of the biolayer refractive index. b) Simulated optical sensitivity of the gold-coated NAA defined as the slope of the linear trend ($S = \frac{\Delta\lambda_{dip}}{\Delta n}$). c) Simulated optical sensitivity as a function of the biolayer thickness. Adapted from [Berto-Rosello2018].

Figure 5.12.a shows reflectance spectra in the range of the LSPR dip corresponding to the gold-coated NAAM with a gold thin film thickness of 20 nm and a biolayer of 10 nm thickness. In order to provide a comparison, the figure also plots the gold-coated NAAM spectra for different refractive index values of the biolayer. The graph shows in red and blue dashed lines the spectra corresponding to the structure with a refractive index of the biolayer of $n = 1.4$ and $n = 1.5$ respectively, in contrast with the green solid line corresponding to the aqueous medium ($n_{water} = 1.33$). The plot reveals an increasing LSPR wavelength as the biolayer refractive index increases. In order to estimate the trend of this increase, additional calculations of the resonant wavelength with different refractive index of the biolayer were performed. The figure 5.12.b illustrates this trend plotting the resonant frequency shift ($\Delta\lambda_{dip}$) as a function

of the refractive index difference (Δn). The picture shows a linear dependence between this two quantities, from which the slope of this linear trend ($S = \frac{\Delta\lambda_{dip}}{\Delta n}$) can be defined as sensitivity parameter. These results suggest that the considered structure could be suitable for sensing, insofar it is theoretically capable of producing a shift in the resonant dip under changes on the biolayer refractive index.

Additionally to the biolayer refractive index, the biolayer thickness can influence the LSPR wavelength position. In order to estimate such influence, figure 5.12.c depicts the dependence of the NAMM sensitivity for different biolayer thicknesses in a range from 10 nm to 40 nm. The plot reveals an increase of the sensitivity S with the biolayer thickness. This result is in the line as it could be expected from the fact that more biolayer material is in interaction with the electric field. However, the observed increasing trend is nonlinear. The results suggest that a biolayer with a bigger thickness does not result in a proportional increase of the sensitivity.

5.5.1 Optimization of the sensitivity as a function of the gold thin film thickness

In the previous section, the optical response of gold-coated NAAM and its suitability for sensing based on the refractive index difference and on the biolayer thickness has been demonstrated. Difficulties arise, however, when an attempt is made to implement real sensing experiments. In that case, the currently chemical or biological analytes to be detected influences these two aforementioned parameters related to the biolayer.

In the fabrication process of the NAAM some structural parameters such as the interpore distance or the pore diameter are usually fixed. This fact leaves the thickness of the gold-coated layer as a free parameter to optimize the sensitivity of the gold-coated NAAM.

In this section, the influence of the gold thin film thickness on the sensitivity is studied. A higher sensitivity reached by the NAAM biosensor would imply a bigger shift in the resonant wavelength upon the adsorption of the species detected. However, as described in the previous section, the width of the LSPR dip depends strongly on the gold thin film thickness (figure 5.11). That implies that with a increase of this width, it would be more difficult to recognize a shift in LSPR wavelength.

In order to quantify the optimum degree of sensitivity in relation with the width of the LSPR dip, the quality factor (Q-factor) is defined. Q-factor is a figure of merit for the width of resonant peaks or dips defined as Q-factor $= \frac{\Delta\lambda_{FWHM}}{\lambda_{dip}}$, where $\Delta\lambda_{FWHM}$ is the full width at half the maximum (or minimum) in wavelength units. Thus, it is

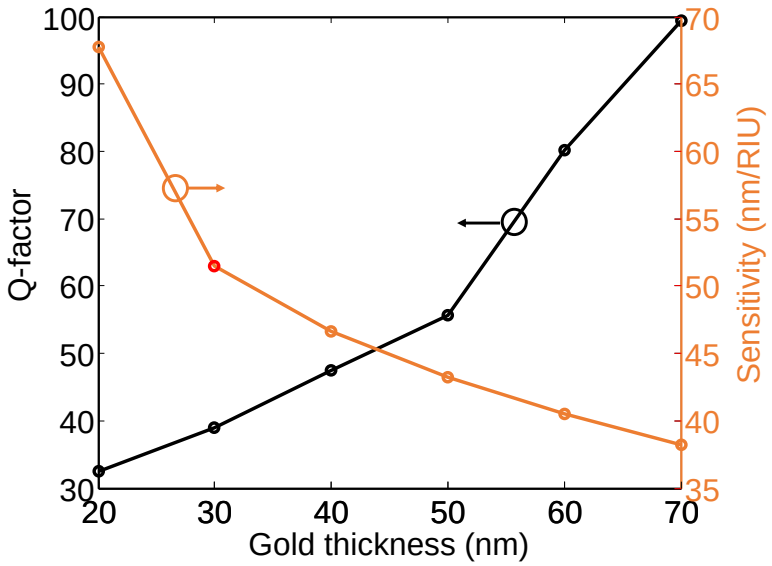

Fig. 5.13 Quality factor and optical sensitivity for a gold-coated NAA as a function of the gold thin film thickness. Quality factor and optical sensitivity for different gold thickness in the range from 20 *nm* to 70 *nm* with the biolayer thickness fixed to 10 *nm*. Adapted from [Berto-Rosello2018].

important to consider both sensitivity and Q-factor in order to evaluate the sensing capabilities of gold-coated NAA.

Figure 5.13 shows two plots corresponding to the sensitivity (orange Y-axis) and the Q-factor (black Y-axis) for gold-coated NAAM as a function of the gold thin film thickness. The thickness of the biolayer in the simulations was fixed to 10 *nm*, although the same conclusions can be reached with other biolayer thicknesses. The figure plots the calculated sensitivity as a function of the gold layer thickness (orange line), showing a decrease of the sensitivity as the gold thin film thickness increases. The picture also shows a plot of the calculated Q-factor. In this case, the plot shows an increasing Q-factor as the gold thin film thickness increase.

This result reveals the existence of a trade-off between the shift of the resonant wavelength and the ability to measure the shift in the spectrum. This fact suggests that there exists an optimal value of gold thin film thickness that permits reaching simultaneously the maximum possible sensitivity and Q-factor. Nevertheless, such optimal value depends of a specific application, as it would depend on the current values of refractive index difference and biolayer thickness for each specific analyte to be detected. Furthermore, it would depend on other experimental measurement parameters such as spectrometer resolution or detector noise.

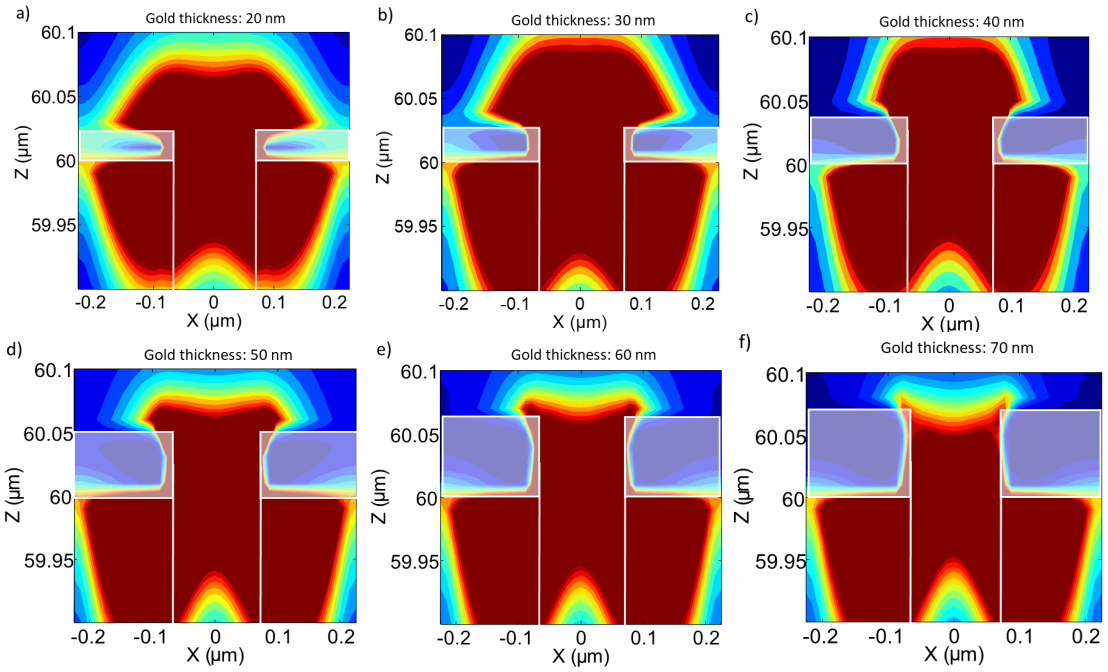

Fig. 5.14 Electric field intensity profiles for the gold-coated NAA with different gold layer thicknesess (shadowed top layer). Electric field intensity profiles at an XZ plane centred in the middle of the pore for gold layer thicknesses in a range from a) 20 *nm* to f) 70 *nm*. Adapted from [Berto-Rosello2018].

In order to understand the decrease in sensitivity of the NAAM with the increasing gold thin film thickness, a study of the electromagnetic field distribution in the vicinity of the gold-coating layer has been carried out. Figure 5.14 illustrates the electric field intensity profiles at the resonant wavelength centred at an XZ plane in the middle of the pore for gold layer thicknesses in a range from 20 *nm* to 70 *nm*. The area occupied by the gold thin film is indicated by the shadowed rectangles, while the area occupied by the alumina is indicated by the rectangles below the gold. The biolayer forms a conformal coating of 10 *nm* thick on the gold and the inner pore surface (not depicted in the figure). From a closer analysis of the figure, it can be observed that, as the gold thin film thickness increases, the region occupied by the highest field intensities on top of the metallic and on the pore walls decreases. Thus, the overlap with the biolayer becomes smaller which leads to a decrease of the resonant wavelength shift and therefore a decrease in the sensitivity.

5.6 Conclusions

In this chapter, the capabilities of gold-coated nanoporous anodic alumina membranes as reflectometry-based plasmonic platforms for biosensors has been studied. The study has been carried out by numerical simulation of the reflectance spectrum of the gold-coated NAAM upon the attachment of analytes (biolayer) on the gold coating and the inner pore walls. 3D-FDTD numerical simulations have been performed on two types of NAAM structures: NAAM with short interpore distances which corresponds to NAA obtained with oxalic acid electrolytes, and NAAM with long interpore distance which corresponds to NAA obtained with sulfuric acid electrolytes. The capability of coupling a localized surface plasmon resonance from an incident beam has been studied by comparing the reflectance spectra of the short and long interpore distance gold-coated NAA with that of a solid gold film and for a nanopatterned gold film with the same distribution of holes as in NAAM, both with the same thickness as the coating on the NAAM. The attachment of the chemical/biological analytes to be detected onto the inner surface of the pores and on the gold surface forming the biolayer has been modelled as a conformal layer with a refractive index that can be different with respect to the medium filling the pores and with a given thickness.

The analysis of the computed results permits us to conclude:

- The nanostructuring provided by the pore distribution of the NAAM enables that normally incident light couples to a plasmon resonance in the gold coating of the NAAM. That coupling depends strongly on the NAAM interpore distance, being much more efficient for the gold-coated NAAM with long interpore distances.

- Numerical simulations demonstrate that the attachment of a biolayer on the gold coating and on the inner pore walls produces a shift on the resonant wavelength of the plasmon resonance. The shift shows a linear dependence with the refractive index of the biolayer, what permits to define the sensitivity as the shift of the resonant wavelength per refractive index unit. This sensitivity increases with the thickness of the biolayer.

- The sensitivity decreases as the thickness of the gold thin film on the NAAM increases. This result can be explained by studying the electric field distribution produced by the different gold thicknesses: a lower thickness results in a larger fraction of the electric field in the space region where the biolayer deposits, resulting in a greater interaction volume. However, the resonance Q-factor increases as the gold thin film increases. Therefore, an increase in sensitivity has

the disadvantage of a decrease in the resonance Q-factor, which can reduce the resolution in the measurement of the shift under experimental conditions. This suggests that an optimal thickness of the gold coating has to be determined for each specific experimental conditions

In summary, the results presented in this chapter show the possibility to use the gold-coated NAAM as a platform for plasmonic biosensors by means of reflectometric methods. The use of long interpore distances NAAM to hold nanopatterned hole arrays on a gold thin film layer permits a direct coupling of the incident light with the plasmons on the metal, providing an alternative to experimental configurations such as Kretchsmann and Otto to obtain plasmonic excitations. Furthermore, this gold-coated NAAM permits the definition of a sensitivity function, which can be optimized for a specific gold thin film layer and a specific analyte to detect.

UNIVERSITAT ROVIRA I VIRGILI
NUMERICAL MODELLING OF NANOPOROUS ANODIC ALUMINA PHOTONIC STRUCTURES FOR OPTICAL BIOSENSING
Francisco Bertó Roselló

Chapter 6

Analysis and modelling of the optical response of NAA-based graded-index structures

In the previous chapters, we have showed the development of a numerical procedure based on FDTD that has been applied to predict the optical behaviour of NAA structures. Specifically, we have modelled the optical response of a set of samples composed of a monolayer of alumina on aluminium substrate, calculating in result its reflectance spectrum and comparing it with the corresponding experimental spectrum. That permits us to test the model and to improve it in order to achieve more accurate results. Next, a theoretical study of the optical behaviour of a gold-coated NAA structure has been proposed in order to investigate the possibility to use NAA-based structures as a platform to future plasmonic biosensors. As a result of the application of our model, reflectance calculations have been obtained, demonstrating that long interpore gold-coated NAA membranes could be suitable as the basis in the development of this kind of plasmonic devices.

However, there are a wide set of NAA structures which can be used as a platforms for optical biosensors such as NAA-based distributed Bragg reflectors [Rahman2013], NAA-based micro cavities [Macias2013] and NAA rugate filters [Macias2014]. The geometrical and chemical characteristics of these type of structures has been briefly explained in chapter 2, whereas in chapter 3 we provided an introduction on different types of numerical methods to model their optical response. Unfortunately, the use of the FDTD method for this kind of structures could have such a huge computational cost making it unaffordable. For this reason, alternative methods to FDTD must be considered. If we consider these complex structures with an interpore distance smaller

that the incident wavelength, the transfer matrix method can be a powerful and faster choice.

This chapter is devoted to study the optical behaviour of NAA rugate filters as a NAA-based graded-index structures, in which a modulation in depth of its pore diameter has been considered. These kind of NAA structures are the so-called NAA rugate filters (NAA-RF) which we have seen in chapter 2. These structures are geometrically characterized by having a sinusoidal pore modulation in depth of its pore diameter which can be obtained applying an anodization current with a sinusoidal component in the fabrication process. In result, the optical behaviour of this NAA-RF is characterized by showing a narrow peak (photonic stop band) in a specific wavelength range in its reflectance spectrum. Our goal is to investigate by numerical modelling the optical photonic stop gap behaviour of the NAA-RF and its relationship with the fabrication parameters .

6.1 Introduction

In the previous chapters, the optical properties of NAA structures and gold-coated NAA thin films has been studied considering them as a 3D nanostructured material. Thereby, the effective refractive index of these structures has been measured and calculated, as well as the variation of this effective index when biological or chemical species have been attached on the top of the structure and onto the pore walls. However, as we pointed in chapter 2, the 3D nanostructuring of the NAA is possible and confers further properties to the NAA or improves the existing ones.

One of the procedures for achieving 3D NAA is the pulse anodization [Lee2008]. This procedure permits to fabricate NAA structures breaking the cylindrical shape of the pores and giving a 3D pore morphology to the NAA, combining a low-potential pulse followed by another high-potential pulse with periods and amplitudes intentionally designed. In this sense, Lee et al. in [Lee2008] achieved a 3D nanostructured NAA-DBR. Following this procedure, Chen et al. [Chen2015] also produced photonic NAA-based DBRs by pulse anodization. The authors highly controlled the nanopore geometry of the NAA structure producing photonic structures with vivid colours in the UV-visible spectrum range.

Another type of procedure to modify the NAA pore morphology, also described in chapter 2, is the cyclic anodization. Losic et al. [Losic2009a] developed this procedure employing periodic oscillating parameters in the anodization current to achieve, for instance, NAA-based rugate filters (NAA-RFs).

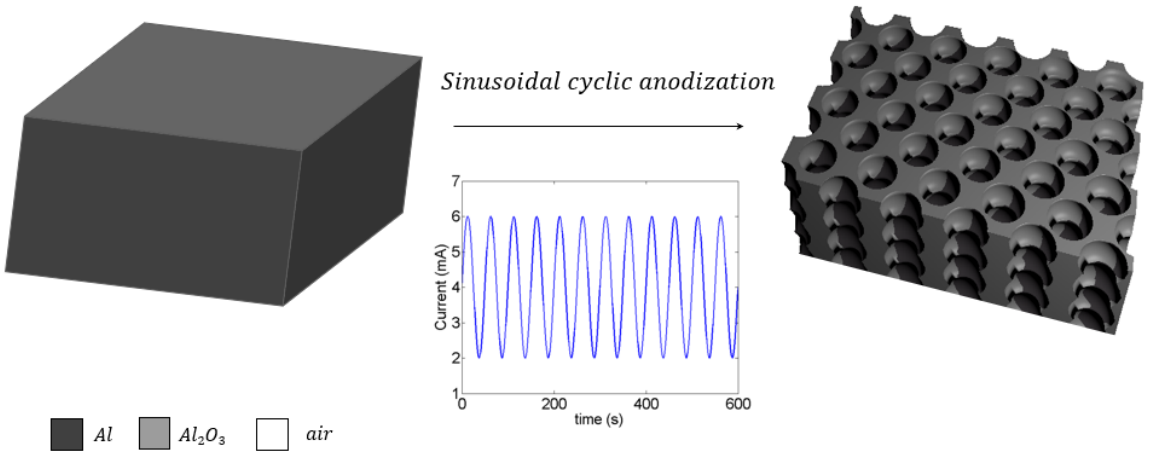

Fig. 6.1 Schematic concept of the aluminium anodization into a ordered NAA-RF by sinusoidal pulse anodisation.

NAA-RFs are NAA-based structures consisting of a matrix of aluminium oxide with a distribution (disordered or hexagonally arranged) of pores perpendicular to its surface, which have a periodical oscillation of its diameter with the depth. The NAA-RFs are produced by applying a sinusoidal anodization current profile such as:

$$I(t) = I_0 + I_1 sin(\frac{2\pi t}{T}) \tag{6.1}$$

where I_0 is an offset current (equivalent to the anodization current in constant current anodization), and I_1 and T are the amplitude and period of the sinusoidal component.

Figure 6.1 illustrates a schematic view of the NAA-RF structure achieved with this sinusoidal cyclic anodization of the aluminium process. The resulting pore morphology is schematically illustrated in detail in figure 6.2. In the picture we can observe the amplitude in the modulation of the pore diameter (Δd_p) on the pore length period (Δ) which can describe the pore modulation in depth.

There are a variety of researches on NAA-RFs in the literature. We cite that of Ferré-Borrull et al. [Ferre-Borrull2014] as an example. The authors fabricated NAA-RFs using the cyclic anodization process by a variation of the current from galvanostatic conditions. The authors applied a sinusoidal profile on the anodization current to create the pore modulation in depth. As another example of NAA-RFs investigation, Santos et al. [Santos2016] reported structurally engineered NAA-RFs produced by sinusoidal pulse anodization.

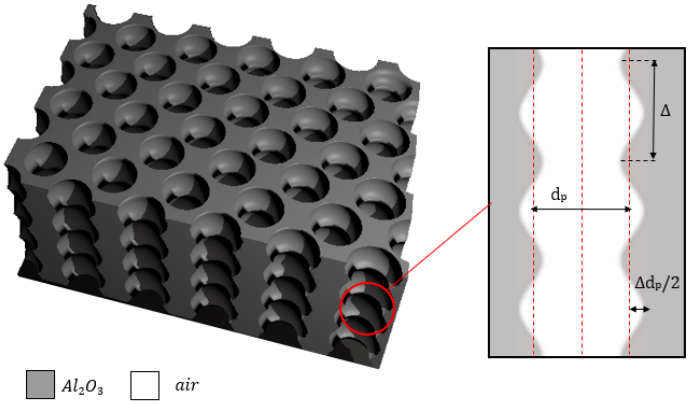

Fig. 6.2 Schematic NAA pore morphology with cyclic anodization: (a) 3D perspective view sketch and (b) 2D planar cross section sketch.

These studies revealed that the NAA-RFs show photonic stop bands in its reflectance spectra. The geometrical parameters such as the interpore distance d_{int}, the pore diameter (d_p), the modulation of the pore diameter (Δd_p) and the modulation period along the pore length (Δ) influence the photonic stop bands properties such as its position, its width and its strength. Consequently, these optical properties can be tuned with high precision, resulting in NAA photonic structures that can be used as a platforms in the development of optical biosensors.

Our goal in this chapter is to investigate by means of numerical modelling and with experimental measurements the optical NAA-RFs properties in order to relate the geometrical parameters (d_{int}, d_p, Δd_p and Δ) with the fabrication parameters (I_0, I_1 and T).

6.2 Fabrication and characterization of the NAA-RF samples

Nanoporous anodic alumina rugate filters were prepared by anodizing aluminium through the anodization process described elsewhere [Ferre-Borrull2014]. Before the anodization the aluminium foils were electropolished using a $HClO_4 : EtOH$ mixture 1:4 v/v at 20 V for 4 min. Next, the anodization was carried out in a 0.3 M aqueous solution of oxalic acidic electrolyte ($H_2C_2O_4$) at 5 ºC. In this step, five different sinusoidal anodization profiles were used to generate five samples of NAA-RFs (named

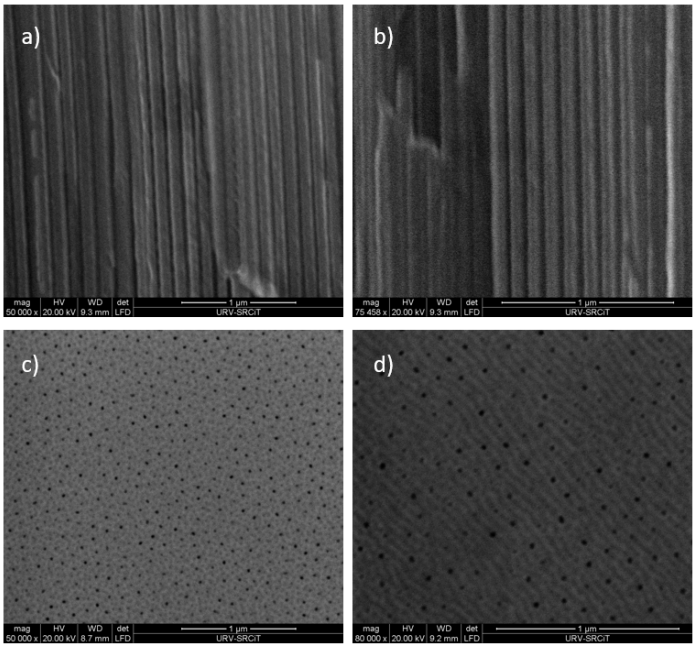

Fig. 6.3 Cross-sectional and top view SEM image of the NAA-RF structure produced at a specific I_0 value. The pictures are at different scale to provide a better view of the pores. Courtesy of L.K. Acosta, Universitat Rovira i Virgili.

$S1$ to $S5$, respectively) with different in-depth variations of the NAA structure. The samples were produced using the anodization current profile described in eq.(6.1) varying the offset current I_0 and maintaining fixed the amplitude current (I_1), the period (T) and the number of cycles (N). When the anodization process finished, the aluminium substrate was removed using a wet chemical etching with HCl and $CuCl_2$. Figure 6.3 illustrates a cross section view and a top view SEM pictures of one of the samples as a reference. The pictures are at different scale to a better view of the pores.

In order to characterize the samples, spectroscopic reflectance measurements were carried out. To this end, a Lambda 950 spectrophotometer from PerkinElmer (Whaltham, MA, USA) equipped with a tungsten lamp as the light source and using a Universal Reflectance Attachment is used. The incidence angle was set very close to the normal incidence (6^o) and the wavelength range was set from 350 nm to 900 nm.

Figure 6.4.a shows the measured reflectance spectra of the NAA-RFs samples for each offset current (I_0) considered. Here, the five spectra are illustrated: the black line corresponds to the sample $S1$ with $I_0 = 2.5\ mA$, the green line corresponds to the sample $S2$ with $I_0 = 3\ mA$, the blue line corresponds to the sample $S3$ with $I_0 = 3.5\ mA$, the red line corresponds to the sample $S4$ with $I_0 = 4\ mA$, and finally the brown line corresponds to the sample $S5$ with $I_0 = 4.5\ mA$. In all cases a photonic stop

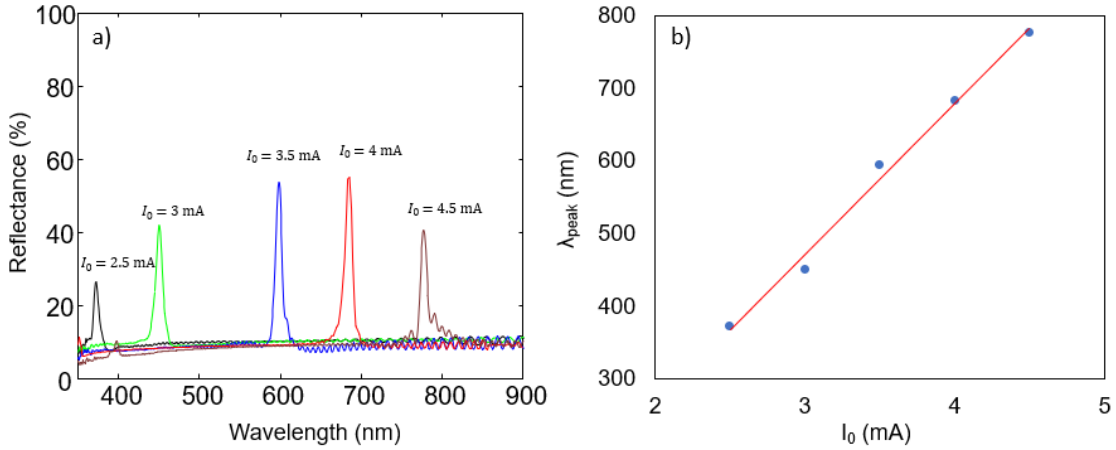

Fig. 6.4 a) Measured reflectance of the NAA-RF samples where the offset current I_0 varies, maintaining fixed the amplitude current (I_1), the period (T) and the number of cycles (N). b) Linear dependence of the measured PSB central wavelength position of the NAA-RFs samples with each offset current (I_0) considered.

band (PSB) in the specified rang is observed. NAA-RFs which its oscillating variation of the pore diameter in depth induces a periodic variation of the refractive index of the NAA-RF that results in a PSB in the direction of variation. The graph shows a significant increase in the central wavelength position of PSB as the offset current (I_0) increases. In order to estimate the trend of this increase, additional calculations of the PSB central wavelength position for different offset current were performed. Figure 6.4.b shows the measured PSB central wavelength position of the NAA-RFs samples for each offset current (I_0) considered, revealing a linear dependence between this two quantities.

Using the same procedure previously described, a sinusoidal anodization profile in which the three different amplitude current were used to generate three additional samples of NAA-RFs with different characteristics. The three types of NAA-RFs were produced varying amplitude current I_1 and maintaining fixed the offset current (I_0), the period (T) and the number of cycles (N). The characterization of the samples by spectroscopic reflectance measurements were carried out as for the previous case.

Figure 6.5 shows the measured reflectance spectra of the NAA-RFs for each amplitude current (I_1) considered. Here, the three spectra are illustrated: the green red line corresponds to the sample $S6$ with $I_1 = 1\ mA$, the black line corresponds to the sample $S7$ with $I_1 = 1.5\ mA$, and the red line corresponds to the sample $S8$ with $I_1 = 2\ mA$. As the previous case, a photonic stop band (PSB) in the reflectance spectrum of each sample is observed. The plot shows that the maximum PSB reflectance is different for

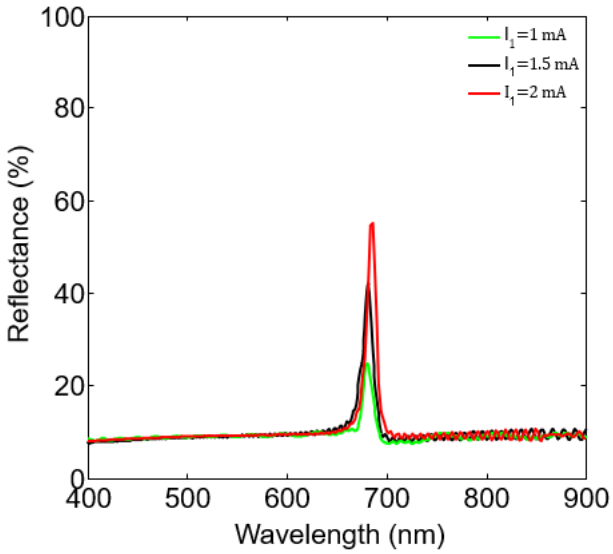

Fig. 6.5 Measured reflectance of the NAA-RF samples where the amplitude current I_1 varies, maintaining fixed the offset current (I_0), the period (T) and the number of cycles (N).

different I_1. The graph reveals an increase of the maximum reflectance of the PSB as increasing I_1. However, in contrast to the previous case, the picture shows that the central wavelength position of PSB remains almost in the same position despite of the amplitude current (I_1) increases.

6.3 Design and numerical modelling

As we have explained in Chapter 3, in the case of thin film modelling with EMA, flat interfaces and layers of homogeneous materials have to be considered. The EMA permits to obtain the effective refractive index of such layers when one of the materials in the structure is actually a mixture of materials [D.A.G.Bruggeman]. Figure 6.3 illustrates a cross-section SEM image of one of the considered samples which shows the oscillating pattern in depth of the pore diameter. However, the pore diameter (d_p) and its variation in amplitude (Δd_p) are hard to evaluate from the pictures. Thus, in order to accomplish such challenge, the EMA simulations were designed by considering the NAA-RF structure as a multilayer system. The pore morphology of the NAA-RF induces a modification in depth of the porosity which results in a continuous transition of the refractive index in depth. The figure 6.6 shows a schematic view of the EMA

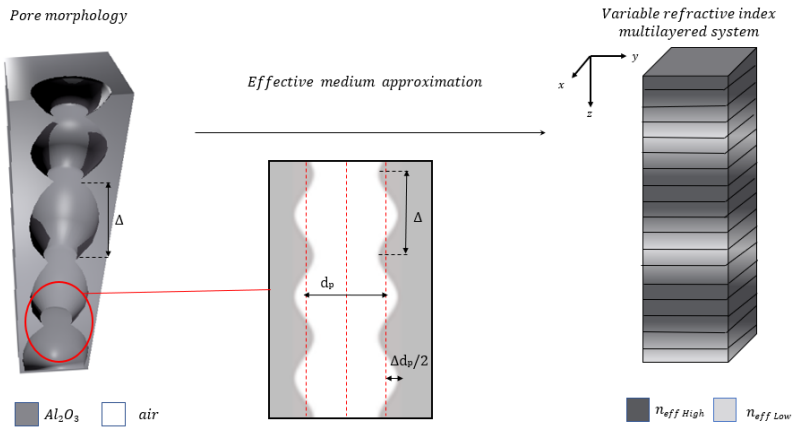

Fig. 6.6 Illustration of the transition of the NAA-RF pore geometry into an effective graded index structure in the Z direction. The continuous variation of the refractive index is between n_{High} and n_{Low}.

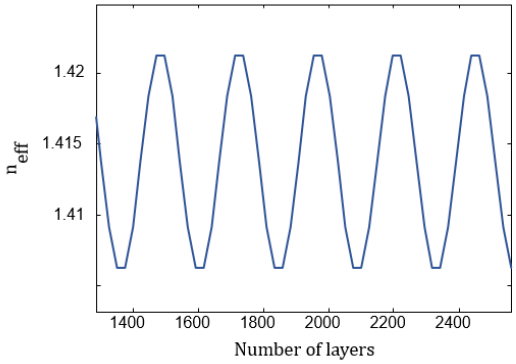

Fig. 6.7 Illustration of the resulting modulation of the effective refractive index with the depth.

model and how the resulting effective system is formed, whereas the figure 6.7 shows the modulation of the effective refractive index in depth.

The calculation of the reflectance spectra will be performed by means of transfer matrix method which implies that a multi-layered thin film model with constant refractive index for each layer is needed. For this reason, the picture shows a final multi-layered system in which each period in the pore modulation is divided in 10 layers with constant index. The effective refractive index of each layer can be calculated by means of the Looyenga-Landau-Lifshitz (3L) formula [Alekseev2007] , in combination with that reported from Bartzsch et al. in [Bartzsch2004] in which the effective index profile oscillates between a high refractive index (n_{High}) and a low refractive index (n_{Low}). The formula is described in the equation (6.2):

Table 6.1 Estimated average interpore distance for each sample with different offset current (I_0).

Sample	Offset current (mA)	Interpore distance (nm)
S1	2.5 mA	79 nm
S2	3 mA	87 nm
S3	3.5 mA	94 nm
S4	4 mA	96 nm
S5	4.5 mA	117 nm

$$n(z) = n_{mean} + \frac{n_{range}}{2} sin\Big(\frac{2\pi}{\Delta} z\Big) \tag{6.2}$$

where $n_{mean} = \frac{1}{2}(n_{High} + n_{Low})$ is the average refractive index and $n_{range} = n_{High} - n_{Low}$ is the peak variation, Δ is the thickness of one oscillation period and z is the distance variable in depth.

6.4 Study of the NAA-RF reflectance spectra and its relationship with the fabrication parameters

In order to reproduce the experimental reflectance spectra, calculated reflectance spectra are analysed by adjusting the geometrical parameters d_{int}, d_p, Δd_p and Δ to obtain the best fit between the experimental and the calculated reflectance.

In the simulations, the interpore distance, d_{int}, and the modulation period, Δ, are established to a value previously estimated from SEM top view pictures and cross-section pictures of prepared samples at the same average current. By applying image analysis to the SEM pictures, the average interpore distance was estimated for each sample. Table 6.1 summarizes this average interpore distance for each sample, from which a linear relation between d_{int} and I_0 could be established:

$$d_{int} = 17 I_0 + 35 \tag{6.3}$$

Concerning the modulation period Δ, figure 6.8 shows a cross-sectional view SEM image of a NAA-RF sample. From the picture the total thickness (L) could be established, and therefore it could be deduced that the physical thickness of one period is given by

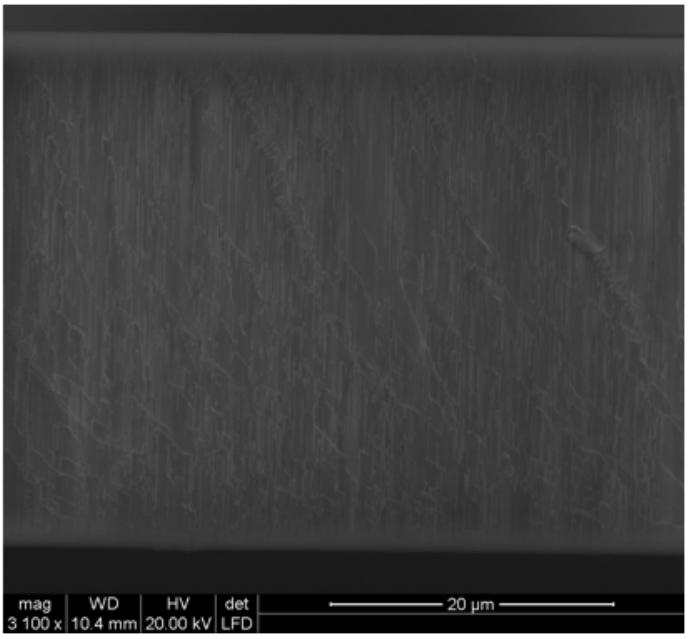

Fig. 6.8 Cross-sectional view SEM image of the NAA-RF sample produced at a specific offset current (I_0) value.

$$\Delta = 302TI_0 \tag{6.4}$$

where I_0 is in mA and T in seconds. Pore modulation amplitude was established to $\Delta d_p = 2\ nm$.

Figure 6.9 depicts the reflectance spectra obtained in the simulations. The picture shows the measured reflectance spectra (red line) for the five samples with different offset currents (I_0) together with the corresponding simulated reflectance spectra (blue line) in order to provide comparison. The numerical model developed is able to reproduce the experimental central wavelengths of the PSB, although with higher calculated maximum reflectance. This difference is caused by the imperfections in the experimental preparation.

Figure 6.10 illustrates the pore diameter used in the best fitting for each I_0. Simulation results reveal an increasing trend of the pore diameter with increasing I_0, as it could be expected. However, further analysis will be necessary in order to relate the pore modulation amplitude to the current modulation amplitude.

The model we developed permits the analysis of measured reflectance spectra and by means of a best fitting establish a relationship between the fabrication parameters

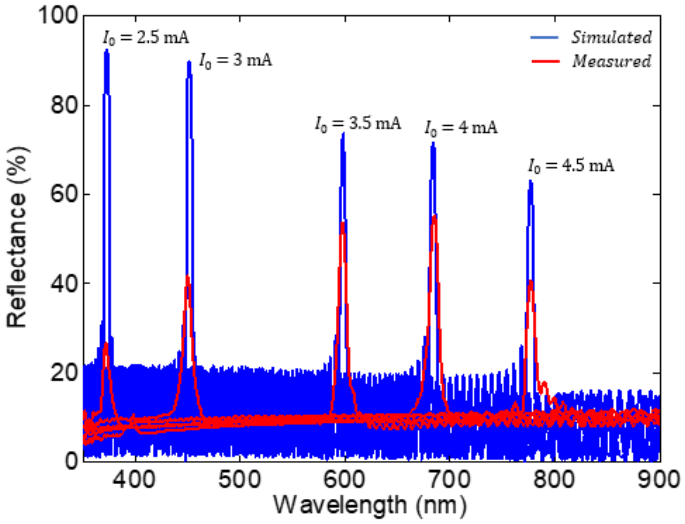

Fig. 6.9 Calculated reflectance of the NAA-RF samples where the offset current I_0 vary, maintaining fixed the amplitude current (I_1), the period (T) and the number of cycles (N).

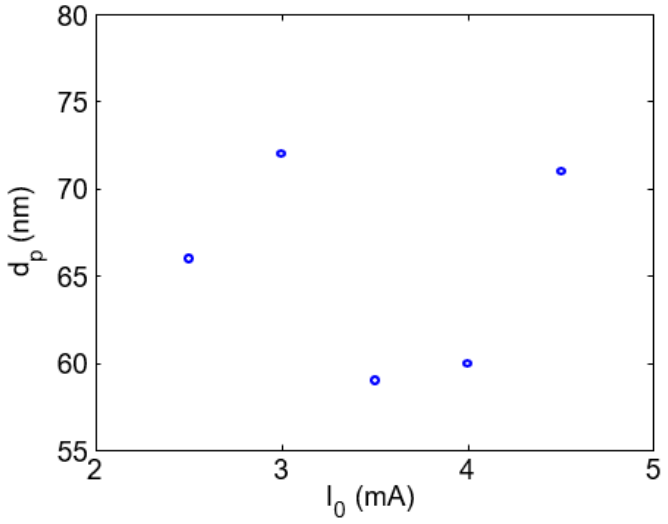

Fig. 6.10 Calculated pore diameter of the NAA-RF samples in function of the offset current I_0, maintaining fixed the amplitude current (I_1), the period (T) and the number of cycles (N).

with the geometric characteristics of NAA-RF. Table 6.2 summarizes the relationship of the fabrication parameters with the geometric characteristics of the NAA-RF.

Table 6.2 Relationship of the fabrication parameters with the geometric characteristics of NAA-RF.

Fabrication parameters			Geometric characteristics			
T (s)	I_0 (mA)	I_1 (mA)	d_{int} (nm)	d_p (nm)	Δd_p(nm)	Δ(nm)
200	2.5	2	79	66	2	151
200	3	2	87	72	2	181
200	3.5	2	94	59	2	211
200	4	2	96	60	2	242
200	4.5	2	117	71	2	272

6.4.1 Influence of the pore modulation amplitude on the reflectance spectrum

Figure 6.11 summarizes the reflectance spectra obtained in the simulations for the three samples ($S6$, $S7$ and $S8$) with different amplitude currents (I_1). Figure 6.11.a shows the reflectance results obtained in the simulations for the sample $S6$ with $I_1 = 1$ mA, the figure 6.11.b shows those corresponding to the sample $S7$ with $I_1 = 1.5$ mA and 6.11.c deals with the corresponding to the sample $S8$ with $I_1 = 2$ mA. The pictures show the measured reflectance spectra (red line) for each sample with the specific amplitude current (I_1) together with the corresponding best fitting (blue line) by adjusting Δd_p in order to provide comparison.

As the results depicted in figure 6.9, the measured spectra also show the photonic stop bands (PSB) as a result of the oscillating variation of the refractive index in the NAA-RF. However, the central wavelength position of each PSB is not affected by the increase of I_1. In contrast, a variation on the intensity of the maximum reflectance is observed which increases as the I_1 increases.

The numerical model developed is able to reproduce the trend of the central wavelengths of the PSB, although with a little deviation reproducing the spectrum for the sample $S6$. This difference may be caused by imperfections in the experimental preparation.

6.5 Study of sensing with NAA-RFs

This section is devoted to the theoretical evaluation of the possibility of using the existence of PSBs in the spectra of NAA-RFs described in the previous section as a sensing mechanism. The basis of such mechanism would lie on the detection or

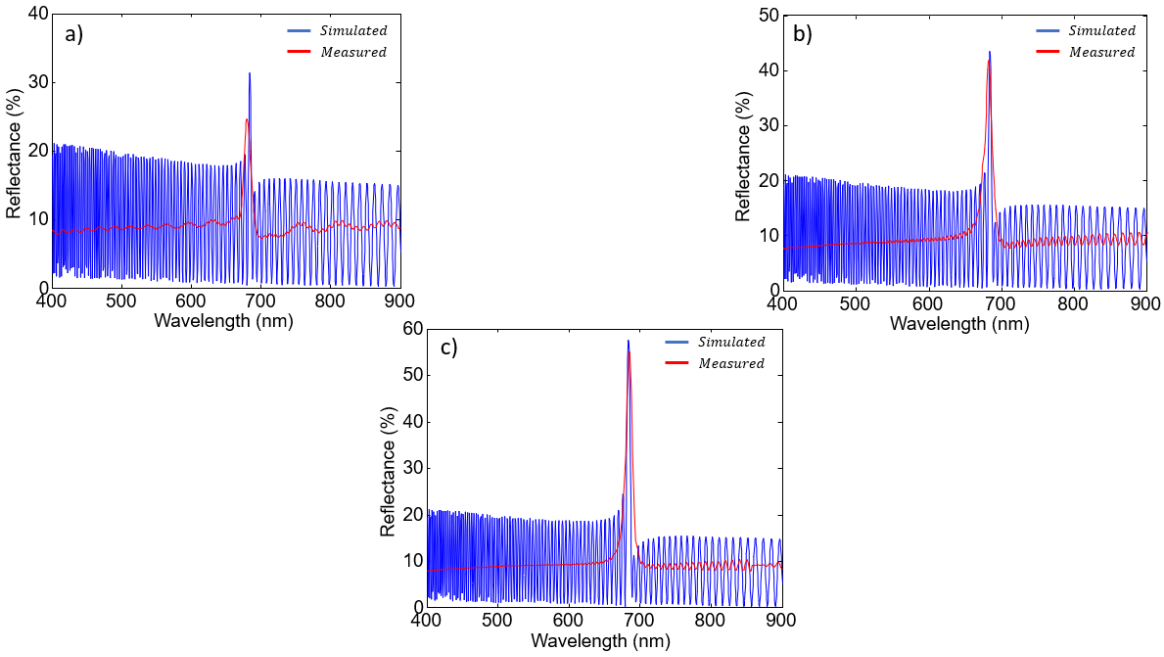

Fig. 6.11 Experimental and calculated reflectance (indicated in the legend) of the NAA-RF samples maintaining fixed the offset current (I_0), the period (T) and the number of cycles (N), and varying the amplitude current for: (a) $I_1 = 1\ mA$, (b) $I_1 = 1.5\ mA$ and (c) $I_1 = 2\ mA$.

quantification of the specific analytes present in aqueous solution in the medium which fills the pores. In order to carry out and assess this possibility, the analytes were modelled considering different refractive index for that medium, which indicates an increasing presence of analytes. From a quantitative point of view, a parameter which permits us to evaluate the sensing mechanism by comparison between the different NAA-RFs is needed. Thus, a sensitivity parameter is defined as the rate of change in the PSB central wavelength position for increasing refractive index of the medium.

Figure 6.12.a shows reflectance spectra corresponding to the NAA-RF sample $S4$ with $I_0 = 4\ mA$ for different refractive index values of the medium that fills the pores in order to provide comparison. The legend in the graph indicates the corresponding spectrum for each refractive index. In the graph, if we consider the reflectance spectrum of the NAA-RF filled with water ($n = 1.33$) as a reference, the plot reveals a shift of the central wavelength of the PSB towards higher wavelengths as the refractive index of the medium that fills the pores increases.

In order to estimate the trend of this increase, additional calculations of the central PSB wavelength with different refractive index of the pore filling medium were performed. Figure 6.12.b illustrates this trend plotting the central PSB wavelength

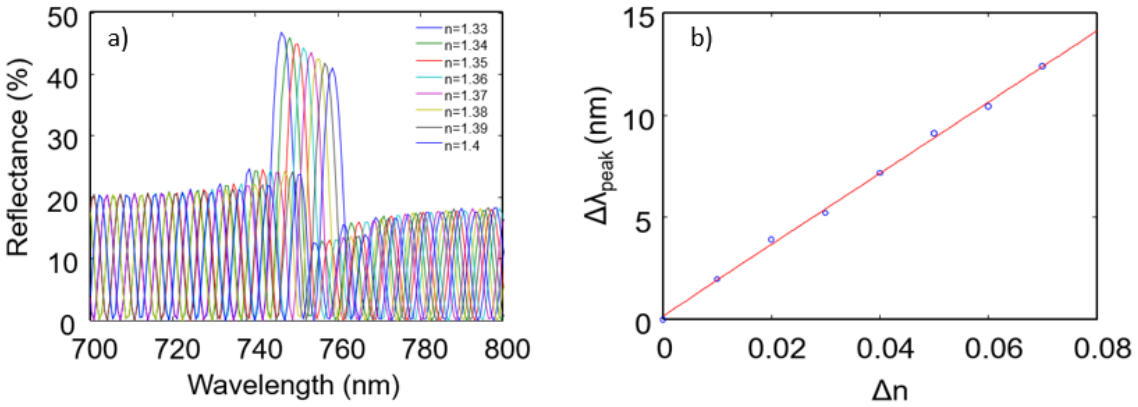

Fig. 6.12 Optical study of the NAA-RF. a) Simulated reflectance of the NAA-RF under different values of the pore filling medium refractive index. b) Simulated optical sensitivity of the NAA-RF defined as the slope of the linear trend ($S = \frac{\Delta\lambda_{dip}}{\Delta n}$).

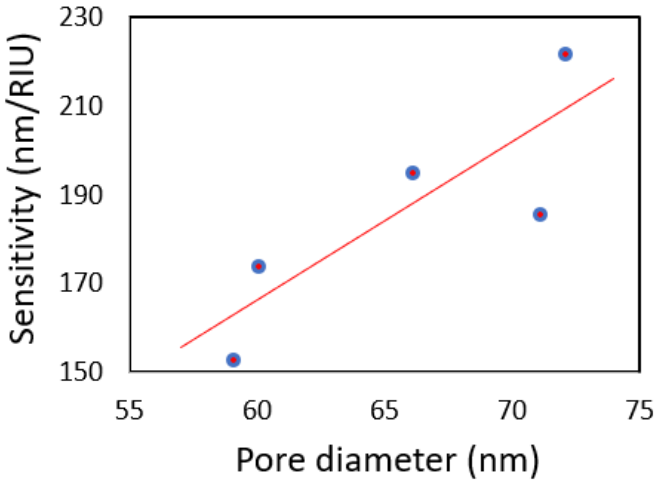

Fig. 6.13 Effect of the d_p on the NAA-RF sensitivity.

variation ($\Delta\lambda_{peak}$) as a function of the refractive index difference (Δn). The picture shows a linear dependence between this two quantities, from which the slope of this linear trend ($S = \frac{\Delta\lambda_{peak}}{\Delta n}$) can be defined as sensitivity parameter. These results suggest that the considered structure could be suitable for sensing, insofar it is theoretically capable of producing a shift of central PSB wavelength under changes on the pore filling medium refractive index.

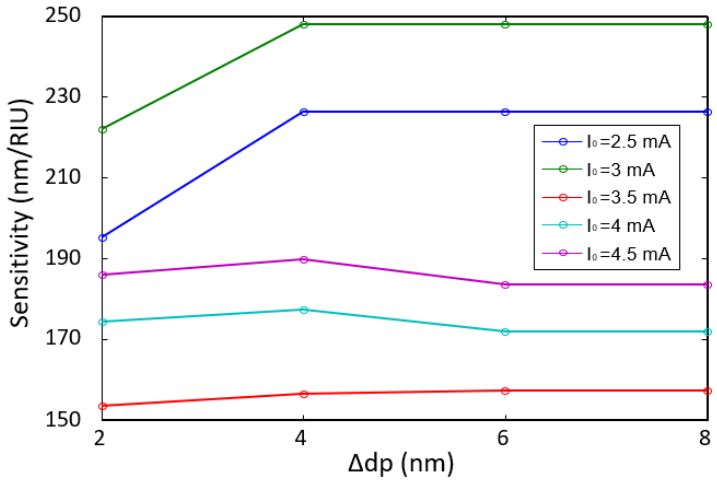

Fig. 6.14 Effect of the Δd_p on the NAA-RF sensitivity.

6.5.1 Influence of the pore diameter and the pore modulation amplitude on the sensitivity

Additional calculations were made in order to achieve a better understanding on the sensing capabilities of the NAA-RF. Figure 6.13 depicts the dependence of the sensitivity for different pore diameters in order to estimate such influence. The plot reveals an increase of the sensitivity S with the pore diameter. However, although the results suggest a increasing trend of the sensitivity with the pore diameter, more data would be needed in order to confirm the linearity of the trend.

On the other hand, a sensitivity study is made in function of Δd_p in a range from 2 nm to 8 nm for each I_0. Figure 6.14 shows the dependence of the sensitivity for different pore modulation amplitudes (Δd_p) in order to estimate such influence. The graph reveals almost a constant behaviour of the sensitivity as the Δd_p increases, although the sensitivity of two samples show a little increase in the first section of the interval of Δd_p. This constant behaviour of the sensitivity suggests that it is not influenced by Δd_p.

6.6 Alternative NAA-RF sensing with a narrowband emission light source

In this section, an alternative method of sensing with NAA-RFs is proposed and evaluated. Figure 6.15 illustrates a schematic concept of the proposed sensing system.

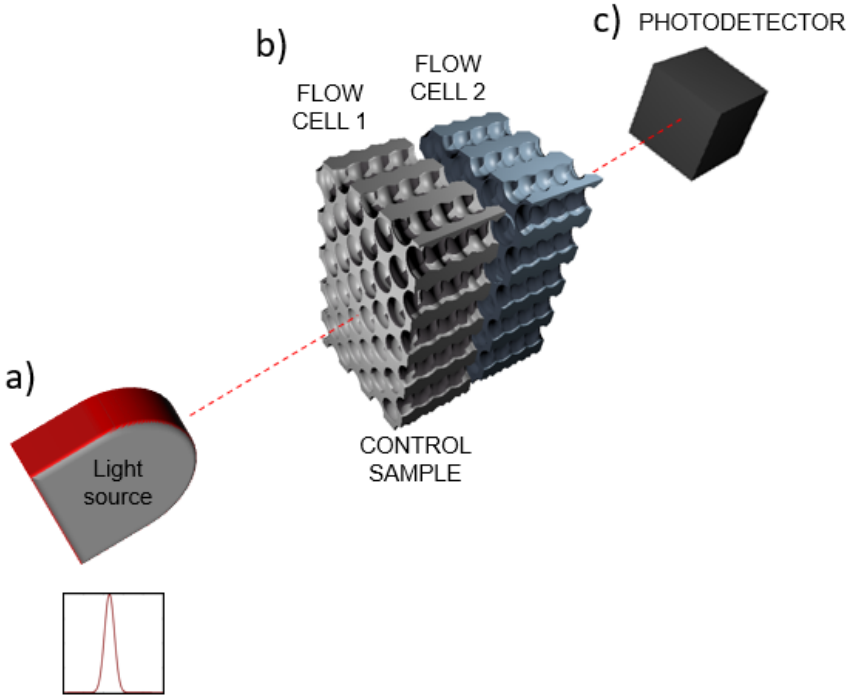

Fig. 6.15 Alternative scheme of proposed optical system for detection of analytes by NAA-RFs. (a) LED or LD light source. (b) Optical sensing platform based on NAA-RFs. The colour in the NAA-RFs distinguishes the function of each flow cell, being the flow cell 1 (grey) for the control sample and the flow cell 2 (blue) for the one that contains the analytes to detect. (c) Photodetector to monitor the final signal.

This system is formed by a narrowband emission device (such as a LED or a laser diode (LD)) as source light, a optical sensing platform based on NAA-RFs and a photodetector to monitor the final signal.

The emission spectrum of a LED or LD light source typically follows a Gaussian profile. When that light passes through a filter a significant portion of the emitted light can be reflected or absorbed resulting in a reduction in their spectral width.

Concerning the NAA-RFs structures, the transmission spectrum of a NAA-RF illuminated by white light shows the typical narrow dip corresponding to the photonic stop band. Figure 6.16 illustrates the transmission spectra for a pair of identical NAA-RFs. The picture illustrates the transmission spectra for a NAA-RF which their pores are filled with water (Flow Cell 1 or control sample), together with the transmission spectra for the another NAA-RF which their pores are filled with an aqueous solution of an analyte (Flow Cell 2 or object sample). The NAA-RFs act as a spectral filter restricting the final amount of transmitted light provided by the source

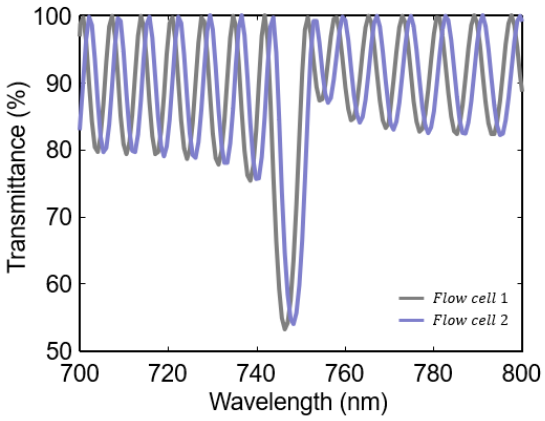

Fig. 6.16 Transmission spectra of each NAA-RFs composing the alternative proposed optical system for detection of analytes by NAA-RFs. The corresponding transmittance is specified in the legend.

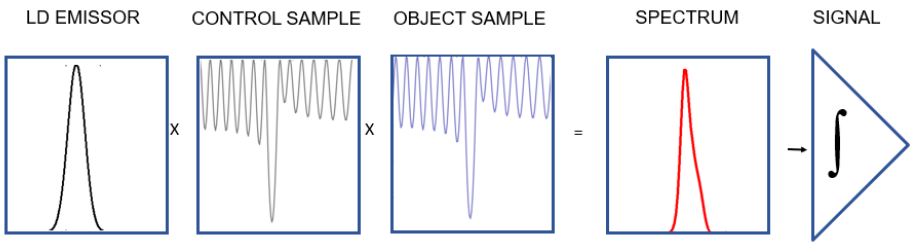

Fig. 6.17 Schematic concept view of the process of light filtering.

and the transmitted spectra of these NAA-RFs allow to calculate the amount of LD light that is capable of reaching the photodetector.

In order to assess the optical characteristics of this NAA-RF based system, reflectance spectra of the two NAA-RF that compounds the system were simulated using the numerical model described previously. The NAA-RFs were considered with the same geometrical parameters and with filling pore media that can be different such as water and an aqueous solution of an analyte, respectively. Next, the figure 6.17 illustrates the process considered to calculate the light that reaches the photodetector. The LED and LD emission spectrum and the transmission spectrum corresponding to the control and object NAA-RF samples are considered. The transmission spectrum of the NAA-RF object sample becomes modified with respect that of the control sample by alterations produced by small changes in the refractive index of the medium that fills the pores. When finally, the spectrum after the flow cell 2 is obtained, the area under it is calculated. The optical assessment is performed by calculating the changes in the area under the spectrum after the flow cell 2 produced by small changes in

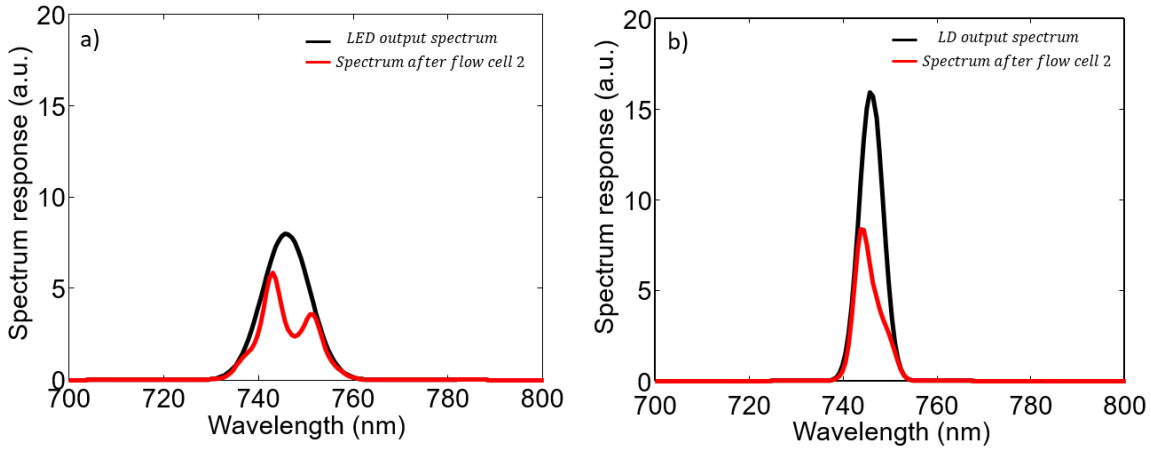

Fig. 6.18 Spectrum response before and after going through the flow cell system for a) considering a LED and b) a laser diode (LD) as a light emisor respectively. The black line represents the signal output spectrum for a light source whereas the red line represents the spectrum after going through the flow cell 2.

the refractive index of the medium that fills the pores of the NAA-RF object sample. Figure 6.18 illustrates the light signal before and after the flow cell system. The graph illustrates the spectra output for a LED (Figure 6.18.a) and a LD (Figure 6.18.b) light source (black line) together with the spectra response after going through the flow cell 2 (red line) in order to provide comparison. The figure shows a change in the typical spectral profile of the light source and a reduction of the intensity of the signal spectrum after the flow cell 2 by the signal filtering action of the NAA-RFs.

In order evaluate the possibility of using the NAA-RF system as a sensing device, reflectance spectra corresponding to the spectrum after the flow cell 2 for different refractive index values of the medium that fills the pores in the NAA-RF object sample and for each light source are calculated. Figure 6.19 shows these reflectance spectra for three different refractive index values of the pore filling medium and for different light sources in order to provide comparison. Figure 6.19.a and 6.19.b shows the spectrum calculated for $n = 1.34$ with a LED and a LD light source respectively. Similarly, figure 6.19.c and 6.19.d shows the calculated spectrum for $n = 1.35$ and for each light source, and finally 6.19.e and 6.19.f shows it for $n = 1.36$. The plots shows different spectra for each light source and for each refractive index from which could result hard to provide such comparison. However, if we consider the area closed by the signal spectrum after the flow cell 2 as the detector's signal response, this response is easily to calculate and to compare. Figure 6.20 shows the detector signal response in function of the refractive

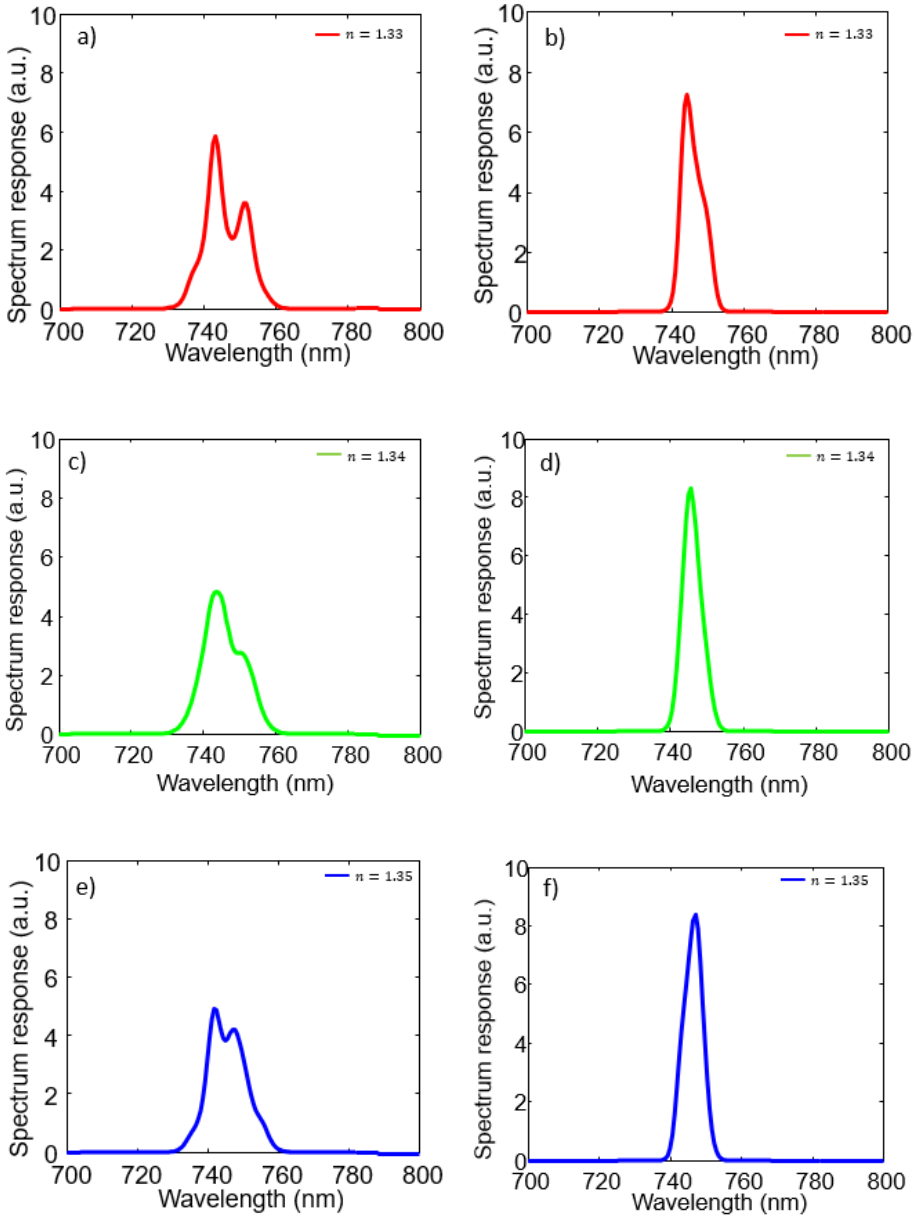

Fig. 6.19 Reflectance spectra after the flow cell system for three different refractive index values of the pore filling medium of the NAA-RF object sample (Flow Cell 2) and for two different light sources. The graphs a), c) and d) shows the spectra response when illuminating with a LED source, whereas the graphs b),d) and e) when illuminating with a LD source. Concerning the refractive index, the graphs a) and b) shows the spectra response for a $n = 1.34$, the c) and d) for $n = 1.35$ and the e) and f) $n = 1.36$.

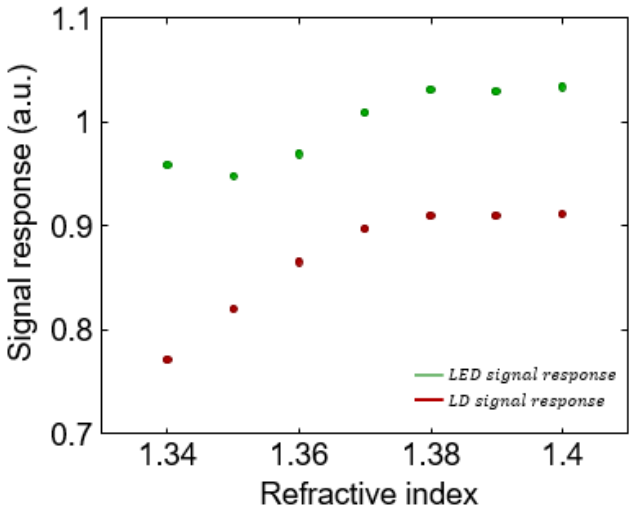

Fig. 6.20 Sensing parameter as a signal response in function of the refractive index that fills the pores.

index that fills the pores. The picture shows a increasing trend in the signal response as the refractive index increases. Therefore, such process permits establish a sensing parameter which indicates a increasing presence of analytes.

6.7 Conclusions

In this chapter, a numerical model for the optical properties of nanoporous anodic alumina-based rugate filters (NAA-RF) using transfer matrix method (TMM) with the effective medium approximation (EMA) is developed in order to study their ability in the prediction of the optical behaviour of the NAA-RFs structures. To this end, we collected reflectance measurements from real samples produced using eight different sinusoidal anodization profiles to generate eight different types of NAA-RFs. Subsequently, these real samples were simulated for each corresponding type of NAA-RF structure.

Henceforward, we considered a model in which the pore morphology shows a sinusoidal variation of the pore diameter in depth and a modulation period along the pore length. EMA is used to move from a variation of pore sizes by depth to a variation of effective refractive index based on depth. Then, this variation of effective index based on the depth is discretized obtaining a multi-layered system with constant refractive index for each layer. Reflectance spectra calculations are performed by TMM

and analysed by adjusting the geometrical parameters d_{int}, d_p, Δd_p and Δ to obtain the best fit between the experimental and the calculated reflectance.

The analysis of the computed results endorses us to conclude:

- The pore geometry of the NAA-RF induces a modification in depth of the porosity which in turn produces a modulation of the effective refractive index with the pore length. As a result of this effective refractive index oscillatory behaviour the NAA-RF reflectance spectra show photonic stop bands. The central wavelength of the PSB increases as the applied offset current (I_0) increases. By adjusting the geometrical parameters d_{int}, d_p and Δ, the numerical model developed is able to reproduce the experimental central wavelengths of these PSB. The simulations indicate an increasing trend of the pore diameter with increasing offset current, demonstrating a relationship between these two parameters.

- Experimental results indicate that the effect of the amplitude current (I_1) in the reflectance spectra of the NAA-RF results in that the central wavelength of each PSB is not affected by a variation of I_1. In contrast, a variation on the maximum reflectance is observed which increases as the I_1 increases. The numerical model developed is able to reproduce the experimental behaviour of the central wavelengths of the PSB, as well as their maximum reflectance value.

- Numerical simulations demonstrate that changes in the refractive index of the medium that fills the pores produces a shift on the central wavelength position of the photonic stop band (PSB). The shift shows a linear dependence with the refractive index of the pore filling medium, what permits to define the sensitivity as the shift of the central wavelength position of the PSB per refractive index unit. This sensitivity increases with the refractive index of the medium.

- Two conclusions from the numerical study on the effect of the pore diameter and the pore modulation amplitude on the sensitivity of NAA-RF can be extracted. From one hand, the influence of the pore diameter on the sensitivity has been demonstrated, revealing an increasing trend of the sensitivity with d_p. On the other hand, in contrast, it has been demonstrated that the pore modulation amplitude does not influence the sensitivity of the NAA-RF.

- Finally, an alternative method of sensing with NAA-RFs is proposed and evaluated. The optical characteristics of this NAA-RF based system are assessed by analysing the spectrum of the light after going through the system. The area

under the spectrum for each refractive index of the medium is compared. This process permits establish a sensing parameter by refractive index unit, showing a increasing trend in the signal response as the refractive index that fills the pores increases.

In summary, the results presented in this chapter shows the possibility to relate the fabrication parameters with the geometric characteristics of NAA-RFs. The numerical model of NAA-RF developed based on the effective medium approximation and the transfer matrix method is capable to determine crucial geometrical parameters such as average pore diameter, (d_p), and the pore modulation amplitude, Δd_p. These results could be important when designing further nanostructures and simulating and predicting their behaviour in future applications.

Chapter 7

Summary and conclusions

Computational models enable scientists to achieve a better understanding of a specific research field, to develop a particular technology understanding the underlying mechanism and to predict results without the need to use authentic devices. Theoretical study on the optical properties of materials is a fundamental field of research. In particular, the study of the optical properties of nanoporous anodic alumina (NAA) by means of numerical modelling permits to understand their relationship with the structural features of the NAA, providing a conceptual framework for the analysis of their optical behaviour. Additionally, these simulations are a powerful tool for the improvement of the NAA-based devices with a design fundamented on a wider knowledge basis.

Of the several models existing in the literature to predict the optical behaviour of NAA-based devices, there is a scarcity of published studies on NAA optical modelling in a broad range of structural features. In this thesis, we aimed at covering this existing gap with the development of predictive models for the optical properties of NAA valid in a wide range of geometrical characteristics.

The objectives of this Thesis have been:

- To develop computer implementations of numerical models for the theoretical study of the optical behaviour of NAA with a broad range of geometric and optical characteristics.
- To analyse the structural and the optical properties of the NAA in order to perform the modelling considering it as a one-dimensional and a two-dimensional photonic crystal.
- To study theoretically of the optical behaviour of gold-coated NAA as a proposal of application to sensing devices based on NAA.

- To study theoretically of the optical behaviour of NAA graded-index structures as a proposal of modelling tools applied to more complex structures, and a theoretical study and assessment of an alternative proposal of sensing with NAA-based graded-index structures.

The study of the optical behaviour of photonic structures based on NAA can not be addressed using a single numerical method due to the different types of structures to be considered. Therefore, the chosen had been restricted to the transfer matrix method (TMM) and the finite differences in the time domain method (FDTD). The fundamentals of these numerical methods have been described in Chapter 3.

In Chapter 4, a numerical procedure based on 3D-FDTD was applied to simulate the optical behaviour of the NAA structures with a wide range of interpore distances has been developed. The study has been addressed for two types of NAA structures with different interpore distances (produced with oxalic and with phosphoric electrolytes). Reflectance measurements from real samples were collected and subsequently simulated considering various models of increasing geometric and chemical complexity: i) an initial model that considers the flat aluminium-alumina and alumina-air interfaces, ii) a second that considers the interface between the aluminium substrate and the alumina layer texturized with the hemispherical concavities caused by the preparation procedures, as well as the alumina barrier layer and the top surface of the alumina layer, iii) a third model that considers a anionic layer in the outer pore wall layer with distinct optical properties and iv) a last fourth model which contemplates absorption in the anionic layer.

The most significant findings to emerge from this study are:

- The EMA-TMM and FDTD correctly reproduce the optical behaviour for short interpore distance NAA.

- When the NAA geometric parameters are of the order of the wavelength of the incident light, EMA is no longer adequate and FDTD offers a better alternative to deal with the geometrical features of the structures. However, FDTD also fails in the prediction of some features in the visible range for long interpore distances NAA.

- The incorporation of the interfaces texturization with FDTD is crucial in order to have precise predictions of the optical behaviour of the NAA for a wide range of characteristics parameters.

- In addition, the consideration of the dual structure of the pore walls with different optical properties (with or without absorption) in their outer pore wall, is translated into the introduction of a next-to-leading order in the predictions, even though it allows a slight adjustment with the experimental measurements.

In Chapter 5, a study on the capabilities of gold-coated NAA membranes as reflectometry-based plasmonic platforms for biosensors has been made. This study has been performed by a 3D-FDTD numerical simulation of the reflectance spectrum of the gold-coated NAA membranes upon the attachment of analytes (biolayer) on the gold coating and the inner pore walls.

The principal theoretical implications of this chapter are:

- Numerical simulations have demonstrated that the nanostructuring provided by the pore distribution of the NAA membranes permits a direct coupling of the incident light with the plasmons on the metal. That coupling depends strongly on the interpore distance NAA membranes, being much more efficient for long interpore distances gold-coated NAA membranes.

- Furthermore, the simulations have demonstrated that the attachment of a biolayer on the gold coating and on the inner pore walls produces a shift on the resonant wavelength of the plasmon resonance. The shift shows a linear dependence with the refractive index of the biolayer, what permits to define the sensitivity as the shift of the resonant wavelength per refractive index unit. This sensitivity increases with the thickness of the biolayer.

- Additionally, the sensitivity function can be optimized for a specific gold thin film layer and a specific analyte to detect. The sensitivity decreases as the thickness of the gold thin film on the NAA increases.

- In order to implement this gold-coated NAA membrane as a biosensor, both the resonance Q-factor and the sensitivity have to be taken into account. The resonance Q-factor increases as the gold thin film increases. Therefore, an increase in sensitivity has the disadvantage of a decrease in the resonance Q-factor, which can reduce the resolution in the measurement of the shift under experimental conditions. This suggests that an optimal thickness of the gold coating has to be determined for each specific experimental condition.

Finally, in Chapter 6 the optical response of NAA-based rugate filters has been modelled with a numerical procedure based on the TMM with an EMA. The study

has been addressed for eight different types of NAA-RFs. Reflectance measurements from these real sample were collected and simulated considering a model in which the pore morphology shows a sinusoidal variation of the pore diameter in depth and a modulation period along the pore length. By means of EMA a multi-layered system with constant refractive index for each layer has been created. Reflectance spectra calculations are performed using the TMM and analysed by adjusting the geometrical parameters in order to obtain the best fit between the experimental and the calculated reflectance. The results presented in this chapter show the possibility to relate the fabrication parameters with the geometric characteristics of NAA-RFs.

The investigation carried out in this chapter has shown that:

- The numerical model developed is able to reproduce the experimental reflectance spectra of the NAA-RFs. The central wavelength of the photonic stop band increases as the applied offset current increases. The simulations indicate an increasing trend of the pore diameter with increasing the offset current, demonstrating a relationship between these two parameters

- The numerical model developed is also able to reproduce the effect of the amplitude current in the experimental reflectance spectra of the NAA-RFs. An increase on the maximum reflectance of the photonic stop band is observed as the amplitude current increases. Instead, the central wavelength of each photonic stop band is not affected by a variation of the amplitude current.

- Furthermore, numerical simulations demonstrate that changes in the refractive index of the medium that fills the pores produces a shift on the central wavelength position of the photonic stop band. The shift shows a linear dependence with the refractive index of the pore filling medium, which permits to define the sensitivity as the shift of the central wavelength position of the photonic stop band per refractive index unit.

- The average pore diameter influences the sensitivity of NAA-RFs. The sensitivity increases as the average pore diameter increases. On the other hand, however, it has been demonstrated that sensitivity is not influenced the pore modulation amplitude.

- On the basis of the properties of the photonic stop band of NAA-RFs, an alternative sensing method has been proposed. The method is based on the use of two equal NAA-RF's as filters for the ligth emitted from a narrowband source (LED or laser diode) centred at the same wavelength as the NAA-RF's. Light

from the source is made to transmit through the two NAA-RF's consecutively. One of the NAA-RF's is filled with a reference medium while the second is filled with the same medium with the dissolved analyte to be detected. The resulting relative shift of the corresponding PSBs results in a change in signal in a photodetector placed after the two NAA-RF's. The possibilities of such a system have been investigated.

UNIVERSITAT ROVIRA I VIRGILI
NUMERICAL MODELLING OF NANOPOROUS ANODIC ALUMINA PHOTONIC STRUCTURES FOR OPTICAL BIOSENSING
Francisco Bertó Roselló

References

[Abdulhalim2014] Ibrahim Abdulhalim. Plasmonic sensing using metallic nanosculptured thin films. *Small*, 10(17):3499–3514, 2014. ISSN 16136829. doi:10.1002/smll.201303181.

[Alekseev2007] S. A. Alekseev, V. Lysenko, V. N. Zaitsev, and D. Barbier. Application of infrared interferometry for quantitative analysis of chemical groups grafted onto the internal surface of porous silicon nanostructures. *J. Phys. Chem. C*, 111(42):15217–15222, 2007. ISSN 19327447. doi:10.1021/jp0712452.

[Alvarez2009] Sara D Alvarez, Chang-peng Li, Casey E Chiang, Ivan K Schuller, and Michael J Sailor. A Label-Free Porous Alumina Interferometric Immunosensor. *ACS Nano*, 3(10):3301–3307, 2009.

[Andonegui2013] Imanol Andonegui and Angel J. Garcia-Adeva. The finite element method applied to the study of two-dimensional photonic crystals. 21(4):173–190, 2013. ISSN 1094-4087. doi:10.1364/OE.21.004072.

[Anglin2008] Emily J. Anglin, Lingyun Cheng, William R. Freeman, and Michael J. Sailor. Porous silicon in drug delivery devices and materials. *Adv. Drug Deliv. Rev.*, 60(11):1266–1277, 2008. ISSN 0169409X. doi:10.1016/j.addr.2008.03.017.

[Anglin2004] Emily J. Anglin, Michael P. Schwartz, Valerie P. Ng, Loren a. Perelman, and Michael J. Sailor. Engineering the chemistry and nanostructure of porous silicon fabry-pérot films for loading and release of a steroid. *Langmuir*, 20(25):11264–11269, 2004. ISSN 07437463. doi:10.1021/la048105t.

[Anker2008] Jeffrey N. Anker, W. Paige Hall, Olga Lyandres, Nilam C. Shah, Jing Zhao, and Richard P. Van Duyne. Biosensing with plasmonic nanosensors. *Nat. Mater.*, 7(6):442–453, 2008. ISSN 14761122. doi:10.1038/nmat2162.

[Aryal2008] Mukti Aryal, Fatih Buyukserin, Kamil Mielczarek, Xiao-Mei Zhao, Jinming Gao, Anvar Zakhidov, and Wenchuang (Walter) Hu. Imprinted large-scale high density polymer nanopillars for organic solar cells. *J. Vac. Sci. Technol. B Microelectron.*

Nanom. Struct., 26(6):2562–2566, 2008. ISSN 1071-1023. doi: 10.1116/1.2981076.

[Atwater2010] Harry A. Atwater and Albert Polman. Plasmonics for improved photovoltaic devices. *Nat. Mater.*, 9(10):865–865, 2010. ISSN 1476-1122. doi:10.1038/nmat2866.

[Balderrama2015] Victor S. Balderrama, Josep Albero, Pedro Granero, Josep Ferré-Borrull, Josep Pallarés, Emilio Palomares, and Lluis F. Marsal. Design, fabrication and charge recombination analysis of an interdigitated heterojunction nanomorphology in P3HT/PC ₇₀ BM solar cells. *Nanoscale*, 7(33):13848–13859, 2015. ISSN 2040-3364. doi:10.1039/C5NR02429C.

[Baranowska2014] Malgorzata Baranowska, Agata J. Slota, Pinkie J. Eravuchira, Gerard Macias, Elisabet Xifré-Pérez, Josep Pallares, Josep Ferré-Borrull, and Lluís F. Marsal. Protein attachment to nanoporous anodic alumina for biotechnological applications: Influence of pore size, protein size and functionalization path. *Colloids Surfaces B Biointerfaces*, 122:375–383, 2014. ISSN 18734367. doi:10.1016/j.colsurfb.2014.07.027.

[Bartzsch2004] H Bartzsch, S Lange, P Frach, and K Goedicke. Graded refractive index layer systems for antireflective coatings and rugate filters deposited by reactive pulse magnetron sputtering. *Surface and Coatings Technology.*, 181:616–620, 2004. doi: 10.1016/j.surfcoat.2003.10.105.

[Berenger1996] Jean-Pierre Bérenger. A Perfectly Matched Layer For The Absorption Of Electromagnetic Waves. *J. Comput. Phys.*, 127:363–379, 1996.

[Berto-Rosello2018] Francesc Bertó-Roselló, Elisabet Xifré-Pérez, Josep Ferré-Borrull, and Lluis F. Marsal. 3D-FDTD Modelling of Optical Biosensing based on Gold-Coated Nanoporous Anodic Alumina. *Results in Physics.*, 2018, Accepted (in press). doi: 10.1016/j.rinp.2018.10.067.

[Berto-Rosello2016] Francesc Bertó-Roselló, Elisabet Xifré-Pérez, Josep Ferré-Borrull, Josep Pallarès, and Lluis F. Marsal. Nanoporous Anodic Alumina 3D FDTD Modelling for a Broad Range of Inter-pore Distances. *Nanoscale Res. Lett.*, 11(1):359, 2016. ISSN 1556276X. doi:10.1186/s11671-016-1575-6.

[Block2005] Ian D. Block, Leo L. Chan, and Brian T. Cunningham. Photonic crystal optical biosensor incorporating structured low-index porous dielectric. *Proc. IEEE Sensors*, 2005:742–745, 2005. ISSN 09254005. doi:10.1109/ICSENS.2005.1597806.

[M.Born1999] M. Born and E. Wolf. *Principles of Optics*. Cambridge University Press, Cambridge, 7th edition, 1999.

[Bosch2001] S. Bosch, J. Ferré-Borrull, and J. Sancho-Parramon. A general-purpose software for optical characterization of thin films: Specific features for microelectronic applications. *Solid. State. Electron.*, 45:703–709, 2001. ISSN 00381101. doi:10.1016/S0038-1101(01)00092-2.

[Bosch2000] Salvador Bosch, Josep Ferré-Borrull, Norbert Leinfellner, and Adolf Canillas. Effective dielectric function of mixtures of three or more materials: a numerical procedure for computations. *Surf. Sci.*, 453(1-3):9–17, 2000. ISSN 00396028. doi:10.1016/S0039-6028(00)00354-X.

[Cantelli2016] L. Cantelli, J. S. Santos, and F. Trivinho-Strixino. The effect of anodization temperature on optical properties of nanoporous anodic alumina (NAA) films. *J. Electroanal. Chem.*, 780:386–390, 2016. ISSN 15726657. doi:10.1016/j.jelechem.2016.01.009.

[Cetin2015] Arif E. Cetin, Dordaneh Etezadi, Betty C. Galarreta, Mickael P. Busson, Yasa Eksioglu, and Hatice Altug. Plasmonic Nanohole Arrays on a Robust Hybrid Substrate for Highly Sensitive Label-Free Biosensing. *ACS Photonics*, 2(8):1167–1174, 2015. ISSN 23304022. doi:10.1021/acsphotonics.5b00242.

[Chen2016] Fang Chen and Huafeng Zhang. Absorption property and nanosensing via double metal films with rectangle holes array. *Opt. Commun.*, 379:13–18, 2016. ISSN 00304018. doi:10.1016/j.optcom.2016.05.046.

[Chen2015] Yuting Chen, Abel Santos, Ye Wang, Tushar Kumeria, Junsheng Li, Changhai Wang, and Dusan Losic. Biomimetic Nanoporous Anodic Alumina Distributed Bragg Reflectors in the Form of Films and Microsized Particles for Sensing Applications. *ACS Appl. Mater. Interfaces*, 7(35):19816–19824, 2015. ISSN 19448252. doi:10.1021/acsami.5b05904.

[Chu2006] S. Z. Chu, K. Wada, S. Inoue, M. Isogai, Y. Katsuta, and A. Yasumori. Large-Scale Fabrication of Ordered Nanoporous Alumina Films with Arbitrary Pore Intervals by Critical-Potential Anodization. *J. Electrochem. Soc.*, 153(9):B384, 2006. ISSN 00134651. doi:10.1149/1.2218822.

[Cos2011] Joaquín Cos. *Design and modelling of photonic crystals with anisotropic components*. Ph.D. thesis, Universitat Rovira i Virgili, 2011.

[D.A.G.Bruggeman] D. A. G. Bruggeman. Berechnung Verschiedener Physikalischer Konstanten von Heterogenen Substanzen. I. Dielektrizitatskonstanten und Leitfahigkeiten der Mischkorper aus Isotropen Substanzen. *Ann. Phys.*, 24((Leipzig)):636–679, 1935.

[Damm2014] Signe Damm, Frances Lordan, Antony Murphy, Mark McMillen, Robert Pollard, and James H. Rice. Application of AAO Matrix in Aligned Gold Nanorod Array Substrates for Surface-Enhanced Fluorescence and Raman Scattering. *Plasmonics*, 9(6):1371–1376, 2014. ISSN 15571963. doi:10.1007/s11468-014-9751-y.

[Deubel2005] M. Deubel, M. Wegener, S. Linden, and G. Von Freymann. Angle-resolved transmission spectroscopy of three-dimensional photonic crystals fabricated by direct laser writing. *Appl. Phys. Lett.*, 87(22):1–3, 2005. ISSN 00036951. doi:10.1063/1.2137899.

[Deubel2004] Markus Deubel, Georg Von Freymann, Martin Wegener, Suresh Pereira, Kurt Busch, and Costas M. Soukoulis. Direct laser writing of three-dimensional photonic-crystal templates for telecommunications. *Nat. Mater.*, 3(7):444–447, 2004. ISSN 14761122. doi:10.1038/nmat1155.

[Dragoman2008] M. Dragoman and D. Dragoman. Plasmonics: Applications to nanoscale terahertz and optical devices. *Prog. Quantum Electron.*, 32(1):1–41, 2008. ISSN 00796727. doi:10.1016/j.pquantelec.2007.11.001.

[Ferre-Borrull2014] Josep Ferré-Borrull, Josep Pallarès, Gerard Macías, and Lluis F. Marsal. Nanostructural engineering of nanoporous anodic alumina for biosensing applications. *Materials (Basel).*, 7(7):5225–5253, 2014. ISSN 19961944. doi:10.3390/ma7075225.

[Ferre-Borrull2014a] Josep Ferré-Borrull, Mohammad Rahman, Josep Pallarès, and Lluís F Marsal. Tuning nanoporous anodic alumina distributed-Bragg reflectors with the number of anodization cycles and the anodization temperature. *Nanoscale Res. Lett.*, 9(1):416, 2014. ISSN 1556-276X. doi:10.1186/1556-276X-9-416.

[Ferre-Borrull2015] L.F. Ferre-Borrull, J., Xifre-Perez, E., Pallares, J., Marsal. Optical properties of nanoporous anodic alumina and derived applications. In *Nanoporous Alumina Springer Ser. Mater. Sci.*, volume 219, pages 185–217. 2015. doi:10.1007/978-3-319-20334-8_6.

[Fu2014] Cuicui Fu, Yuejiao Gu, Zhiyong Wu, Yuyang Wang, Shuping Xu, and Weiqing Xu. Surface-enhanced Raman scattering (SERS) biosensing based on nanoporous dielectric waveguide resonance. *Sensors Actuators, B Chem.*, 201:173–176, 2014. ISSN 09254005. doi:10.1016/j.snb.2014.04.091.

[GopalKhan2013] Gobinda Gopal Khan, Ashutosh K. Singh, and Kalyan Mandal. Structure dependent photoluminescence of nanoporous amorphous anodic aluminium oxide membranes: Role of F+center defects. *J. Lumin.*, 134:772–777, 2013. ISSN 00222313. doi:10.1016/j.jlumin.2012.06.050.

[Gordon2008] Reuven Gordon, David Sinton, Karen L. Kavanagh, and Alexandre G. Brolo. A new generation of sensors based on extraordinary optical transmission. *Acc. Chem. Res.*, 41(8):1049–1057, 2008. ISSN 00014842. doi:10.1021/ar800074d.

[Gray2012] Stephen K Gray. Theory and Modeling of Plasmonic Structures Theory and Modeling of Plasmonic Structures. 2012. doi: 10.1021/jp309664c.

[Gultepe2010] Evin Gultepe, Dattatri Nagesha, Srinivas Sridhar, and Mansoor Amiji. Nanoporous inorganic membranes or coatings for sustained drug delivery in implantable devices. *Adv. Drug Deliv. Rev.*, 62(3):305–315, 2010. ISSN 0169409X. doi: 10.1016/j.addr.2009.11.003.

[Gyurcsanyi2008] Róbert E. Gyurcsányi. Chemically-modified nanopores for sensing. *TrAC - Trends Anal. Chem.*, 27(7):627–639, 2008. ISSN 01659936. doi:10.1016/j.trac.2008.06.002.

[Han2014] Katherine Han and Chih-Hung Chang. Numerical Modeling of Sub-Wavelength Anti-Reflective Structures for Solar Module Applications. *Nanomaterials*, 4(1):87–128, 2014. ISSN 2079-4991. doi:10.3390/nano4010087.

[Hernandez-Eguia2014] Laura P Hernández-Eguía, Josep Ferré-Borrull, Gerard Macias, Josep Pallarès, and Lluís F Marsal. Engineering optical properties of gold-coated nanoporous anodic alumina for biosensing. *Nanoscale Res. Lett.*, 9(1):414, 2014. ISSN 1931-7573. doi: 10.1186/1556-276X-9-414.

[hillebrand2008] Reinald Hillebrand, Frank Mu, Kathrin Schwirn, Woo Lee, and Martin Steinhart. Quantitative Analysis of the Grain Hexagonal Lattices. 2(5):913–920, 2008.

[Homola2008] Jirí Homola and Jirí Homola. Surface plasmon resonance sensors for detection of chemical and biological species. *Chem. Rev.*, 108(2):462–93, 2008. ISSN 0009-2665. doi:10.1021/cr068107d.

[Hotta2012] Kazuhiro Hotta, Akira Yamaguchi, and Norio Teramae. Nanoporous waveguide sensor with optimized nanoarchitectures for highly sensitive label-free biosensing. *ACS Nano*, 6(2):1541–1547, 2012. ISSN 19360851. doi:10.1021/nn204494z.

[Huang2003] G. S. Huang, X. L. Wu, Y. F. Mei, X. F. Shao, and G. G. Siu. Strong blue emission from anodic alumina membranes with ordered nanopore array. *J. Appl. Phys.*, 93(1):582–585, 2003. ISSN 00218979. doi:10.1063/1.1529075.

[Huang2008] Mao Jung Huang, Chii Rong Yang, Yuang Cherng Chiou, and Rong Tsong Lee. Fabrication of nanoporous antireflection surfaces on silicon. *Sol. Energy Mater. Sol. Cells*, 92(11):1352–1357, 2008. ISSN 09270248. doi:10.1016/j.solmat.2008.05.014.

[Ingham2012] Colin J. Ingham, Jurjen ter Maat, and Willem M. de Vos. Where bio meets nano: The many uses for nanoporous aluminum oxide in biotechnology. *Biotechnol. Adv.*, 30(5):1089–1099, 2012. ISSN 07349750. doi:10.1016/j.biotechadv.2011.08.005.

[Jain2008] Prashant K Jain, Xiaohua Huang, Ivan H El-sayed, and Mostafa A El-sayed. Noble Metals on the Nanoscale : Optical and Photothermal Properties and Some Applications in Imaging , Sensing , Biology , and Medicine. 41(12):7–9, 2008.

[Joannopoulos2011] J. D. Joannopoulos, Steven G Johnson, J. N. Winn, and R. D. Meade. *Photonic Crystals - Molding the Flow of Light*. Princeton University Press, Princeton, 2nd edition, 2008.

[Kee2012] Jack Sheng Kee, Sweeyin Lim, Agampodi Promoda Perera, Mi Kyoung Park, and Yong Zhang. Plasmonic nanohole array for biosensor applications. *2012 Photonics Glob. Conf. PGC 2012*, pages 1–4, 2012. doi:10.1109/PGC.2012.6458037.

[Kim2008] Do Kyun Kim, Kagan Kerman, Ha Minh Hiep, Masato Saito, Shohei Yamamura, Yuzuru Takamura, Young Soo Kwon, and Eiichi Tamiya. Label-free optical detection of aptamer-protein interactions using gold-capped oxide nanostructures. *Anal. Biochem.*, 379(1):1–7, 2008. ISSN 00032697. doi:10.1016/j.ab.2008.04.029.

[Kim2017] Do-Kyun Kim, Dong Min Kim, Seung Min Yoo, and Sang Yup Lee. Controllable gold-capped nanoporous anodic alumina chip for label-free, specific detection of bacterial cells. *RSC Adv.*, 7(30):18815–18820, 2017. ISSN 2046-2069. doi:10.1039/C6RA27130H.

[Konig2014] Tobias König, Rajesh Kodiyath, Zachary A. Combs, Mahmoud A. Mahmoud, Mostafa A. El-Sayed, and Vladimir V. Tsukruk. Silver nanocube aggregates in cylindrical pores for higher refractive index plasmonic sensing. *Part. Part. Syst. Charact.*, 31(2):274–283, 2014. ISSN 09340866. doi:10.1002/ppsc.201300217.

[Koutsioubas2008] Alexandros G. Koutsioubas, Nikolaos Spiliopoulos, Dimitris Anastassopoulos, Alexandros A. Vradis, and George D. Priftis. Nanoporous alumina enhanced surface plasmon resonance sensors. *J. Appl. Phys.*, 103(9), 2008. ISSN 00218979. doi:10.1063/1.2924436.

[Kral2009] Zdeněk Král, Lukáš Vojkůvka, Enric Garcia-Caurel, Josep Ferré-Borrull, Lluis F. Marsal, and Josep Pallarès. Calculation of Angular-Dependent Reflectance and Polarimetry Spectra of Nanoporous Anodic Alumina-Based Photonic Crystal Slabs. *Photonics Nanostructures - Fundam. Appl.*, 7(1):12–18, 2009. ISSN 15694410. doi:10.1016/j.photonics.2008.11.005.

[Kumeria2012a] Tushar Kumeria, Mahaveer D. Kurkuri, Kerrilyn R. Diener, Luke Parkinson, and Dusan Losic. Label-free reflectometric interference microchip biosensor based on nanoporous alumina for detection of circulating tumour cells. *Biosens. Bioelectron.*, 35(1):167–173, 2012. ISSN 09565663. doi:10.1016/j.bios.2012.02.038.

[Kumeria2012] Tushar Kumeria and Dusan Losic. Controlling interferometric properties of nanoporous anodic aluminium oxide. *Nanoscale Res. Lett.*, 7(1):88, 2012. ISSN 1556-276X. doi:10.1186/1556-276X-7-88.

[Kumeria2011a] Tushar Kumeria, Luke Parkinson, and Dusan Losic. A nanoporous interferometric micro-sensor for biomedical detection of volatile sulphur compounds. *Nanoscale Res. Lett.*, 6(1):634, 2011. ISSN 1556-276X. doi:10.1186/1556-276X-6-634.

[Kumeria2014] Tushar Kumeria, Mohammad Mahbubur Rahman, Abel Santos, Josep Ferré-Borrull, Lluís F. Marsal, and Dusan Losic. Structural and optical nanoengineering of nanoporous anodic alumina rugate filters for real-time and label-free biosensing applications. *Anal. Chem.*, 86(3):1837–1844, 2014. ISSN 00032700. doi:10.1021/ac500069f.

[Kumeria2014a] Tushar Kumeria, Abel Santos, and Dusan Losic. Nanoporous anodic alumina platforms: engineered surface chemistry and structure for optical sensing applications. *Sensors (Basel).*, 14(7):11878–1918, 2014. ISSN 1424-8220. doi:10.3390/s140711878.

[Kumeria2014b] Tushar Kumeria, Abel Santos, Mohammad Mahbubur Rahman, Josep Ferré-Borrull, Lluís F. Marsal, and Dusan Losic. Advanced Structural Engineering of Nanoporous Photonic Structures: Tailoring Nanopore Architecture to Enhance Sensing Properties. *ACS Photonics*, 1(12):1298–1306, 2014. ISSN 23304022. doi:10.1021/ph500316u.

[Laatar2017] Fakher Laatar, Afef Harizi, Ahmed Zarroug, Mondher Ghrib, Mohamed Hassen, Mounir Gaidi, and Hatem Ezzaouia. Novel CdSe nanorods/porous anodic alumina nanocomposite-based ethanol sensor: sensitivity enhancement by visible light illumination. *J. Mater. Sci. Mater. Electron.*, 28(16):12259–12267, 2017. ISSN 1573482X. doi:10.1007/s10854-017-7042-z.

[Lau2004] K H A Lau, L S Tan, K Tamada, M S Sander, and W Knoll. Highly sensitive detection of processes occurring inside nanoporous anodic alumina templates: A waveguide optical study. *J. Phys. Chem. B*, 108(30):10812–10818, 2004. ISSN 1520-6106. doi:10.1021/jp0498567.

[Lee2011] Seung Woo Lee, Kyeong Seok Lee, Junhyoung Ahn, Jae Jong Lee, Min Gon Kim, and Yong Beom Shin. Highly sensitive biosensing using arrays of plasmonic Au nanodisks realized by nanoimprint lithography. *ACS Nano*, 5(2):897–904, 2011. ISSN 19360851. doi:10.1021/nn102041m.

[Lee2006a] Woo Lee, Ran Ji, Ulrich Gösele, and Kornelius Nielsch. Fast fabrication of long-range ordered porous alumina membranes by hard anodization. *Nat. Mater.*, 5(9):741–747, 2006. ISSN 1476-1122. doi:10.1038/nmat1717.

[Lee2014] Woo Lee and Sang-Joon Park. Porous Anodic Aluminum Oxide: Anodization and Templated Synthesis of Functional Nanostructures. *Chem. Rev.*, 114:7487–7556, 2014. ISSN 1520-6890. doi:10.1021/cr500002z.

[Lee2008a] Woo Lee, Roland Scholz, and Ulrich Gösele. A Continuous Process for Structurally Well-Defined Al 2 O 3 Nanotubes Based on Pulse Anodization of Aluminum. *Nano Lett.*, 8(8):2155–2160, 2008. ISSN 1530-6984. doi:10.1021/nl080280x.

[Lee2008] Woo Lee, Kathrin Schwirn, Martin Steinhart, Eckhard Pippel, Roland Scholz, and Ulrich Gösele. Structural engineering of nanoporous anodic aluminium oxide by pulse anodization of aluminium. *Nat. Nanotechnol.*, 3(4):234–239, 2008. ISSN 17483395. doi:10.1038/nnano.2008.54.

[LeifJ.Sherry2005] Leif J. Sherry, Shih-Hui Chang, George C. Schatz, Benjamin J. Wiley Duyne, Richard P. Van, and Younan Xia. Localized Surface Plasmon Resonance Spectroscopy of Single Silver Nanocubes. *Nano Lett.*, 5(10):2014–2038, 2005. doi: 10.1021/NL0515753.

[Li1998] Feiyue Li, Lan Zhang, and Robert M Metzger. On the Growth of Highly Ordered Pores in Anodized Aluminum Oxide. *Chem. Mater*, 10(28):2470–2480, 1998.

[Li2014] Jiawen Li, Zhiqiang Zhu, Yanlei Hu, Jinjin Zheng, Jiaru Chu, and Wenhao Huang. Numerical and experimental study of the structural color by widening the pore size of nanoporous anodic alumina. *J. Nanomater.*, 2014, 2014. ISSN 16874129. doi:10.1155/2014/819432.

[Li2007a] Zhaojian J. Li and Kelong L. Huang. Optical properties of alumina membranes prepared by anodic oxidation process. *J.*

Lumin., 127(2):435–440, 2007. ISSN 00222313. doi:10.1016/j.jlumin.2007.02.001.

[Lin1997] V S Lin, K Motesharei, K P Dancil, M J Sailor, and M R Ghadiri. A porous silicon-based optical interferometric biosensor. *Science*, 278(5339):840–843, 1997. ISSN 00368075. doi:10.1126/science.278.5339.840.

[Losic2009a] Dusan Losic, Mickael Lillo, and Dusan Losic Jr. Porous Alumina with shaped pore geometries and complex pore architectures fabricated by cyclic anodization. *Small*, 5(12):1392–1397, 2009. ISSN 16136810. doi:10.1002/smll.200801645.

[Losic2009] Dusan Losic and Spomenka Simovic. Self-ordered nanopore and nanotube platforms for drug delivery applications. *Expert Opin. Drug Deliv.*, 6(12):1363–1381, 2009. ISSN 1742-5247. doi:10.1517/17425240903300857.

[Lumerical] Lumerical. Lumerical Inc. *https://www.lumerical.com/tcad-products/fdtd/*.

[Macias2014] Gerard Macias, Josep Ferré-Borrull, Josep Pallarès, and Lluís F. Marsal. 1-D nanoporous anodic alumina rugate filters by means of small current variations for real-time sensing applications. *Nanoscale Res. Lett.*, 9(1):1–6, 2014. ISSN 1556276X. doi:10.1186/1556-276X-9-315.

[Macias2013] Gerard Macias, Laura P. Hernández-Eguía, Josep Ferré-Borrull, Josep Pallares, and Lluís F. Marsal. Gold-coated ordered nanoporous anodic alumina bilayers for future label-free interferometric biosensors. *ACS Appl. Mater. Interfaces*, 5(16):8093–8098, 2013. ISSN 19448244. doi:10.1021/am4020814.

[Maier2001] S. A. Maier, M. L. Brongersma, P. G. Kik, S. Meltzer, A. A G Requicha, and H. A. Atwater. Plasmonics - A route to nanoscale optical devices. *Adv. Mater.*, 13(19):1501–1505, 2001. ISSN 09359648. doi:10.1002/1521-4095(200110)13:19<1501::AID-ADMA1501>3.0.CO;2-Z.

[Maniya2014a] Nalin H. Maniya, Sanjaykumar R. Patel, and Z. V.P. Murthy. Simulation and fabrication study of porous silicon photonic crystal. *Optik (Stuttg).*, 125(2):828–831, 2014. ISSN 00304026. doi:10.1016/j.ijleo.2013.07.062.

[Marinakos2007] Stella M. Marinakos, Sihai Chen, and Ashutosh Chilkoti. Plasmonic detection of a model analyte in serum by a gold nanorod sensor. *Anal. Chem.*, 79(14):5278–5283, 2007. ISSN 00032700. doi:10.1021/ac0706527.

[Markel2016] Vadim A. Markel. Introduction to the Maxwell Garnett approximation: tutorial. *J. Opt. Soc. Am. A*, 33(7):1244, 2016. ISSN 1084-7529. doi:10.1364/JOSAA.33.001244.

[Marsal2009] L. F. Marsal, L. Vojkuvka, P. Formentin, J. Pallarés, and J. Ferré-Borrull. Fabrication and optical characterization of nanoporous alumina films annealed at different temperatures. *Opt. Mater. (Amst).*, 31(6):860–864, 2009. ISSN 09253467. doi:10.1016/j.optmat.2008.09.008.

[Martin-Moreno2001] L. Martín-Moreno, F. J. García-Vidal, H. J. Lezec, K. M. Pellerin, T. Thio, J. B. Pendry, and T. W. Ebbesen. Theory of extraordinary optical transmission through subwavelength hole arrays. *Phys. Rev. Lett.*, 86(6):1114–1117, 2001. ISSN 00319007. doi:10.1103/PhysRevLett.86.1114.

[Masuda1995] H Masuda and K. Fukuda. Ordered metal nanohole arrays made by a two-step replication of honeycomb structures of Anodic Alumina. *Science (80-.).*, 268:1466–1468, 1995.

[Masuda1997] Hideki Masuda and Fumio Hasegwa. Self-Ordering of Cell Arrangement of Anodic Porous Alumina Formed in Sulfuric Acid Solution. *J. Electrochem. Soc.*, 144(5):L127, 1997. ISSN 00134651. doi:10.1149/1.1837634.

[Mirotznik2010] Mark S. Mirotznik, Brandon L. Good, Paul Ransom, David Wikner, and Joseph N. Mait. Broadband antireflective properties of inverse motheye surfaces. *IEEE Trans. Antennas Propag.*, 58(9):2969–2980, 2010. ISSN 0018926X. doi: 10.1109/TAP.2010.2052575.

[Moharam1995] T.K. Moharam, M.G., Grann, E.B., Pommet, D.A., Gaylord. Formulation for stable and efficient implementation of the rigorous coupled-wave analysis of binary gratings. *J. Opt. Soc. Am. A Opt. Image Sci. Vis.*, 12(5):1068–1076, 1995.

[Mondal2010] B. Mondal and S. K. Saha. Fabrication of SERS substrate using nanoporous anodic alumina template decorated by silver nanoparticles. *Chem. Phys. Lett.*, 497(1-3):89–93, 2010. ISSN 00092614. doi:10.1016/j.cplett.2010.07.096.

[Mukherjee2013] Anupam Mukherjee, A. David Ariza-Flores, R. Fabiola Balderas-Valadez, and Vivechana Agarwal. Controlling the optical properties of composite multilayered photonic structures: effect of superposition. *Opt. Express*, 21(14):17324, 2013. ISSN 1094-4087. doi:10.1364/OE.21.017324.

[Mukhurov2010] N. I. Mukhurov, S. P. Zhvavyi, I. V. Gasenkova, S. N. Terekhov, P. P. Pershukevich, and V. A. Orlovich. Journal of Applied Spectroscopy, Vol. 77, No. 4, 2010. *Radiat. Med.*, 77(4):449–467, 2010.

[Nagaura2008] T. Nagaura, F. Takeuchi, and S. Inoue. Fabrication and structural control of anodic alumina films with inverted cone porous structure using multi-step anodizing. *Electrochim. Acta*,

53(5):2109–2114, 2008. ISSN 00134686. doi:10.1016/j.electacta.2007.09.016.

[Nakayama2008] Keisuke Nakayama, Katsuaki Tanabe, and Harry A. Atwater. Plasmonic nanoparticle enhanced light absorption in GaAs solar cells. *Appl. Phys. Lett.*, 93(12), 2008. ISSN 00036951. doi:10.1063/1.2988288.

[Nielsch2002] Kornelius Nielsch, Jinsub Choi, Kathrin Schwirn, Ralf B. Wehrspohn, and Ulrich Gösele. Self-ordering Regimes of Porous Alumina: The 10 Porosity Rule. *Nano Lett.*, 2(7):677–680, 2002. ISSN 1530-6984. doi:10.1021/nl025537k.

[N.Patel2012] P. N.Patel and Vivekanand Mishra. Simulations and Analysis of Nano Scale Porous Silicon Structures for Optical Sensor Applications. *Int. J. Comput. Appl.*, 56(10):14–18, 2012. doi: 10.5120/8925-2997.

[Nusz2009] Greg J. Nusz, Adam C. Curry, Stella M. Marinakos, Adam Wax, and Ashutosh Chilkoti. Geometry for Label-FreeRational Selection of Gold Nanorod Plasmonic Biosensors. *ACS Nano*, 3(4):795–806, 2009.

[Ono2005] Sachiko Ono, Makiko Saito, and Hidetaka Asoh. Self-ordering of anodic porous alumina formed in organic acid electrolytes. *Electrochim. Acta*, 51(5):827–833, 2005. ISSN 00134686. doi: 10.1016/j.electacta.2005.05.058.

[Ono2004] Sachiko Ono, Makiko Saito, Miyuki Ishiguro, and Hidetaka Asoh. Controlling Factor of Self-Ordering of Anodic Porous Alumina. *J. Electrochem. Soc.*, 151(8):B473, 2004. ISSN 00134651. doi:10.1149/1.1767838.

[Palik2012] E.D. Palik. *Handbook of Optical Constants of Solids-I*. 2012.

[Petryayeva2011] Eleonora Petryayeva and Ulrich J. Krull. Localized surface plasmon resonance: Nanostructures, bioassays and biosensing-A review. *Anal. Chim. Acta*, 706(1):8–24, 2011. ISSN 00032670. doi:10.1016/j.aca.2011.08.020.

[Pillai2010] S. Pillai and M. A. Green. Plasmonics for photovoltaic applications. *Sol. Energy Mater. Sol. Cells*, 94(9):1481–1486, 2010. ISSN 09270248. doi:10.1016/j.solmat.2010.02.046.

[Porta-i-Batalla2016] Maria Porta-i Batalla, Chris Eckstein, Elisabet Xifré-Pérez, Pilar Formentín, J. Ferré-Borrull, and Lluis F. Marsal. Sustained, Controlled and Stimuli-Responsive Drug Release Systems Based on Nanoporous Anodic Alumina with Layer-by-Layer Polyelectrolyte. *Nanoscale Res. Lett.*, 11(1), 2016. ISSN 1556276X. doi:10.1186/s11671-016-1585-4.

[Rahman2011] Mohammad Mahbubur Rahman, Josep Ferré-Borrull, Josep Pallarès, and Lluis F. Marsal. Photonic stop bands of two-dimensional quasi-random structures based on macroporous silicon. *Phys. Status Solidi Curr. Top. Solid State Phys.*, 8(3):1066–1070, 2011. ISSN 18626351. doi:10.1002/pssc.201000415.

[Rahman2013] Mohammad Mahbubur Rahman, Lluis F. Marsal, Josep Pallarès, and Josep Ferré-Borrull. Tuning the photonic stop bands of nanoporous anodic alumina-based distributed bragg reflectors by pore widening. *ACS Appl. Mater. Interfaces*, 5(24):13375–13381, 2013. ISSN 19448244. doi:10.1021/am4043118.

[Sai2006] Hitoshi Sai, Homare Fujii, Koji Arafune, Yoshio Ohshita, Masafumi Yamaguchi, Yoshiaki Kanamori, and Hiroo Yugami. Antireflective subwavelength structures on crystalline Si fabricated using directly formed anodic porous alumina masks. *Appl. Phys. Lett.*, 88(20):1–4, 2006. ISSN 00036951. doi:10.1063/1.2205173.

[Sannomiya2011] Takumi Sannomiya, Olivier Scholder, Konstantins Jefimovs, Christian Hafner, and Andreas B. Dahlin. Investigation of plasmon resonances in metal films with nanohole arrays for biosensing applications. *Small*, 7(12):1653–1663, 2011. ISSN 16136810. doi:10.1002/smll.201002228.

[Santos2012c] A. Santos, P. Formentín, J. Ferré-Borrull, J. Pallarès, and L. F. Marsal. Nanoporous anodic alumina obtained without protective oxide layer by hard anodization. *Mater. Lett.*, 67(1):296–299, 2012. ISSN 0167577X. doi:10.1016/j.matlet.2011.09.101.

[Santos2012] Abel Santos, Maria Alba, Mohammad M. Rahman, Pilar Formentin, Josep Ferre-Borrull, Josep Pallares, and Lluis F. Marsal. Structural tuning of photoluminescence in nanoporous anodic alumina by hard anodization in oxalic and malonic acids. *Nanoscale Res. Lett.*, 7(1):228, 2012. ISSN 1556-276X. doi:10.1186/1556-276X-7-228.

[Santos2012a] Abel Santos, Victor S. Balderrama, María Alba, Pilar Formentín, Josep Ferré-Borrull, Josep Pallarès, and Lluís F. Marsal. Nanoporous anodic alumina barcodes: Toward smart optical biosensors. *Adv. Mater.*, 24(8):1050–1054, 2012. ISSN 09359648. doi:10.1002/adma.201104490.

[Santos2010] Abel Santos, Pilar Formentín, Josep Pallarés, Josep Ferré-Borrull, and Lluís F. Marsal. Fabrication and characterization of high-density arrays of P3HT nanopillars on ITO/glass substrates. *Sol. Energy Mater. Sol. Cells*, 94(7):1247–1253, 2010. ISSN 09270248. doi:10.1016/j.solmat.2010.03.016.

[Santos2013a] Abel Santos, Tushar Kumeria, and Dusan Losic. Nanoporous anodic aluminum oxide for chemical sensing and biosensors. *TrAC - Trends Anal. Chem.*, 44:25–38, 2013. ISSN 01659936. doi:10.1016/j.trac.2012.11.007.

[Santos2013] Abel Santos, Tushar Kumeria, and Dusan Losic. Optically optimized photoluminescent and interferometric biosensors based on nanoporous anodic alumina: A comparison. *Anal. Chem.*, 85(16):7904–7911, 2013. ISSN 00032700. doi:10.1021/ac401609c.

[Santos2014] Abel Santos, Tushar Kumeria, and Dusan Losic. Nanoporous Anodic Alumina: A Versatile Platform for Optical Biosensors. *Materials (Basel).*, pages 4297–4320, 2014. doi:10.3390/ma7064297.

[Santos2014a] Abel Santos, Tushar Kumeria, Ye Wang, and Dusan Losic. Insitu monitored engineering of inverted nanoporous anodic alumina funnels: on the precise generation of 3D optical nanostructures. *Nanoscale*, 6(1):9991–9999, 2014. ISSN 2040-3372. doi:10.1039/c4nr01422g.

[Santos2012b] Abel Santos, Gerard Macías, Josep Ferré-Borrull, Josep Pallarés, and Lluís F. Marsal. Photoluminescent enzymatic sensor based on nanoporous anodic alumina. *ACS Appl. Mater. Interfaces*, 4(7):3584–3588, 2012. ISSN 19448244. doi:10.1021/am300648j.

[Santos2016] Abel Santos, Jeong Ha Yoo, Charu Vashisth Rohatgi, Tushar Kumeria, Ye Wang, and Dusan Losic. Realisation and advanced engineering of true optical rugate filters based on nanoporous anodic alumina by sinusoidal pulse anodisation. *Nanoscale*, 8(3):1360–1373, 2016. ISSN 20403372. doi:10.1039/c5nr05462a.

[Shimizu2000] K. Shimizu, H. Habazaki, P. Skeldon, G. E. Thompson, and G. C. Wood. Migration of sulphate ions in anodic alumina. *Electrochim. Acta*, 45(11):1805–1809, 2000. ISSN 00134686. doi:10.1016/S0013-4686(99)00397-7.

[Shimizu2001] K. Shimizu, H. Habazaki, P. Skeldon, G. E. Thompson, and G. C. Wood. Migration of oxalate ions in anodic alumina. *Electrochim. Acta*, 46(28):4379–4382, 2001. ISSN 00134686. doi:10.1016/S0013-4686(01)00660-0.

[Srivastava2015] Sachin K. Srivastava, Hilla Ben Hamo, Ariel Kushmaro, Robert S. Marks, Christoph Grüner, Bernd Rauschenbach, and Ibrahim Abdulhalim. Highly sensitive and specific detection of E. coli by a SERS nanobiosensor chip utilizing metallic nanosculptured thin films. *Analyst*, 140(9):3201–3209, 2015. ISSN 0003-2654. doi:10.1039/C5AN00209E.

[Stewart2008] Matthew E. Stewart, Christopher R. Anderton, Lucas B. Thompson, Joana Maria, Stephen K. Gray, John A. Rogers, and Ralph G. Nuzzo. Nanostructured plasmonic sensors. *Chem. Rev.*, 108(2):494–521, 2008. ISSN 00092665. doi: 10.1021/cr068126n.

[Suarez2012] I. Suárez, V. Chirvony, D. Hill, and J. Martínez-Pastor. Simulation of surface-modified porous silicon photonic crystals for biosensing applications. *Photonics Nanostructures - Fundam. Appl.*, 10(3):304–311, 2012. ISSN 15694410. doi: 10.1016/j.photonics.2011.04.014.

[Sulka2009] Grzegorz D. Sulka and Wojciech J. Stepniowski. Structural features of self-organized nanopore arrays formed by anodization of aluminum in oxalic acid at relatively high temperatures. *Electrochim. Acta*, 54(14):3683–3691, 2009. ISSN 00134686. doi:10.1016/j.electacta.2009.01.046.

[Taflove1980] Allen Taflove. Application of the Finite-Difference Time-Domain Method to Sinusoidal Steady-State Electromagnetic-Penetration Problems. *IEEE Trans. Electromagn. Compat.*, EMC-22(3):191–202, 1980. ISSN 0018-9375. doi:10.1109/TEMC.1980.303879.

[Taflove1975] Allen Taflove and M E Brodwin. Numerical Solution of Steady-State Electromagnetic Scattering Problems Using the Time-Dependent Maxwell's Equations. *IEEE Trans. Microw. Theory Tech.*, 23(8):623–630, 1975. ISSN 0018-9480. doi:10.1109/TMTT.1975.1128640.

[Thompson1997] G E Thompson. Porous anodic alumina: fabrication, characterization and applications. *Thin Solid Films*, 297(1-2):192–201, 1997. ISSN 0040-6090. doi:http://dx.doi.org/10.1016/S0040-6090(96)09440-0.

[Toccafondi2015] C. Toccafondi, R. La Rocca, A. Scarpellini, M. Salerno, G. Das, and S. Dante. Thin nanoporous alumina-based SERS platform for single cell sensing. *Appl. Surf. Sci.*, 351:738–745, 2015. ISSN 01694332. doi:10.1016/j.apsusc.2015.05.169.

[Vo-Dinh2015] Tuan Vo-Dinh, Yang Liu, Andrew M. Fales, Hoan Ngo, Hsin Neng Wang, Janna K. Register, Hsiangkuo Yuan, Stephen J. Norton, and Guy D. Griffin. SERS Nanosensors and Nanoreporters: Golden Opportunities in Biomedical Applications. *Wiley Interdiscip. Rev. Nanomedicine Nanobiotechnology*, 7(1):17–33, 2015. ISSN 19390041. doi:10.1002/wnan.1283.

[VonFreymann2003] G. Von Freymann, W. Koch, D. C. Meisel, M. Wegener, M. Diem, A. Garcia-Martin, S. Pereira, K. Busch, J. Schilling,

R. B. Wehrspohn, and U. Gösele. Diffraction properties of two-dimensional photonic crystals. *Appl. Phys. Lett.*, 83(4):614–616, 2003. ISSN 00036951. doi:10.1063/1.1596731.

[Vrublevsky2005] I. Vrublevsky, V. Parkoun, and J. Schreckenbach. Analysis of porous oxide film growth on aluminum in phosphoric acid using re-anodizing technique. *Appl. Surf. Sci.*, 242(3-4):333–338, 2005. ISSN 01694332. doi:10.1016/j.apsusc.2004.08.034.

[Whittaker1999] D. Whittaker and I. Culshaw. Scattering-matrix treatment of patterned multilayer photonic structures. *Phys. Rev. B*, 60(4):2610–2618, 1999. ISSN 0163-1829. doi:10.1103/PhysRevB.60.2610.

[Willets2007] Katherine A. Willets and Richard P. Van Duyne. Localized Surface Plasmon Resonance Spectroscopy and Sensing. *Annu. Rev. Phys. Chem.*, 58(1):267–297, 2007. ISSN 0066-426X. doi:10.1146/annurev.physchem.58.032806.104607.

[Xu2004] W. L. Xu, M. J. Zheng, S. Wu, and W. Z. Shen. Effects of high-temperature annealing on structural and optical properties of highly ordered porous alumina membranes. *Appl. Phys. Lett.*, 85(19):4364–4366, 2004. ISSN 00036951. doi:10.1063/1.1815072.

[Yanik2010] Ahmet A. Yanik, Min Huang, Osami Kamohara, Alp Artar, Thomas W. Geisbert, John H. Connor, and Hatice Altug. An optofluidic nanoplasmonic biosensor for direct detection of live viruses from biological media. *Nano Lett.*, 10(12):4962–4969, 2010. ISSN 15306984. doi:10.1021/nl103025u.

[Yee1966] K. Yee. Numerical solution of initial boundary value problems involving Maxwell's equations in isotropic media. *IEEE Trans. Antennas Propag.*, 14(3):302–307, 1966. ISSN 0018-926X. doi:10.1109/TAP.1966.1138693.

[Yokogawa2012] Sozo Yokogawa, Stanley P. Burgos, and Harry A. Atwater. Plasmonic color filters for CMOS image sensor applications. *Nano Lett.*, 12(8):4349–4354, 2012. ISSN 15306984. doi:10.1021/nl302110z.

[Zaraska2016a] Leszek Zaraska, Anna Brudzisz, Ewa Wierzbicka, and Grzegorz D. Sulka. The effect of electrolyte change on the morphology and degree of nanopore order of porous alumina formed by two-step anodization. *Electrochim. Acta*, 198:259–267, 2016. ISSN 00134686. doi:10.1016/j.electacta.2016.03.050.

[Zayats2005] Anatoly V. Zayats, Igor I. Smolyaninov, and Alexei A. Maradudin. Nano-optics of surface plasmon polaritons. *Phys. Rep.*, 408(3-4):131–314, 2005. ISSN 03701573. doi:10.1016/j.physrep.2004.11.001.

[Zhang2008a] Jin Z. Zhang and Cecilia Noguez. Plasmonic optical properties and applications of metal nanostructures. *Plasmonics*, 3(4):127–150, 2008. ISSN 15571955. doi:10.1007/s11468-008-9066-y.

UNIVERSITAT
ROVIRA i VIRGILI